2024-12-20

Mass- and Momentum-Conserved Secondary Injection Model (MMC-SIM) for Thrust Vector Control Analysis

Abdelwahab, Noreen

UNIVERSITY OF CALGARY

Mass- and Momentum-Conserved Secondary Injection Model (MMC-SIM) for Thrust Vector Control Analysis

by

Noreen Abdelwahab

A THESIS
SUBMITTED TO THE FACULTY OF GRADUATE STUDIES
IN PARTIAL FULFILMENT OF THE REQUIREMENTS FOR THE
DEGREE OF MASTER OF SCIENCE

GRADUATE PROGRAM IN MECHANICAL ENGINEERING

CALGARY, ALBERTA
DECEMBER, 2024

Abstract

A mass- and momentum-conserved secondary injection model (MMC-SIM) is presented for thrust vector control (TVC) analysis in axisymmetric nozzles. TVC modelling provides fast thrust vector predictions for control and design applications. MMC-SIM addresses a key limitation in prior models - the lack of mass conservation, which often compromised accuracy through assumed jet exit conditions. Using a semi-empirical approach based on the blunt-body analogy, MMC-SIM uniquely incorporates both mass and momentum conservation for thrust vector predictions. Computational fluid dynamics (CFD) simulations were performed to verify that MMC-SIM captures the underlying physics of the flow, including boundary layer separation and the pressure distribution. MMC-SIM shows strong agreement with experimental results, yielding average and maximum lateral force prediction errors of 3.3% and 4.8%, respectively. Compared to current models, MMC-SIM halves the maximum error on the pressure-driven lateral force. MMC-SIM is highly suitable for integration into six degree-of-freedom rocket flight simulation programs.

Preface

This thesis is an original work by the author. No part of this thesis has been previously published.

Acknowledgements

I would like to express my sincere gratitude to my supervisor, Dr. Craig Johansen, for your guidance and mentorship, which have been instrumental in shaping my research and academic growth. Thank you to my family, friends, colleagues and advisors for your unconditional support, advice and friendship. I am also grateful for the generous financial support of NSERC, the Faculty of Graduate Studies, Dr. Mildred L.G. Shaw, and the estate of Mary H. Petrie, which made this work possible. It is difficult to fully express my immense gratitude to all who have supported and guided me in my education.

To osreti.

Table of Contents

List of Figures

List of Tables

List of Symbols, Abbreviations, and Nomenclature

Symbol	Definition
A	Cross-sectional area
A_s	Sutherland law viscosity constant
$a_{f\pm}$	Volumetric flux through cell face including wave propagation effects
a_1	k-ω SST coefficient defined in Tab. 4.1
C_d	Discharge coefficient of secondary injection port
C_f	Coefficient of friction
$\boldsymbol{C}_f$	Coordinates of the centre of a cell face
C_P	Heat capacity at constant pressure
C_V	Heat capacity at constant volume
C_Δ	Coefficient for surface normal gradient of orthogonal meshes
C_Δ^{corr}	Non-orthogonal correction for C_Δ
$CD_{k\omega}$	Cross-diffusion term for blending the k-ω and k-ϵ turbulence models
Co	Courant number
c	Speed of sound/wave propagation
D_inj	Diameter of secondary injection port
d	Distance to the nearest wall
$\boldsymbol{d}$	Displacement vector from owner to neighbour cell centres
$\boldsymbol{d}_{fN}$	Displacement vector from $\boldsymbol{C}_f$ to neighbouring cell centre
E	Total energy
e	Specific internal energy
$e^\mathrm{ab}_\mathrm{approx}$	Approximate relative error of mesh b with respect to mesh a

$\boldsymbol{e}_1, \boldsymbol{e}_2, \boldsymbol{e}_3$	Standard basis of three-dimensional coordinate vector space
$\mathcal{F}()$	Function of
F_1	k-ω SST blending function for coefficients
F_2	k-ω SST blending function for turbulent viscosity
F_j	Force due to secondary jet momentum
F_y	Total lateral thrust
$\boldsymbol{F}_{net}$	Net externally applied forces on control volume
$\boldsymbol{G}$	Tensor of weighted squared displacements for gradient discretization
$\boldsymbol{G}_C$	Function to be minimized for least squares gradient discretization
h	Characteristic height of secondary injection
h_M	Representative cell size of a mesh
$\boldsymbol{I}$	Identity matrix
K	Amplification factor
k	Turbulent kinetic energy
M	Mach number
$\dot{m}$	Mass flow rate
N	Number of cells in a mesh
$\boldsymbol{n}$	Surface normal unit vector
P	Pressure
$\widetilde{P_k}$	Limited turbulent kinetic energy production rate
p	Order of grid convergence (observed)
p_FS	Limited observed order of grid convergence
P_k	Turbulent kinetic energy production rate
p_r	Ratio of the observed order to the theoretical order of grid convergence
p_th	Theoretical order of grid convergence
$\boldsymbol{q}$	Diffusive heat flux
R	Specific gas constant
R_C	Shock hyperbola vertex radius of curvature
R_s	Separation hyperbola vertex radius of curvature
$\boldsymbol{R}_x, \boldsymbol{R}_y, \boldsymbol{R}_z$	Rotation matrices
r	Radius of spherical/cylindrical obstruction
r_ab	Ratio of refinement between two consecutive grids a and b

r_{grad}	Gradient ratio
S	Strain invariant
$\boldsymbol{S}$	Mean strain rate tensor
s	Sign of the ratio between the relative errors ϵ_{32} and ϵ_{21}, defined as $s = \text{sgn}\left(\frac{\epsilon_{32}}{\epsilon_{21}}\right)$
$\boldsymbol{S}_f$	Face area normal vector
t	Time
T	Temperature
T_s	Sutherland law reference temperature
$\boldsymbol{u}$	Velocity vector
u_{disc}	Discretization uncertainty
u_τ	Friction velocity
V	Volume
w_f	Weighting function for linear interpolation of cell centre to face values
w_{id}	Weighting factor for least squares gradient discretization
x	Longitudinal axis, aligned with the rocket axis
x_0	x-coordinate of hyperbola centre
y_0	y-coordinate of hyperbola centre
$y+$	Non-dimensional wall distance

Greek Symbol	**Definition**
α	Weighting factor for discretization of convective fluxes
α_n	Conical nozzle half-angle
α_t	Kinematic turbulent thermal conductivity
β	k-ω SST coefficient defined in Tab. 4.1
β_{lim}	Flux limiter
β^*	k-ω SST coefficient defined in Tab. 4.1
Γ	Diffusivity
γ_t	k-ω SST coefficient defined in Tab. 4.1
γ	Ratio of specific heats
Δ	Bow shock standoff distance
δ	Estimated discretization error
δ	Flow deflection angle for oblique shock waves
ϵ	Turbulent energy dissipation rate

ϵ_{ab}	Solution error of mesh a with respect to mesh b
ζ	Oblique shock wave angle
Θ	Obstruction local inclination angle
θ	Mach angle/hyperbola asymptote angle
κ	Thermal conductivity
κ_f	Switching function
μ	Dynamic viscosity
μ_t	Turbulence dynamic viscosity
ν	Kinematic viscosity
ν_t	Turbulence kinematic viscosity
ξ_f	Weighting function for discretization of convective fluxes
ρ	Density
σ_k	k-ω SST coefficient defined in Tab. 4.1
σ_ω	k-ω SST coefficient defined in Tab. 4.1
$\boldsymbol{\tau}$	Viscous stress tensor
τ_w	Wall shear stress
Φ	Mass flux
ϕ_f	Volumetric flow rate through cell face
Ψ	Rotation angle
$\boldsymbol{\psi}$	Arbitrary flow variable
ω	Turbulent dissipation frequency

Abbreviations	**Definition**
APG	Adverse pressure gradient
ASME	American Society of Mechanical Engineers
BL	Boundary layer
CFD	Computational fluid dynamics
CFL	Courant-Friedrichs-Lewy
CS	Control surface
CV	Control volume
DILU	Diagonal incomplete lower-upper
EDDES	Enhanced delayed detached eddy simulation
FFS	Forward-facing step

FS	Factor of safety
GAMG	Generalized-algebraic multigrid
GCI	Grid convergence index
ICARE	Institute for Combustion, Aerothermics, Reactivity and Environment
KNP	Kurganov, Noelle, and Petrova
KT	Kurganov and Tadmore
LES	Large eddy simulation
LITVC	Liquid injection thrust vector control
LOX	Liquid oxygen
LSQ	Least squares
MMC-SIM	Mass- and momentum-conserved secondary injection model
N/A	Not available
NPR	Nozzle pressure ratio
PBiCGStab	Preconditioned bi-conjugate gradient stabilized
PDE	Partial differential equation
PG	Pressure gradient
PSLV	Polar Satellite Launch Vehicle
PUV	Primary upstream vortex
RANS	Reynolds-averaged Navier-Stokes
rCF	rhoCentralFOAM
RFNA	Red fuming nitric acid
Re	Reynolds
SA	Spalart-Allmaras
SITVC	Secondary injection thrust vector control
SPR	Secondary pressure ratio
SST	Shear stress transport
SUV	Secondary upstream vortex
SWBLI	Shock wave boundary layer interaction
TVC	Thrust vector control
TKE	Turbulent kinetic energy
UDMH	Unsymmetrical dimethylhydrazine
uEuler	Unsteady Euler

uRANS	Unsteady Reynolds-averaged Navier-Stokes
WF	Wall function

Subscripts and Superscripts	**Definition**
$\square_{amb}$	Ambient conditions
$\square_{C}$	Owner cell
$\square_{e}$	Nozzle exit
$\square_{f}$	Cell face
$\square_{f+}$	From positive flow direction as per Fig. 4.1
$\square_{f-}$	From negative flow direction as per Fig. 4.1
$\square_{N}$	Neighbour cell
$\square_{plat}$	Plateau region
$\square_{t}$	Stagnation state
$\square_{w}$	At the wall
$\square_{\infty}$	Freestream value
$\square^{*}$	Sonic state

Epigraph

The simplest things are overlooked. And yet, it is the simplest things that are the most essential.

- T. L. Qualls, *Painted Oxen*

Chapter 1

Introduction

The growing demand to launch payloads into orbit has supercharged the development of high-performance rockets (Messinger et al., 2019; Schmierer et al., 2019). Modern rockets require enhanced manoeuvrability to perform trajectory corrections, docking, deorbiting, reentry, and landing (Sutton and Biblarz, 2017). Requiring high control authority, thrust vector control (TVC) is used to maintain vehicle flight stability and desired trajectory (Pelouch, 1970). One method for manipulating thrust direction involves injecting fluid laterally into the nozzle in a method known as secondary injection thrust vector control (SITVC) (Green and McCullough, 1961; Newton, 1961). SITVC has advantages over conventional TVC mechanisms. It eliminates moving mechanical components associated with movable nozzles, and generates higher lateral thrust when compared to cold gas thrusters in vacuum (Hozaki et al., 1963). Additionally, SITVC is particularly relevant for hybrid rocket technologies, as the liquid oxidizer may be used for injection, eliminating challenging flex-seal nozzles (Carroll et al., 2009). Furthermore, it is effective across a wide range of flight regimes, including both atmospheric and vacuum conditions (Sutton and Biblarz, 2017).

Estimates of the lateral thrust generated by SITVC are required for system design and analysis. At the advent of SITVC technology, low-order models were developed that rely on empirical relations, simplifying assumptions and correction factors derived from experiments (Broadwell, 1963; Karamcheti and Tao-Sze Hsia, 1963; Spaid, 1964; Walker et al., 1962; Wilson and Comparin, 1969; Wu et al., 1961; Zukoski and Spaid, 1964). These models prioritized the prediction of the final outcome, in this case the lateral force, over capturing the underlying physics of the flow. Calibration using empirical results and experimental data yielded acceptable results despite incorrect intermediate predictions, leading to a lack of understanding of the wall pressure profile and boundary layer effects (Broadwell, 1963).

Advancements in computational fluid dynamics (CFD) and processing power provide the tools for

simulating SITVC, offering deeper insights into the complex flow physics involved (Hawkes, 1996; Ko and Yoon, 2002). These capabilities have enabled numerical simulation using various turbulence modelling approaches, including Reynolds-averaged Navier-Stokes (RANS) (Chen and Liao, 2020; Deere et al., 2003; Forghany et al., 2018a; Kobald et al., 2017; Zmijanovic et al., 2016), Enhanced Delayed Detached Eddy Simulation (EDDES) (Younes et al., 2020), and Large eddy simulations (LES) (Yan et al., 2023).

Mangin (2006) developed a model that predicts pressure distribution and boundary layer separation using empirical relations, and compared the results to CFD data. Maarouf (2008), Sellam et al. (2012), and Zmijanovic et al. (2016) expanded on this work by comparing the results to additional experimental and numerical data. Recently, other researchers have attempted to replicate the model, but had to introduce additional assumptions and simplifications (Chen and Liao, 2020; Deng et al., 2014; Younes and Hickey, 2020). These modifications highlight challenges in accurately reproducing the original findings and the need for further investigation of the existing modelling techniques for SITVC.

This study aims to address these challenges by focusing on the underlying mechanisms that generate the lateral force with an emphasis on the reproducibility of results. The objectives of this thesis are:

1. To identify assumptions and limitations in existing models and if applicable, demonstrate the need for a new model through a comprehensive literature review.

2. To develop a new model, grounded in both empirical and theoretical analysis, for the prediction of forces generated by fluidic injection at varying secondary pressure levels.

3. To assess the proposed model through comparison of force and wall pressure predictions with numerical simulations and experimental data available in the literature.

4. To identify the limitations of the proposed model and evaluate the applicability of its assumptions.

The remainder of Chapter 1 provides a background on TVC and the historical development of SITVC. Chapter 2 reviews existing models with a focus on assessing their accuracy, assumptions and applicability. In Chapter 3, a new model is proposed, and Chapter 4 details the numerical methodologies used in the simulations. The results of the proposed model and numerical simulations are evaluated in Chapter 5, along with an assessment of the model's performance. Finally, conclusions and recommendations are presented in Chapter 6.

1.1 Attitude Control

To begin, a brief overview of attitude control for rockets is provided. Attitude control is the manipulation of a vehicle's orientation with respect to a reference frame. Attitude control systems maintain vehicle flight stability and desired trajectory while filtering flight disturbances. Disturbances during flight may include atmospheric wind, vehicle and thrust misalignments, and changes in the vehicle's centre of gravity (Woodberry and Zeamer, 1974). Attitude control of a vehicle requires orientation sensors, actuators, and a control algorithm (Starin and Eterno, 2011). The flight regime and mission requirements dictate selection of the appropriate control mechanism, such as external aerodynamic control surfaces, gas thrusters and TVC. Figure 1.1 illustrates a typical orbital rocket trajectory, highlighting key flight events and their corresponding control mechanisms.

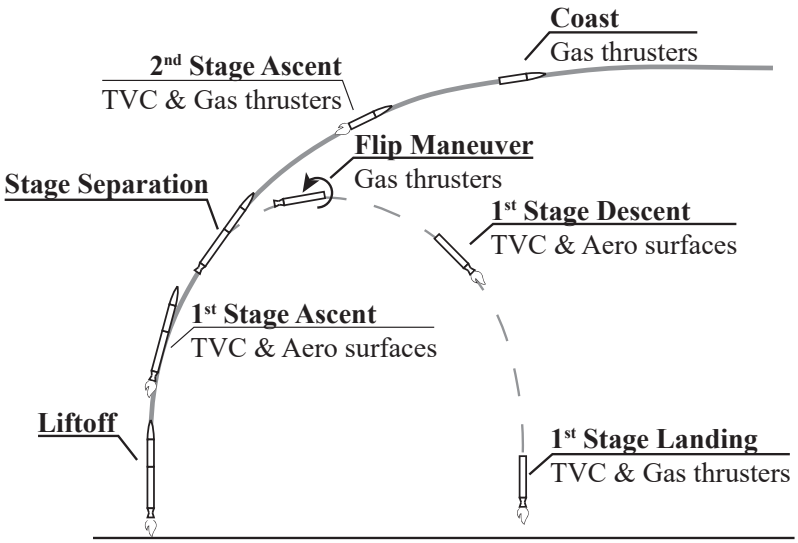

Figure 1.1: Schematic of a typical orbital rocket trajectory with control mechanisms at key flight events. Adapted from SpaceX (2024).

External aerodynamic surfaces (such as fins and canards) are only effective for attitude control of rockets moving at relatively high speeds through the atmosphere (Sutton and Biblarz, 2017). The limited effectiveness of these control surfaces generates the need for more active attitude control mechanisms during takeoff and landing, and throughout much of the flight (Wu et al., 1961).

Hot and cold gas thrusters are primarily used in space for attitude control, minor in-flight trajectory corrections, and after engine cut-off (Sutton and Biblarz, 2017). The impulse required for attitude control is generated by the ejection of exhaust gases from hot gas thrusters or from the expansion of compressed gases for cold gas thrusters. Nitrogen cold gas thrusters on the Pegasus rocket provided roll control and attitude control during coast (Sutton and Biblarz, 2017). Additionally, cold nitrogen gas thrusters are used

to guide the first stage landing and second stage ascent/coast of SpaceX's Falcon 9 (SpaceX, 2021).

When high control authority is required, TVC is commonly used (Sutton and Biblarz, 2017). Thrust vectoring is the manipulation of the direction of the rocket exhaust to control vehicle attitude. Deflecting the thrust generates a lateral force that causes a moment about the vehicle's centre of gravity as shown in Fig. 1.2. Thrust vectoring provides control over the pitch and yaw moments of single-nozzle vehicles.

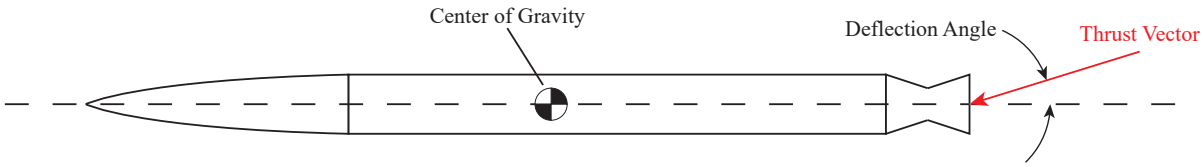

Figure 1.2: Schematic of thrust vector control.

Unlike aerodynamic control surfaces, TVC is effective in both atmospheric and vacuum flight. However, TVC systems are only effective during powered flight because they rely on the deflection of the engine exhaust. TVC mechanisms include jet vanes and tabs, movable nozzle systems, and secondary fluid injection in the nozzle.

Jet vanes and tabs, which redirect motor thrust by moving small aerodynamic surfaces near the exhaust, are used in small rockets and early missile technologies (Wu et al., 1961). While simple to implement, they are prone to failure by ablation (Nickens et al., 1970).

Movable nozzles adjust the direction of thrust by pivoting either the whole engine (as in liquid rockets) or just the nozzle (as in solid rockets). Commonly used for large rockets, movable nozzles are capable of precise corrections even with substantial thrust outputs. However, these systems are mechanically complex, with moving parts and actuators that add weight. Over-designed components further increase system mass (Wu et al., 1961). Depending on mission requirements, the weight penalties may exceed the performance advantages provided by movable nozzles (Kirby and Van Vooren, 1964).

In SITVC systems, side thrust arises from the lateral injection of a fluid in the nozzle (Green and McCullough, 1961; Newton, 1961). In addition to the force generated by the secondary jet momentum, F_j, the interaction of the secondary fluid with the supersonic cross-flow generates unbalanced forces on the nozzle wall. As a result, the overall side-force, F_y, is higher than that generated by gas thrusters ejecting to vacuum at the same mass flow rate (Hozaki et al., 1963; Wu et al., 1961). The magnification factor, K, which is a measure of the effectiveness of secondary injection and is defined in Eq. 1.1, has typical values of about

two (Wu et al., 1961).

$$K = \frac{F_y}{F_j} \tag{1.1}$$

In practice, SITVC deflects exhaust gases by ±6° and high losses are incurred if larger deflections of up to ±12° are required (Woodberry and Zeamer, 1974).

1.2 Status of Technology

Secondary injection for TVC has been successfully implemented for solid and liquid rockets. Table 1.1 provides a list of selected systems that employed liquid injection TVC (LITVC). Figure 1.3 displays images of selected rocket and missiles that have used LITVC technology.

Table 1.1: Selected engines employing liquid injection for TVC.

System	**Description**	**Injectant**
Polaris A3 second stage (Woodberry and Zeamer, 1974)	Fleet Ballistic Missile	Freon 114-B2
Minuteman (Andreosky, 1965)	Intercontinental Ballistic Missle	Freon 114-B2
Titan IIIC and IIID (Stofan, 1973)	Expendable Launch System	N_2O_4
Sprint first and second stages (Bell Laboratories, 1975)	Anti-Ballistic Missile	Freon 114-B2
Hibex (Atta et al., 1991)	Anti-Ballistic Missile	Freon 114-B2
Lance (Sutton, 2003)	Short/Medium-Range Ballistic Missile	UDMH (Unsymmetrical dimethylhydrazine)
Polar Satellite Launch Vehicle (PSLV) first stage (Nazeer, 2018)	Expendable Launch System	$Sr(ClO_4)_2$
M-V Rocket second stage (Morita and Kawaguchi, 2001)	Japanese Scientific Satellite Carrier	–

(a) Polaris A-3 missile (Missilery Info, 1971).

(b) Minuteman III missile (IAS, 2024).

(c) M-V (JAXA Institute of Space and astronautical science, 1997).

(d) Titan IIIC (US Department of Defense, 2024).

(e) Titan IIID (Cape Canaveral Space Force Museum, 1978).

(f) PSLV (Indian Space Research Organisation, 2019).

Figure 1.3: Selected rockets and missiles employing liquid injection TVC.

Of note, the LGM-30G Minuteman III is a land-based intercontinental ballistic missile that has been in service from 1970 until today. Representing one component of the nuclear triad, it will be in service until 2030 (Bell Laboratories, 1975). The 2nd and 3rd stages use secondary injection TVC. Additionally, the Japanese M-V solid-fuelled rocket was designed to launch scientific satellites. First launched in 1997, its second stage employed secondary injection for TVC (Morita and Kawaguchi, 2001). Furthermore, an exploded view of the Polaris A3 missile is schematically illustrated in Fig. 1.4. This two-stage ballistic missile used Freon 114-B2 as the liquid injectant for attitude control of the second stage, and flexible-joint nozzles for TVC of the first stage. Both stages were powered by solid-fuelled rocket motors.

Continuum Aerospace was tasked with conducting a feasibility study on Canadian microsatellite launch systems for the Canadian Space Agency (Carroll et al., 2009). They concluded that a three-stage hybrid rocket employing liquid injection TVC is the optimal technical solution. However, the development of a suitable

TVC system was identified as one of the key challenges due to a gap in the technological knowledge available from accessible sources. Additionally, hybrid rockets are being developed in Canada by Reaction Dynamics (Reaction Dynamics, 2023). With the increased attention surrounding hybrid rockets, understanding SITVC in the context of this propulsion system is crucial. While there are many examples of SITVC for solid and liquid rockets, only three research projects have specifically addressed its application to hybrid rockets, to the author's knowledge (Case, 2008; Karp et al., 2016, 2018; Lee et al., 2019; Simurda et al., 2012; Story et al., 2018, 2020; Tsohas et al., 2006, 2007; Whittinghill et al., 2019).

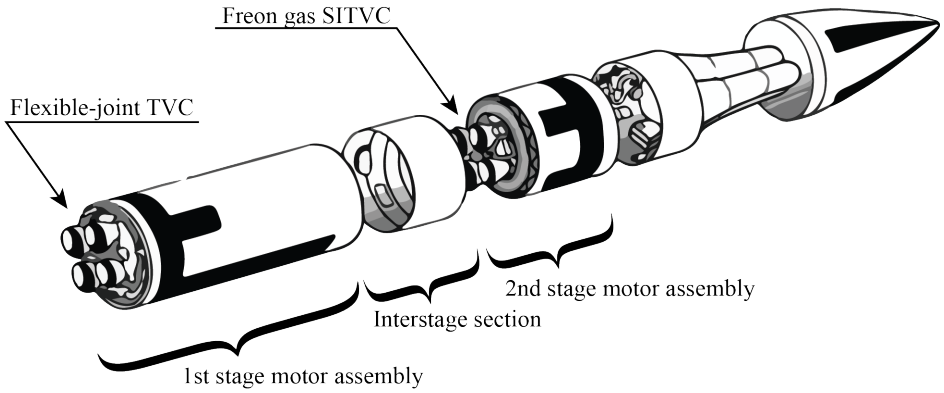

Figure 1.4: Schematic of Polaris A-3 missile. Adapted from Burnell (2006).

In 2012, a thrust vector controlled paraffin/Nytrox hybrid rocket was designed and ground-tested at Stanford University (Simurda et al., 2012). The Nytrox oxidizer (composed of oxygen and nitrous oxide) is liquid at the bottom of the tank and partially self-pressurizing gas at the top. The TVC system was designed to use the gas phase of the Nytrox oxidizer for cold-gas injection. Static testing of the rocket has been performed, but as of writing there is no record of the gas injection TVC system being tested.

In 2019, Lee et al. (2019) reported the results of hybrid rocket engine static fire tests with TVC achieved using hydrogen peroxide injection. The effects of chamber pressure, injectant flow rate, and injection location on the LITVC performance were parametrically investigated. Using a hydrogen-peroxide/paraffin motor, they found that doubling the main engine combustion chamber pressure from 20 to 40 bar improved side-specific impulse by 85.6 seconds under set conditions.

A hybrid rocket technology development program was undertaken for a Mars ascent vehicle utilizing LITVC (Karp et al., 2016, 2018; Story et al., 2018, 2020). As part of the program, a 6050 N thrust hybrid rocket motor was tested for single-stage-to-orbit hybrid propulsion system for Mars missions, but no quantitative data on the LITVC system performance was published. The study, conducted by Whittinghill et al. (2019), reported challenges with small combustion instabilities and nozzle erosion.

Chapter 2

Background on Modelling of SITVC

This chapter provides an overview of the existing models in the literature. A brief overview of the flow structures in an SITVC nozzle are introduced, then the most relevant models in the literature are discussed with a focus on their assumptions and limitations.

2.1 Modelling Motivation

Design and analysis of SITVC systems requires lateral thrust predictions. While numerical simulations generate detailed flow fields and experiments provide real-life validation, models are faster to implement and run, making them ideal for design optimization over a wide range of parameters, such as nozzle geometry, injection location and angle, and primary and secondary flow properties. These models are also useful for control system design and tuning. Many models have been proposed with varying levels of detail. These models all make simplifying assumptions about the flow field to make SITVC more amenable to analysis.

2.2 Flow Structures in an SITVC Nozzle

Figure 2.1 schematically illustrates the key flow phenomena that generate lateral thrust in an SITVC nozzle. The primary flow is first turned by a weak separation shock, then a strong bow shock. The secondary jet accelerates as it enters the primary nozzle and is deflected by the oncoming primary flow. In addition to the momentum injection of the secondary jet, the interaction between the primary and secondary flows generates an asymmetric pressure distribution along the nozzle wall that contributes to the lateral thrust. A complex flow field is generated inside the nozzle that includes jet expansion, shock-wave boundary

layer interaction and turbulent mixing. Key concepts used for developing the models are summarized in Appendix A, including control volume analysis, compressible flows, and boundary layer theory.

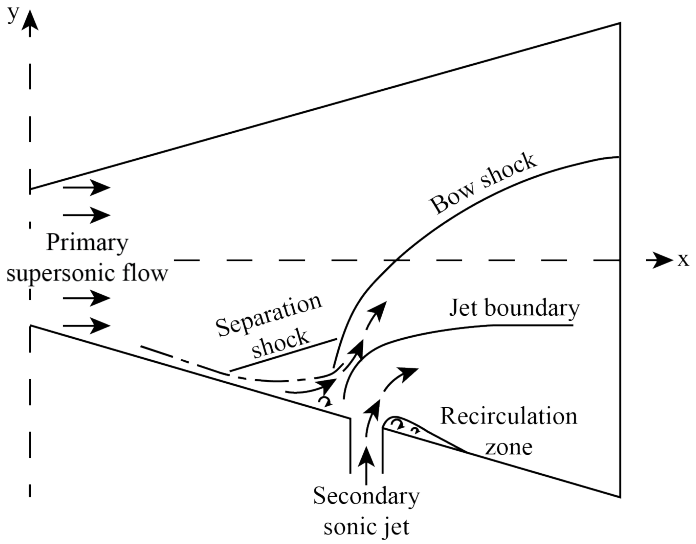

Figure 2.1: Schematic of key flow features generated by secondary injection thrust vector control. Adapted from Balu et al. (1991).

2.3 Overview of Models in the Literature

The complex three-dimensional flow that contributes to lateral force generation in an SITVC nozzle is difficult to analyze using purely theoretical models. Instead, most predictive models combine theory with empirical relations or scaling constants derived from static fire testing (Pelouch, 1970; Wilson and Comparin, 1969).

The lateral thrust is obtained by calculating the change in momentum of the injected jet, and the pressure changes along the nozzle wall. The side force, F_y, is composed of the jet reaction force, F_j, and the induced force due to the interaction between the two streams, F_i.

Figure 2.2 presents the most prominent models in the literature, categorized by modelling approach: blast wave theory, or blunt body analogy. The blast wave theory offers versatility, as it applies to both gas and liquid injectants, as well as reactive and inert injectants. Its simplicity makes it useful for quick, approximate calculations, though it relies on scaling parameters derived from experiments. Conversely, the blunt-body modelling approach is the most comprehensive, offering insight into the flow field upstream of the injection and providing relatively accurate results without the need for scaling parameters. However, it is the most challenging to implement. The following sections provide overviews of the models categorized

in Fig. 2.2.

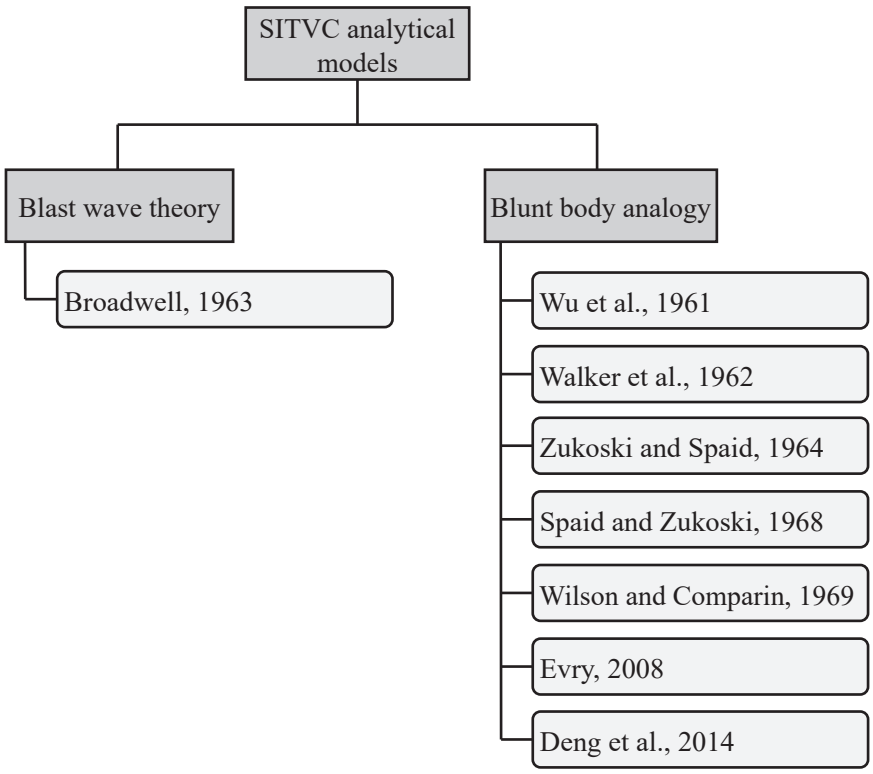

Figure 2.2: Classes of models for SITVC.

2.3.1 Blast-Wave Theory

The sudden release of energy at a point due to an explosion in a gas that is initially at rest is described by blast wave theory. This theory has been expanded to determine the pressure distribution and resulting forces due to the explosion of a line charge in a steady uniform flow. Lees and Kubota (1957) showed that the shape of the bow shock wave upstream of a blunt body in a uniform hypersonic flow shows similarity to the blast wave generated by the explosion of a line charge. The flow caused by the explosion of a line charge is analogous to hypersonic and high supersonic flow about a blunt body. Approximating the secondary injection stream as a blunt body in the primary flow, blast wave theory may be used to describe the pressure distribution and the forces on the wall near a secondary injection port.

Broadwell, 1963

Broadwell (1963) used blast wave theory to predict the side force generated due to secondary injection of a fluid. This first-order solution corresponding to Sakurai's cylindrical solution for the shock wave equation

(Sakurai, 1953) is applicable to both gas and liquid injection. Broadwell's model assumes that an injected liquid vaporizes instantaneously then mixes at a constant pressure. The model requires the effective density as a function of the mixture ratio to account for mixing, reaction processes, and the change in volume due to vaporization. However, the effective density was only defined for water, liquid oxygen (LOX) and Freon 114B-2 injected into solid propellant exhaust. No data is provided for hybrid or liquid propellant exhaust, or other injectants. Additionally, Broadwell assumes that the injected fluid accelerates to the freestream velocity. As a result, this model may not be applicable for injection ports located near the exit of the nozzle. Finally, Broadwell (1963) comments that the pressure distribution theorized by the blast wave theory near the injection port is incorrect. However, this inaccurate wall pressure distribution is used to compute the lateral forces in his model. Overall, the forces predicted by this model show similar trends to experimental data; computed lateral forces increase with secondary mass flow rate. However, the lateral forces are over-predicted, especially at high secondary mass flow rates.

2.3.2 Blunt-Body Models

Zukoski and Spaid (1964) investigated the shock pattern induced by a secondary gas injection using Schlieren imagery shown in Fig. 2.3. They observed a bow shock and flow separation in front of the injection

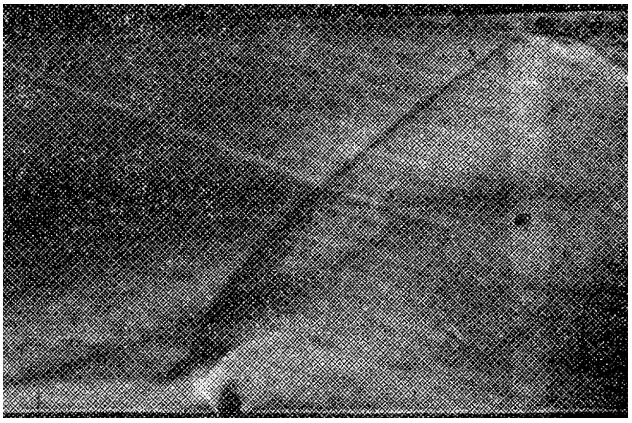

Figure 2.3: Schlieren image of supersonic cross-flow with a secondary jet injection. From Zukoski and Spaid (1964).

resembling the flow field that develops ahead of a solid body obstructing a supersonic flow. These findings led to the development of "blunt body" models, where the secondary jet is modelled as an equivalent obstruction in the primary flow. Prediction of the thrust generated in an SITVC nozzle using the blunt-body approach involves three main steps:

1. Define the shape and dimensions of an equivalent body, usually using the characteristic height, h.

2. Define the wall pressure distribution in the vicinity of the injection port.

3. Compute the lateral thrust by summing wall pressure and jet momentum contributions.

An advantage of blunt body models is that they provide not only the final result (the lateral force), but can also quantify flow phenomena such as the boundary layer separation and pressure distribution.

In the 1960s, Zukoski and Spaid, pioneers in the field, developed two independent models for flat plate secondary injection: one for a circular injection port (3D case), and the second for a transverse injection slot (2D case). The 2D slot injection relied on forward facing step (FFS) empirical relations. However, a key limitation of these models was the absence of a defined pressure distribution, which is required for calculating the lateral force.

Inspired by the work of Zukoski and Spaid, Wilson and Comparin (1969) developed a semi-empirical model that was the first to define the pressure distribution on the wall by dividing it into three distinct regions. However, implementation details and validation of the model were lacking.

Mangin (2006) and Maarouf (2008) extended the blunt-body approach to SITVC for axisymmetric nozzles. For brevity, this work refers to the model, developed at the University of Evry, as the Evry model. The semi-empirical approach fully defined both the pressure distribution and lateral force generation. Since then, other researchers have attempted to replicate the model, but had to introduce additional assumptions and simplifications (Deng et al., 2014; Chen and Liao, 2020; Younes and Hickey, 2020). The following sections provide overviews and discuss the limitations of existing blunt-body models. Note that the semi-empirical model in this work is based on these models.

Wu, Chapkis and Mager, 1961

Wu et al. (1961) predicted that the injection of a secondary jet into a supersonic primary flow leads to separation of the turbulent boundary layer from the nozzle wall. They defined and quantified an "accommodation" height to describe the secondary jet behaviour several years before the blunt-body analogy was officially named. Conservation of mass, momentum and energy for both the primary and secondary flows were used to compute the accommodation height, h.

The accommodation or injection height is a scaling parameter for the area along the nozzle wall that is disturbed by the secondary jet. The side force contribution due to the pressure distribution arising from the secondary jet may be found by integrating along the disturbed area. Note that each SITVC model defines the injection height in a different manner. As such, h should be regarded as a scaling parameter rather than a physical measure of the height of the injected jet when comparing across models.

Wu et al. (1961) not only characterized the injection height, they also applied the three conservation

laws in their derivation for the lateral force. To find the pressure field in the disturbed region, a method for determining the pressure ratio required to induce boundary layer separation in 2D flows was extended to 3D flows. With this assumption, the lateral force was computed by assuming an average pressure in the separated region. However, the model lacked sufficient detail to quantify the pressure distribution and the boundary layer separation, limiting insights into the underlying flow physics.

Walker, Stone and Shandor, 1962

Walker et al. (1962) developed a linearized model of fluid injection using supersonic flow over a forward-facing step as an analogous flow. In this model, mixing, phase changes and chemical reactions were assumed to be instantaneous and complete. The primary flow was considered to be an ideal gas. Equation 2.1 relates the induced component of the force to the freestream parameters assuming that the exhaust deflections are small (Walker et al., 1962). The turning angle of the primary flow must be sufficiently small to permit use of linearized flow theory.

$$F_i = \frac{P_\infty \gamma_\infty M_\infty^2 A_\infty}{\sqrt{M_\infty^2 - 1}} \tag{2.1}$$

The results of the analysis were reported to be qualitative rather than quantitative due to the restrictions imposed by the linearized supersonic flow theory.

Circular Slot - Zukoski and Spaid, 1964

Zukoski and Spaid (1964) theorized that the shock pattern induced by a secondary gas injection is similar to the pattern produced with a supersonic flow obstructed by a solid body. This blunt body is assumed to have a quarter-sphere nose and a half-cylinder body as shown in Fig. 2.6. The shape and size of the bow shock generated by secondary injection are similar to that generated by the blunt body. The injected fluid isentropically expands to the local ambient pressure (P_∞) and is redirected such that it travels parallel to the wall. A characteristic dimension describing the radius of the nose, h, was used as a scaling parameter for the side force generated. In contrast to Broadwell's model, they assume that no mixing occurs between the primary and secondary flows. Similarly to Walker et al. (1962), Zukoski and Spaid assume that the secondary jet isentropically expands to the freestream exhaust pressure. The injection height, h, was determined using a momentum flux balance as shown in Eq. 2.2 (Zukoski and Spaid, 1964).

$$\frac{h}{D_{\text{inj}}\sqrt{C_d}} = \frac{1}{M_\infty}\sqrt{\left(\frac{P_{\text{tj}}}{P_\infty}\right)\left(\frac{\gamma_{\text{j}}}{\gamma_\infty}\right)\left(\frac{2}{C_{P,\,\max}}\right)}\left\{\left(\frac{2}{\gamma_{\text{j}}-1}\right)\left(\frac{2}{\gamma_{\text{j}}+1}\right)\left[1-\left(\frac{P_\infty}{P_{\text{tj}}}\right)^{\frac{\gamma_{\text{j}}-1}{\gamma_{\text{j}}}}\right]\right\}^{0.25} \tag{2.2}$$

Here, D_{inj} and C_d are the injection port diameter and discharge coefficient of the injection port, respectively.

Subscripts ∞ and j indicate values of the primary freestream flow and the secondary jet flow, respectively. A significant limitation of this analysis is that it assumes that a jet is injected into a supersonic cross flow over a flat plate, rather than a nozzle. Furthermore, the computation of the lateral force requires experimental data for the pressure distribution on the infinite flat plate as shown in Eq. 2.3 (Zukoski and Spaid, 1964).

$$F_{yP} = \int_{y=-\infty}^{\infty} \int_{x=-\infty}^{\infty} (P - P_{\infty})\, dx\, dy \tag{2.3}$$

However, no analytical or empirical methods for determining the pressure distribution on a flat plate or a nozzle wall are provided. Thus, Zukoski and Spaid's model cannot directly be used to find the lateral force generated by SITVC.

Transverse Slot - Spaid and Zukoski, 1968

Following the 1964 paper, interest grew in understanding the underlying flow phenomena. Consequently, a new investigation was initiated to examine the two-dimensional SITVC case, where secondary gas was injected through a transverse slot. Figure 2.4 illustrates the pressure distribution and the main flow features in the vicinity of the injection. Key flow phenomena include bow shock formation, flow separation and recirculation zone development upstream of the injection. These features contribute to the wall pressure distribution, which is of particular interest for calculating lateral forces. The pressure rises from the initial pressure, P_1, to a plateau in the separated region, P_{plat}, then rises to another peak just ahead of the injection, P_f.

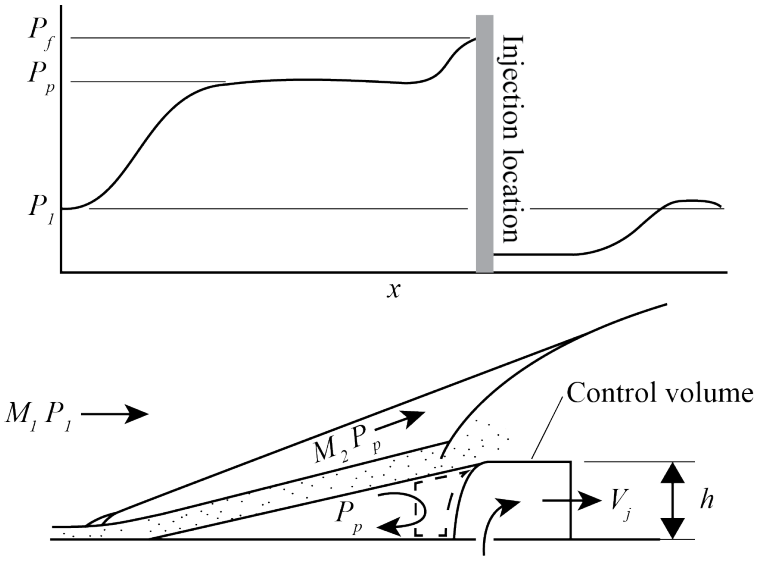

Figure 2.4: Schematic of secondary gas injection through a slot and the associated pressure profile along the wall. Adapted from Spaid and Zukoski (1968).

A momentum balance in the x-direction was applied across the CV to generate an expression for the injection height. The new model required two-dimensional empirical relations. Observations suggested that the separation region upstream of the injection resembled that generated by a forward-facing step. Zukoski (1967) investigated the turbulent boundary layer separation ahead of a two-dimensional forward facing step and found the separation distance, X_s, to be approximately 4.2 times the forward-facing step height as shown in Eq. 2.4:

$$X_s/h = 4.2 \tag{2.4}$$

Additionally, the plateau pressure in the recirculation zone, P_{plat}, was found to depend on the primary flow Mach number according to Eq. 2.5:

$$P_{\text{plat}} = P_1 (0.5M_1 + 1) \tag{2.5}$$

Finally, the average pressure on the face of the FFS, P_f, was related to the Mach number after the oblique shock, M_2, as shown in Eq. 2.6:

$$\frac{P_f}{P_{\text{plat}}} = 1 + \beta' \frac{\gamma M_2^2}{1 + \frac{\gamma-1}{2} M_2^2} \tag{2.6}$$

where $\beta' = 0.062$. As in the 3D case, the pressure distribution was not fully defined and thus could not be integrated to find the lateral force generated.

Wilson and Comparin, 1969

In 1969, Wilson and Comparin theorized that analysis of secondary injection must rely heavily on empirical results due to the complexity of the phenomena. They found effective body models to be most successful in predicting lateral forces due to secondary injection. Although the body shape and dimensions are not directly observed in experiments, they serve as a scaling parameter for calculating the lateral thrust. Wilson and Comparin's model uses a combination of empirical relations and Spaid and Zukoski's blunt body analogy. Most notable, they were the first to define the pressure distribution near the injection port using three distinct regions listed below and shown in Fig. 2.5.

1. **Separation Region**: The boundary layer has separated upstream of the bow shock. The pressure in this region is assumed to be constant and equal to half the characteristic pressure in a shock-separated boundary layer.

2. **Strong Vortex Region**: High-pressure area downstream of the shock characterized by high-vortex flow. The pressure in this region is assumed to be the characteristic pressure.

3. **Jet Region**: The area directly downstream of the injection port that is characterized by separation and reattachment of the secondary jet. This low pressure region, which was defined by assuming an arbitrary point downstream of the injection port, negatively contributes to the lateral force.

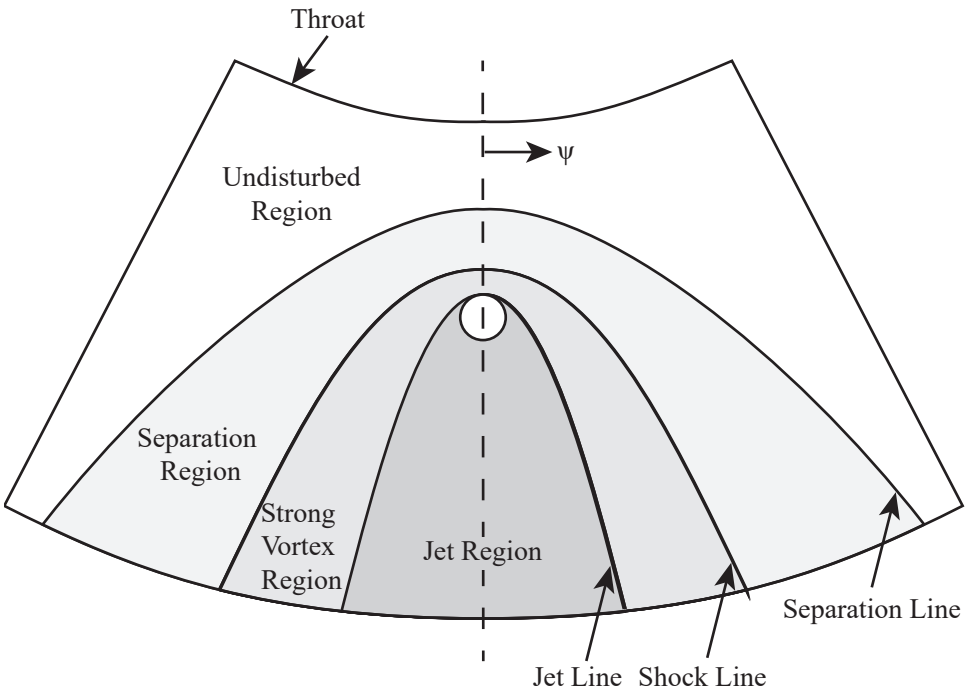

Figure 2.5: Two-dimensional projection of the distinct wall pressure regions in a three-dimensional conical nozzle near the secondary injection site. Adapted from Wilson and Comparin (1969).

The side force contributed by the wall pressure distribution asymmetry is obtained using Eq. 2.7 (Wilson and Comparin, 1969):

$$F_{wy} = 2 \iint (P - P_\infty) \cos\Psi \cos\alpha_n r d\Psi dx \tag{2.7}$$

where P, P_∞, Ψ, and α_n are the wall pressure, isentropic freestream pressure of the primary flow, rotation angle, and the nozzle half-angle. Wilson and Comparin admit that their approach requires significant simplifying assumptions regarding the nozzle wall pressure distribution in all three regions.

Validation was attempted using hot-gas injection data from a NASA-sponsored experiment. However, significant sources of experimental error, including a crack in the injection valve, yielded unsatisfactory validation of results. Comparison to experimental data under a variety of conditions is required to evaluate the accuracy of this model.

Evry, 2008

Maarouf (2008) and Sellam et al. (2012) adopted the blunt body analogy for an axisymmetric nozzle with both circular and slot injections. Building on the work of Mangin (2006), they expanded the analysis from a 2D to a conical nozzle. The secondary injection is modelled as a solid obstruction with a quarter-sphere nose with a half-cylinder body, as depicted in Fig. 2.6.

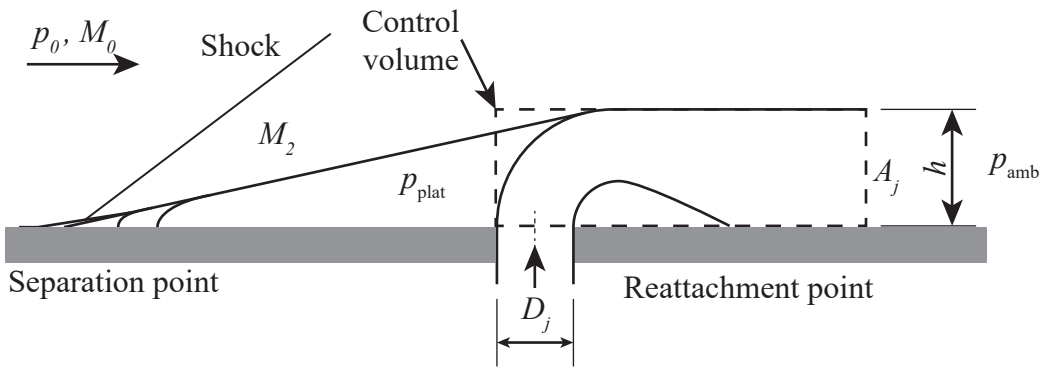

Figure 2.6: Control volume for the computation of injection height. Adapted from Zmijanovic et al. (2013).

A momentum balance in the x-direction is applied to determine the characteristic height, h. The momentum balance on the control volume illustrated in Fig. 2.6 is given in Eq. 2.8.

$$\sum F_x = F_{x1} + F_{x2} = \dot{m}_{\mathrm{j}} V_{\mathrm{j,\,e}} \tag{2.8}$$

The right-hand side of the equation represents the momentum of the jet as it exits the control volume. This is computed using Eqs. 2.9 to 2.11. Note that subscripts "j" and "e" indicate secondary jet properties and properties at the exit of the control volume, respectively. Additionally, the control volume exit does not necessarily coincide with the exit of the main nozzle.

$$V_{\mathrm{j,\,e}} = \sqrt{\gamma_{\mathrm{j}} R_{\mathrm{j}} T_{\mathrm{tj}} \frac{2}{\gamma_{\mathrm{j}} - 1} \left[1 - \left(\frac{P_{\mathrm{j,\,e}}}{P_{\mathrm{tj}}} \right)^{\frac{\gamma_{\mathrm{j}}-1}{\gamma_{\mathrm{j}}}} \right]} \tag{2.9}$$

$$\dot{m}_{\mathrm{j}} = C_d \frac{\pi}{4} D_{\mathrm{inj}}^2 \frac{P_{\mathrm{tj}}}{\sqrt{T_{\mathrm{tj}}}} \sqrt{\frac{\gamma_{\mathrm{j}}}{R_{\mathrm{j}}}} \left(\frac{\gamma_{\mathrm{j}} + 1}{2} \right)^{-\frac{\gamma_{\mathrm{j}}+1}{2(\gamma_{\mathrm{j}}-1)}} \tag{2.10}$$

$$\dot{m}_{\mathrm{j}} V_{\mathrm{j,\,e}} = C_d \frac{\pi}{2} D_{\mathrm{inj}}^2 P_{\mathrm{tj}} \gamma_{\mathrm{j}} \left(\frac{2}{\gamma_{\mathrm{j}} + 1} \right)^{\frac{1}{\gamma_{\mathrm{j}}-1}} \sqrt{\left(\frac{1}{\gamma_{\mathrm{j}}^2 - 1} \right) \left[1 - \left(\frac{P_{\mathrm{j,\,e}}}{P_{\mathrm{tj}}} \right)^{\frac{\gamma_{\mathrm{j}}-1}{\gamma_{\mathrm{j}}}} \right]} \tag{2.11}$$

The forces acting on the upstream and downstream control volume faces, F_{x1} and F_{x2}, are given by Eqs. 2.12 and 2.13, respectively.

$$F_{x1} = \frac{\pi}{2} h^2 \left(P_{\mathrm{plat}} + \frac{1}{2} q_\infty C_{\mathrm{P,\,max}} \right) \tag{2.12}$$

$$F_{x2} = -\frac{\pi}{2} h^2 P_{\mathrm{av}} \tag{2.13}$$

Here, q_∞ and $C_{P\mathrm{max}}$ are the dynamic pressure and maximum pressure coefficient of the freestream flow

evaluated at the separation location. P_{av} is the average pressure acting on the downstream face of the control volume. Substituting in Eqs. 2.9 to 2.13 into Eq. 2.8 and rearranging for the injection height, h, yields Eq. 2.14:

$$h = D_{\text{inj}} \sqrt{\frac{C_d \gamma_j P_{\text{tj}} \left(\frac{2}{\gamma_j+1}\right)^{\frac{1}{\gamma_j-1}} \sqrt{\left(\frac{1}{\gamma_j^2-1}\right)\left[1-\left(\frac{P_{\text{j,e}}}{P_{\text{tj}}}\right)^{\frac{\gamma_j-1}{\gamma_j}}\right]}}{P_{\text{plat}} - P_{\text{av}} + \frac{1}{2} q_\infty C_{P,\text{max}}}} \tag{2.14}$$

$P_{\text{j,e}}$ is the secondary jet pressure as it exits the CV. Maarouf defines the exit pressure as the ambient pressure for over-expanded nozzles, and the isentropically-determined nozzle exit pressure for under-expanded nozzles.

The injection height is dependent on the primary flow properties at the boundary layer separation location, x_{s}. However, the separation location is dependent on the injection height. The interdependence of these parameters, caused by the changing area of the nozzle, requires iterative calculations to resolve according to the simplified procedure in Eq. 2.15.

$$\begin{aligned} &\rightarrow h = \mathcal{F}(P_{\text{plat}}, C_{P,\text{max}}, q_\infty) \\ &\quad P_{\text{plat}}, C_{P,\text{max}}, q_\infty = \mathcal{F}(P_\infty, M_\infty) \\ &\quad P_\infty, M_\infty = \mathcal{F}(x_{\text{s}}) \\ &\quad x_{\text{s}} = \mathcal{F}(h) \end{aligned} \tag{2.15}$$

Key differences between the original blunt body model (Zukoski and Spaid, 1964) and this extended version are summarized in Tab. 2.1.

Table 2.1: Comparison of blunt body models by Zukoski and Spaid (1964) and Maarouf (2008).

Study	**Zukoski and Spaid (1964)**	**Maarouf (2008)**
Valid for...	circular injection over flat plate.	circular or slot injection in an axisymmetric nozzle.
Secondary jet pressure at CV exit...	equals primary flow freestream pressure.	is dependent on nozzle operating regime (under- or over-expanded).
Primary flow properties are...	constant and known.	dependent on x_{s}, requiring iterative calculations.

Empirical correlations for separated flows are required to resolve additional unknown parameters. Maarouf compares and summarizes the results of various empirical empirical relations for separated flows

(Schmucker, 1984; Summerfield et al., 1954; Zukoski, 1967) and free interaction theory (Carrière et al., 1969; Chapman et al., 1958). In addition, geometric constraints are imposed on the oblique separation shock. Specifically, the separation line is assumed to be tangential to the quarter-sphere nose of the blunt body. Note that the imposition of geometric constraints, simplifying assumptions and empirical relations may lead to errors in the results if they are contradictory or inconsistent.

Given that the shape and dimensions of the equivalent obstruction are defined, the next step is to define the wall pressure distribution. Maarouf divides the nozzle wall in the vicinity of the injector port into distinct regions. He determines the boundary layer separation curve geometry by extending the hyperbolic shock shape determined by Billig (1967) to the boundary layer separation curve. Once the wall pressure distribution is fully defined, numerical integration is performed to calculate the lateral force due to the wall pressure asymmetry. This analysis involves a combination of empirical relations, geometric constraints, control volume analysis, boundary layer separation, and numerical integration making it the most difficult to implement of the models discussed.

Recently, other researchers have tried to replicate the model but encountered difficulties that led them to introduce additional assumptions and simplifications (Younes and Hickey, 2020). This suggests that the original model may have had complexities or dependencies that were not fully captured or articulated, making it challenging for others to reproduce the results. Challenges in reproducibility demonstrate the need for further research on blunt-body modelling techniques for SITVC.

Furthermore, assessment of the model assumptions indicates that conservation of mass is not enforced across the control volume. Instead, assumptions regarding the secondary jet exit pressure are introduced. According to Sellam et al. (2012):

> The pressure (P_{av}) that dominates the area at the exit of the control volume follows the same functioning-regime of the nozzle. This pressure should be equal to the ambient pressure (P_{amb}) in the case of an over-expanded nozzle or equal to the isentropic pressure of the nozzle (P_j) in the case of an adapted or under-expanded nozzle ... $P_j = P_{av}$ [is] the stagnation pressure at the exit of the control volume. (p. 197-198)

The Evry lab developed this model and validated it through cold-gas experiments conducted in a blow-down wind tunnel. Both the experimental force data and the Evry model predictions were reported (Sellam et al., 2012). Attempts to replicate their model using the published data did not yield the same predictions. However, it remains valuable to review the case. Given an ambient pressure of 8.0 kPa and a primary flow total pressure of 300 kPa, a Mach 3 undisturbed nozzle exit pressure is approximately 8.2 kPa. Given these inputs, Dr. Sellam has indicated P_j equals 105.7 kPa (personal communication, October 20, 2023). Without

details on how this value was determined, its exact derivation remains unclear. Despite this, P_j has been used in the following calculations, assuming it accurately represents the intended conditions.

Given that the stagnation properties of the flow remain constant, the mass flow rate is proportional to the area and Mach number as shown in Eq. 2.16.

$$\dot{m} \propto AM\left(1 + \frac{\gamma - 1}{2}M^2\right)^{-\frac{\gamma+1}{2(\gamma-1)}} \tag{2.16}$$

Using values provided by Dr. Sellam (personal communication, October 20, 2023) including the injection port diameter, D_{inj} = 6.15 mm, the injection height, h = 8.64 mm, and secondary jet exit pressure of $P_{j,\,e}$ = 105.7 kPa, the ratio of mass flow rates across the control volume is determined.

$$\frac{\dot{m}_e}{\dot{m}_{in}} \approx 3.7 \tag{2.17}$$

The mass flow rate that exits the control volume is approximately **3.7 times** the mass flow rate that enters. This ratio indicates that conservation of mass of the secondary jet was not included as a governing equation in their model. Instead, an assumption of CV exit pressure was used to close the model.

Deng et al., 2014

Deng et al. (2014) investigated SITVC using the blunt-body analogy, building on the works of Sellam et al. (2012) and Zukoski and Spaid (1964). Their model defines the control volume's shape and dimensions and calculates the boundary layer separation location. However, it stops short of fully defining the pressure distribution on the nozzle wall or computing the lateral thrust. Despite these limitations, their work remains valuable for review. This model combines control volume analysis with assumptions and forward-facing step empirical relations to estimate the separation position. The control volume used in their analysis is illustrated in Fig. 2.7, and the momentum balance applied is given in Eq. 2.18.

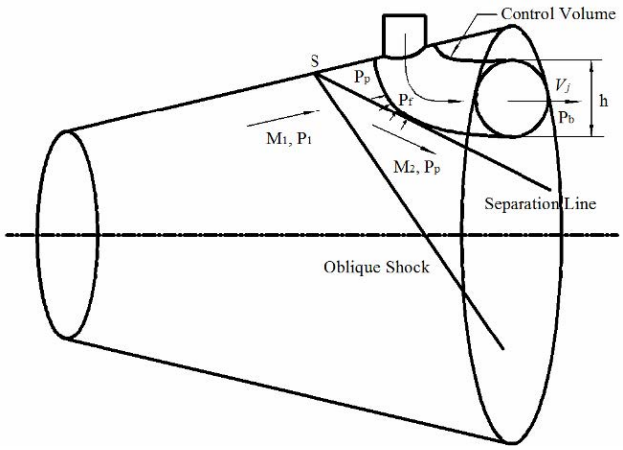

Figure 2.7: Control volume for the computation of injection height. From Deng et al. (2014).

$$\sum F_x = F_{x1} + F_{x2} = \dot{m}_j V_j \tag{2.18}$$

The average pressure on the upstream face is derived from forward-facing step relations and acts over a projected area of a half-circle, $\frac{\pi}{2}h^2$. The resulting drag force on this upstream control volume face, F_{x1}, is calculated according to Eq. 2.19:

$$F_{x1} = \frac{\pi}{2}h^2 P_f \tag{2.19}$$

The exit area of the control volume is defined as an oval with semi-axes h and $4h$. Given the back pressure, P_b, the force on the downstream face, F_{x2}, is given by Eq. 2.20.

$$F_{x2} = -4\pi h^2 P_b \tag{2.20}$$

The model is limited to cases where the secondary injection is sonic through the port, making the inlet mass flow rate directly proportional to the injection port area.

$$\dot{m}_{\text{in}} \propto \frac{\pi}{4}D_{\text{inj}}^2 \tag{2.21}$$

In addition to defining the control volume shape, Deng et al. (2014) assume that the secondary jet exits the control volume at sonic speeds. They argue that the jet flow becomes subsonic as it turns, then accelerates through the recompression shock, becoming supersonic again as it reattaches to the wall. By assuming sonic flow at the control volume exit, the mass flow rate exiting the control volume becomes directly proportional to the oval-shaped exit area.

$$\dot{m}_e \propto 4\pi h^2 \tag{2.22}$$

Given the reported injection port diameter of $D_{inj} = 6$ mm and an approximate injection height of 10 mm (derived from reported separation distances), the ratio of mass flow rate across the control volume is determined:

$$\frac{\dot{m}_e}{\dot{m}_{in}} \approx 44 \tag{2.23}$$

Thus, the mass flow rate that exits the control volume is approximately **44 times** the mass flow rate that enters. This substantial discrepancy undermines the reliability of the analysis, and may compromise the accuracy of final thrust vector predictions. However, since the model does not provide a method to calculate forces, the impact of neglecting to uphold continuity on the final results cannot be evaluated directly.

2.4 Summary

Chapter 2 provided an overview of the fundamental flow dynamics involved in secondary injection thrust vector control within nozzle systems, establishing a foundation for evaluating existing models. Following this, the prominent models in the literature were examined, with most shown to rely on the blunt-body analogy. Wu et al. (1961) set an early benchmark for SITVC analysis by applying fundamental conservation laws—mass, momentum, and energy—offering a more physics-based foundation compared to many later models. However, the accuracy of Wu's predictions was limited. Wu's model was constrained by over-simplifications in representing the interactions between the primary and secondary flows, and it could not reliably predict lateral thrust and flow behaviour with high accuracy. Additionally, while Wu's approach was pioneering in its use of conservation principles, it did not shed light on the flow features in an SITVC nozzle. A key limitation across nearly all models—excluding Wu et al. (1961)—was the absence of mass conservation enforcement, which was substituted with assumptions about secondary jet conditions at the control volume exit. This assumption-based approach introduced significant deviations in mass conservation. For example, using the Evry model, the exiting mass flow rate is almost four times the mass that enters the control volume, while Deng's model produces an even larger deviation, with an exit mass flow rate of 44 times the entry rate. These discrepancies underscore the inaccuracies in predicting the secondary jet's interaction with the primary flow.

Moreover, the current leading model developed by the Evry group, while comprehensive, was identified as being challenging to reproduce due to its complexity and limited accessibility to the precise details needed for full validation. These shortfalls underscore the need for a more robust and accessible solution that

not only conserves mass and momentum across the control volume but also offers clear and reproducible methodologies. This necessity motivates the development of a new model, which addresses these limitations and will be introduced in the following chapter.

Chapter 3

Modelling of SITVC

3.1 Overview

Purpose of Modelling

Modelling provides a fast, cost-effective approach to estimating the thrust vector arising from the injection of a jet into a supersonic axisymmetric nozzle. This method is especially valuable in early design phases, offering speed and affordability over computational and experimental techniques. It is also particularly suitable for integration into six degree-of-freedom rocket simulation frameworks.

Building on the foundational works of Wu et al. (1961); Maarouf (2008); Mangin (2006); Zukoski (1967), a semi-empirical model was developed to compute the thrust vector for three-dimensional converging diverging nozzles. Named the mass- and momentum-conserved secondary injection model (MMC-SIM), it enforces both mass and momentum conservation, avoiding the need for other assumptions seen in subsequent models.

Overview of MMC-SIM

MMC-SIM applies the blunt-body analogy to predict the thrust vector in SITVC, uniquely enforcing conservation of mass to minimize assumptions. This low-fidelity model for computing the thrust vector was developed for three-dimensional converging-diverging nozzles. It models the secondary jet as an equivalent blunt body with a quarter-sphere nose of radius h, referred to as the injection height. SITVC-induced shock patterns resemble those from supersonic flow over blunt bodies, as discussed in Section 2.3.2. Traditional blunt body models determine the characteristic height, h, by equating the drag force with the jet's momentum as it exits the control volume. This approach requires additional assumptions about the jet's exit

velocity or pressure (Deng et al., 2014; Maarouf, 2008; Zukoski and Spaid, 1964). In contrast, MMC-SIM introduces a novel approach by enforcing mass conservation. This distinctive feature minimizes assumptions, grounding MMC-SIM more firmly in real-life physical principles and enhancing its predictive accuracy.

Complexity of SITVC Flow Structures

The three-dimensional flow structure produced by SITVC is inherently complex, involving a horseshoe vortex, a pair of counter-rotating vortices, mixing between the jet and freestream, and recirculation zones. Detailed analytical modelling of these individual phenomena and their interactions is challenging. Instead, the model can be greatly simplified if only the features that contribute significantly to the thrust vector are considered. These features of interest, including the adverse pressure gradient and boundary layer separation, lie near the nozzle wall and may be approximated using a combination of analytical modelling and empirical relations. Gas injection into the nozzle becomes more amenable to modelling provided simplifying assumptions are employed.

Modelling Simplifications and Assumptions

MMC-SIM applies the blunt-body analogy and the following assumptions for thrust vector predictions:

1. The secondary jet is deflected by the primary freestream until it is parallel to the nozzle wall.
2. The equivalent body has a quarter-sphere nose.
3. No mixing occurs between the primary and secondary flows.
4. Shear stresses on the control volume are negligible.
5. The boundary layer thickness is much less than the injection height.

Overview of MMC-SIM Structure

MMC-SIM consists of two subroutines as shown in Fig. 3.1. The first subroutine calculates the injection height, h, and the boundary layer separation position, x_s, using nozzle geometry and flow properties as inputs. These intermediate results are passed to the second subroutine, which determines the thrust by numerically integrating the pressure along the nozzle wall. Full details of each subroutine are provided in Sections 3.2 and 3.3. Additionally, the complete MMC-SIM code is available for reference in Appendix C.

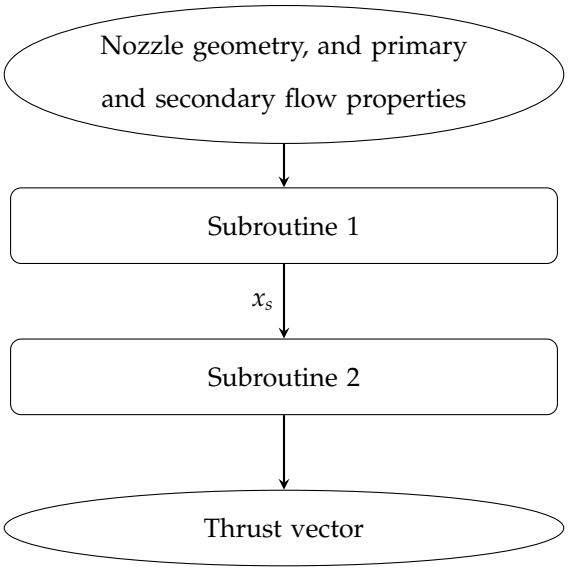

Figure 3.1: Flowchart describing execution process of MMC-SIM.

3.2 Subroutine 1: Injection Height Determination

The foundations of the blunt-body analogy were laid by Spaid and Zukoski (1968) in their extensive work on sonic jet injection over a flat plate. Deng et al. (2014) and Maarouf (2008) expanded this model to include injection into an axisymmetric nozzle. The current model builds upon these contributions.

A control volume encompassing the secondary jet is shown in Fig 3.2. The centre of the secondary injection port is located at x_{inj}. Note that the nozzle divergence (half-angle) is assumed to be small and is neglected. The oncoming primary flow is deflected through the oblique shock upstream of the obstruction by the turning angle, δ. The onset of boundary layer separation occurs at x_s.

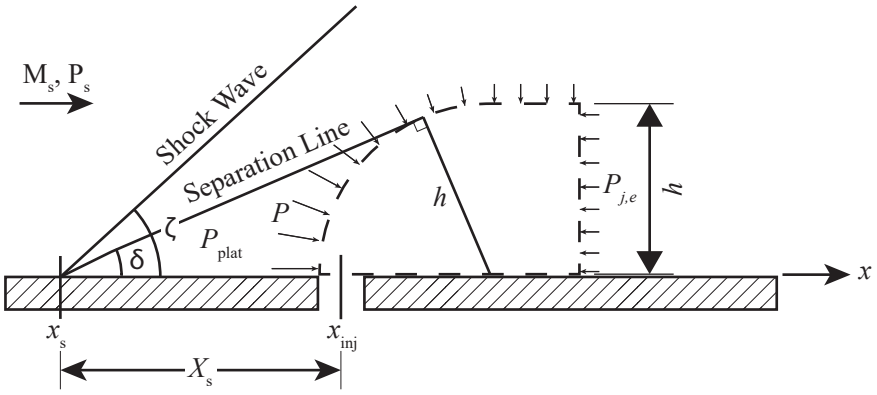

Figure 3.2: Control volume encompassing equivalent body with quarter-sphere nose. Adapted from Zmijanovic et al. (2013).

The boundary layer separation distance, X_s, which describes the distance from the separation position to the injection port is defined by assuming that the deflected flow is tangential to the quarter-sphere nose according to Eq. 3.1.

$$X_s = h\left(\frac{1}{\sin\delta} - 1\right) \tag{3.1}$$

Note that Eq. 3.1 neglects the thickness of the jet. The boundary layer separation position, x_s, is determined using Eq. 3.2.

$$x_s = x_{\text{inj}} - X_s \tag{3.2}$$

Supersonic flow over forward-facing step experiments show that in the separated region, the pressure may be assumed constant. This so-called plateau pressure, P_{plat}, is dictated by the freestream deflection angle, δ. Jet-induced separation exhibits similar behaviour. However, given that the obstacle size is unknown, empirical relations are used to obtain the plateau pressure from the primary flow properties at x_s. The static pressure of the freestream after the oblique shock, P_{plat} may be computed using the empirical relation presented in Eq. 3.3 (Zukoski, 1967):

$$P_{\text{plat}} = P_s(0.5M_s + 1) \tag{3.3}$$

Subscript s indicates primary flow properties at the separation position, x_s. A further increase in pressure occurs just ahead of the obstruction. Equation 3.4 is used to obtain the upstream pressure acting on the obstruction, P_f. The proportionality constant β' was set to 0.062 based on experimental force data (Zukoski, 1967). The pressure on the upstream face of the control volume does not show dependence on β' if the obstacle height is larger than the boundary layer thickness, $h/\delta > 1$.

$$P_f = P_{\text{plat}}\left(1 + \beta'\frac{\gamma M_{\text{plat}}^2}{1 + \frac{\gamma-1}{2}M_{\text{plat}}^2}\right) \tag{3.4}$$

The pressure ratio across the oblique shock, P_{plat}/P_s, is used to find the shock angle, ζ, and the flow deflection angle according to Eqs. 3.5 and 3.6 (John and Keith, 2006).

$$\sin\zeta = \sqrt{\frac{\frac{P_{\text{plat}}}{P_s}(\gamma+1) + (\gamma-1)}{2\gamma M_s^2}} \tag{3.5}$$

$$\tan\delta = \cot\zeta\frac{M_s^2\sin^2\zeta - 1}{\frac{\gamma+1}{2}M_s^2 - (M_s^2\sin^2\zeta - 1)} \tag{3.6}$$

Finally, the Mach number of the freestream flow after the oblique shock is obtained from Eq. 3.7.

$$M_{\text{plat}}^2 \sin^2(\delta - \zeta) = \frac{(\gamma - 1)M_s^2 \sin^2 \delta + 2}{2\gamma M_s^2 \sin^2 \delta - (\gamma - 1)} \tag{3.7}$$

3.2.1 Conservation of Mass

The secondary mass flow into the control volume is known and is defined by the secondary injection port flow conditions as follows:

$$\dot{m}_{\text{in}} = \iint \rho \boldsymbol{U} \cdot \boldsymbol{n} dS = \rho_{\text{in}} \boldsymbol{U}_{\text{in}} A_{\text{port}} \tag{3.8}$$

where the subscript "in" denotes secondary jet conditions at the injection port with area A_{port}. Assuming that no mixing occurs between the primary and secondary flows, the mass flow rates entering and exiting the control volume are equal by conservation of mass.

$$\dot{m}_{\text{j}} = \dot{m}_{\text{in}} = \dot{m}_{\text{e}} \tag{3.9}$$

Additionally, the mass flow rate across the exit face is expressed using stagnation properties as follows:

$$\dot{m}_{\text{e}} = \frac{P_{\text{tj}}}{\sqrt{T_{\text{tj}}}} A_{\text{e}} M_{\text{j, e}} \sqrt{\frac{\gamma_{\text{j}}}{R_{\text{j}}}} \left(1 + \frac{\gamma_{\text{j}} - 1}{2} M_{\text{j, e}}^2\right)^{-\frac{\gamma_{\text{j}}+1}{2(\gamma_{\text{j}}-1)}} \tag{3.10}$$

Subscript "j" indicates secondary jet properties. Note that the exit area of the control volume is assumed to be a half-circle with radius h.

$$A_{\text{e}} = \frac{\pi}{2} h^2 \tag{3.11}$$

Rearranging Eq. 3.10 yields an expression for the injection height derived from conservation of mass as shown in Eq. 3.12.

$$\boxed{h_{\text{mass}} = \left[\sqrt{\frac{R_{\text{j}}}{\gamma_{\text{j}}}} \frac{2}{M_{\text{j, e}} \pi} \frac{\sqrt{T_{tj}}}{P_{tj}} \dot{m}_{\text{j}} \left(1 + \frac{\gamma_{\text{j}} - 1}{2} M_{\text{j, e}}^2\right)^{\frac{\gamma_{\text{j}}+1}{2(\gamma_{\text{j}}-1)}} \right]^{\frac{1}{2}}} \tag{3.12}$$

Note that the subscript "mass" indicates that the height is derived from a conservation of mass assumption. Equation 3.12 establishes the first constraint on the injection height, h. However, the jet exit conditions (specifically Mach number, $M_{\text{j, e}}$) remain unknown. All other parameters in this equation are known.

3.2.2 Conservation of Momentum

Applying momentum conservation yields the second constraint on the injection height. The net force in the x-direction, $\sum F_x$, is balanced by the momentum of the exiting jet, $\dot{m}_e V_{j,e}$, as established in Eq. 3.13.

$$\sum F_x = F_{x1} + F_{x2} = \dot{m}_j V_{j,e} \tag{3.13}$$

Here, F_{x1}, and F_{x2} represent the x-components of the forces on the upstream and downstream faces of the control volume, respectively. To evaluate F_{x1}, the pressure on the upstream face of the control volume is integrated.

$$F_{x1} = \iint P \sin\Theta \sin\Phi dS_{\text{upstream}} \tag{3.14}$$

The differential area over a quarter sphere is illustrated in Fig. 3.3 and is calculated according to Eq. 3.15. Angles Θ and Φ are defined as illustrated in the figure.

$$dS_{\text{upstream}} = h^2 \sin\Theta d\Theta d\Phi \tag{3.15}$$

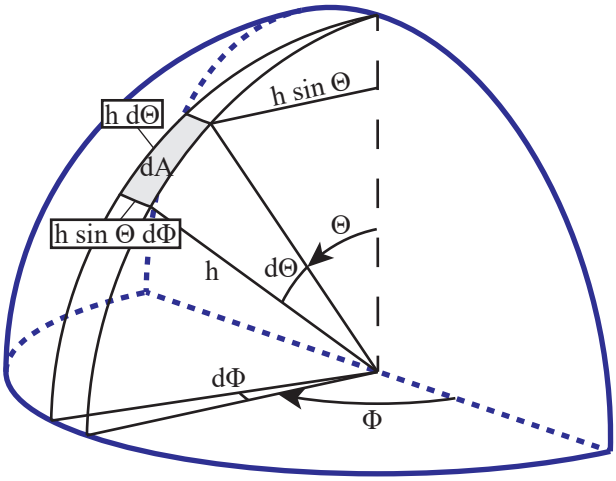

Figure 3.3: Schematic of area integration over a quarter sphere.
Adapted from Rowlands (2017).

Recalling the modified Newtonian theory (see Appendix A.6), the pressure on an inclined blunt body is given by Eq. 3.16:

$$P = q_{\text{plat}} C_{P\text{max}} \sin^2\Theta \sin^2\Phi + P_{\text{plat}} \tag{3.16}$$

Here, subscript "plat" denotes primary flow properties in the plateau region. $C_{P\text{max}}$ is likewise evaluated in

the plateau region using using Eq. A.24. Substituting Eqs. 3.15 and 3.16 into Eq. 3.14 yields the following:

$$F_{x1} = \int_0^{\pi} \int_0^{\pi/2} \left(q_{\text{plat}} C_{P\text{max}} \sin^2\Theta \sin^2\Phi + P_{\text{plat}} \right) h^2 \sin^2\Theta \sin\Phi d\Theta d\Phi \tag{3.17}$$

Evaluating the integral yields Eq. 3.18 for the pressure force on the upstream face of the control volume.

$$F_{x1} = \frac{\pi}{2} h^2 \left(\frac{1}{2} q_{\text{plat}} C_{P\text{max}} + P_{\text{plat}} \right) \tag{3.18}$$

Next, the force acting on the downstream face of the control volume may be determined using Eq. 3.19.

$$F_{x2} = \int P dA = -\frac{\pi}{2} h^2 P_b \tag{3.19}$$

Here, P_b is the back-pressure acting on the downstream control volume face, which equals the undisturbed nozzle exit pressure, P_{e}. Lastly, Eq. 3.20 provides the exiting jet momentum.

$$\dot{m}_{\text{j}} V_{\text{j, e}} = \dot{m}_{\text{j}} M_{\text{j, e}} \sqrt{\gamma_{\text{j}} R_{\text{j}} \frac{T_{\text{tj}}}{1 + \frac{\gamma_{\text{j}}-1}{2} M_{\text{j, e}}^2}} \tag{3.20}$$

Combining Eqs. 3.18, 3.19, and 3.20 yields a relation for the injection height derived from conservation of momentum:

$$\boxed{h_{\text{momentum}} = \left[\frac{2}{\pi} \frac{\dot{m}_{\text{j}} M_{\text{j, e}} \sqrt{\gamma_{\text{j}} R_{\text{j}} T_{\text{j, e}}}}{\frac{1}{2} q_{\text{plat}} C_{P\text{max}} + P_{\text{plat}} - P_{\text{b}}} \right]^{1/2}} \tag{3.21}$$

Note that the subscript "momentum" indicates that the height is derived from a conservation of momentum assumption. As in the equation derived from continuity, the jet exit condition remains unknown ($M_{\text{j, e}}$, $T_{\text{j, e}}$). All other parameters in Eq. 3.21 are known.

3.2.3 Solving for Injection Height

Conservation of mass and momentum have been used to derive Eqs. 3.12 and 3.21 for the injection height. Both functions are dependent on the secondary jet exit condition, which remains unknown. To resolve this, the two equations are solved simultaneously. This enforces both conservation of mass and momentum conditions and yields the injection height, h, and the jet exit conditions, $M_{\text{j, e}}$. The MATLAB function "fzero" is used to find the root (in this case $M_{\text{j, e}}$) that satisfies the following condition:

$$h_{\text{mass}} - h_{\text{momentum}} = 0 \tag{3.22}$$

The procedure to solve for the injection height is iterative. This is because freestream properties at the separation location are required, but the separation location is unknown. Given the changing area nature of the nozzle, the freestream properties vary with x-position. The procedure is schematically shown in Fig. 3.4.

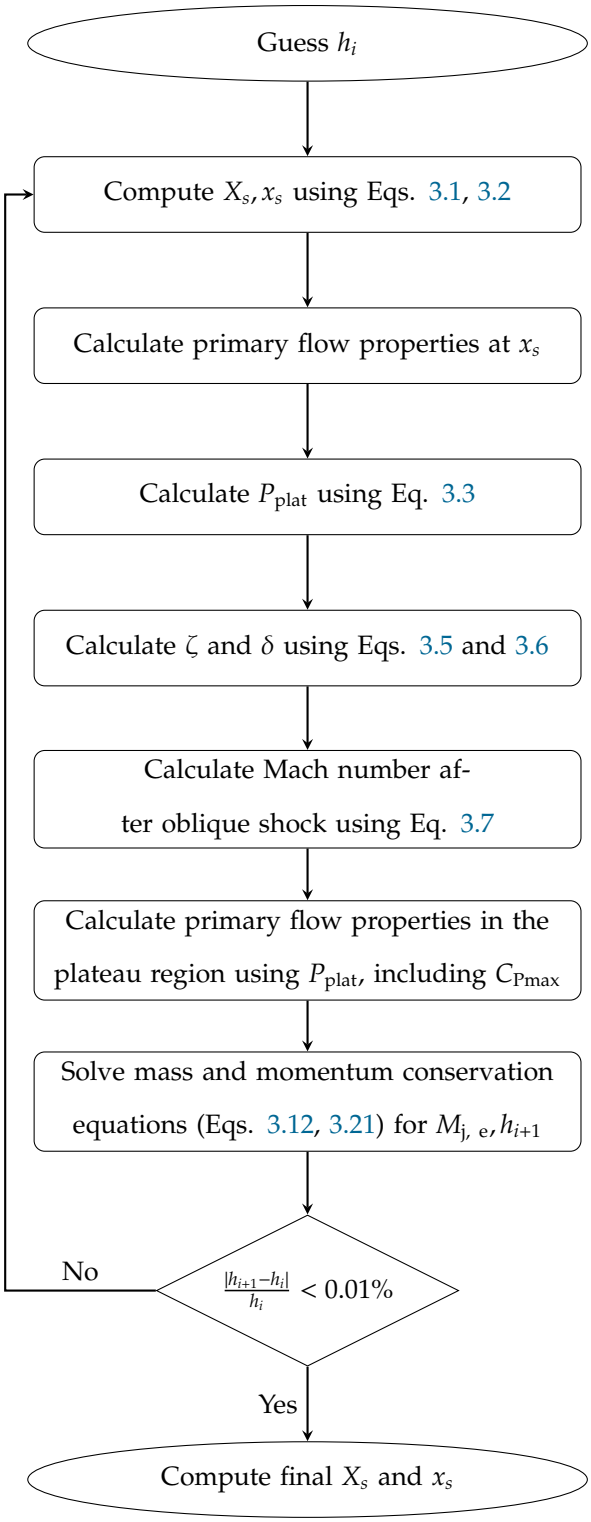

Figure 3.4: Flowchart describing subroutine 1, including inputs and outputs, for estimation of the separation position, x_s.

3.3 Subroutine 2: Force Determination

The nozzle thrust is composed of the primary and secondary jet momentum contributions and the wall pressure contributions. The wall pressure distribution is divided into three distinct regions as illustrated in Fig. 3.5: (I) undisturbed nozzle at P_{isen}, (II) separated region at P_{plat}, and (III) elevated pressure region at P_{f}.

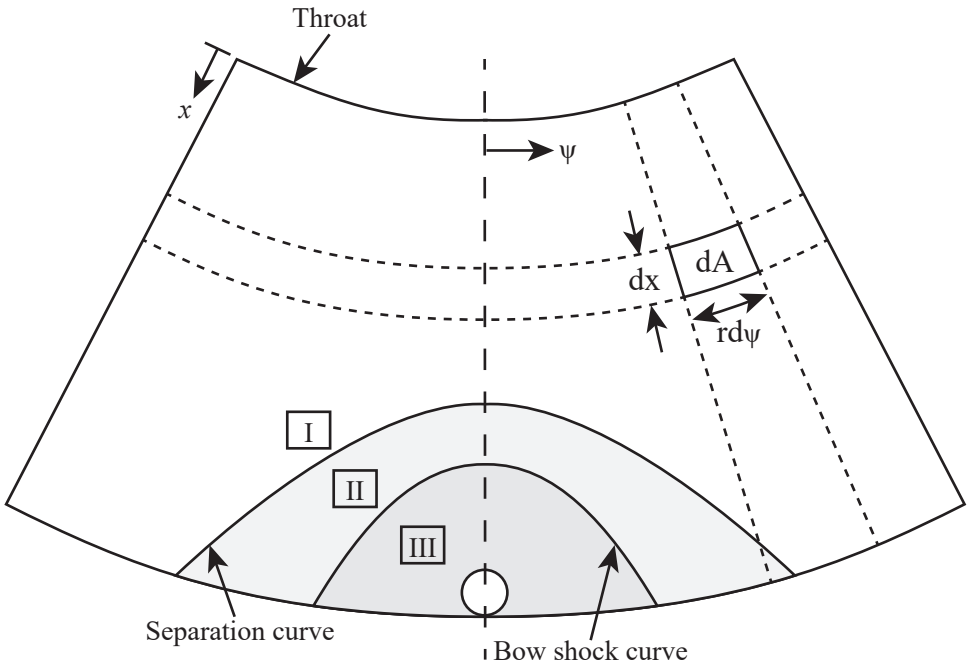

Figure 3.5: Wall pressure distribution schematic in vicinity of secondary injection for conical nozzle.

The thrust vector may be broken up into the axial and lateral components, denoted F_x and F_y, respectively. The x-component is parallel to the rocket axis, while the y-component is perpendicular. They are calculated according to Eqs. 3.23 and 3.24, respectively.

$$F_x = F_{x,\,\text{throat}} + F_{x,P} - P_{\text{amb}} A_{\text{e}} \tag{3.23}$$

$$F_y = F_{y,\,\text{jet}} + F_{y,P} \tag{3.24}$$

Here, $F_{x,\,\text{throat}}$ and $F_{y,\,\text{jet}}$ are the primary jet momentum at the nozzle throat, and the secondary jet momentum at the injector port, respectively. $F_{x,P}$ and $F_{y,P}$ represent the x- and y-components of the force due to the asymmetric wall pressure distribution, respectively. The primary jet momentum is calculated at the throat as shown in Eq. 3.25:

$$F_{x,\,\text{throat}} = \dot{m} V_{\text{throat}} + P_{\text{throat}} A_{\text{throat}} \tag{3.25}$$

For a secondary jet injected perpendicular to the nozzle axis, the momentum contributions to the thrust are calculated according to Eq. 3.26:

$$F_{y,\,\mathrm{jet}} = \dot{m}_\mathrm{j} V_\mathrm{j} + \left(P_\mathrm{j} - P_{\infty,x\mathrm{IP}}\right) A_\mathrm{port} \tag{3.26}$$

Here, P_j and $P_{\infty,x\mathrm{IP}}$ are the pressure of the secondary jet at the injection port, and the pressure of the undisturbed primary flow at the injection port plane, respectively. Numerical integration of the pressure over the nozzle wall is performed to obtain the pressure contributions, $F_{x,P}$ and $F_{y,P}$.

3.3.1 Pressure Contribution to the Thrust Vector

Given a continuous pressure distribution on an area, the force vector may be determined using Eq. 3.27.

$$\boldsymbol{F}_P = \int P \boldsymbol{n} dS \tag{3.27}$$

However, the pressure distribution over the nozzle wall is discretized into a grid of cells, each defined by indices m and n, corresponding to the x-axial and Ψ-angular positions, respectively. Numerical integration is performed over these discrete cells to approximate the total pressure contribution across the surface. In Eq. 3.27, the unit outward normal, $\boldsymbol{n}$, is defined by rotating the vector $(0, 1, 0)$ by the nozzle half-angle, α_n, about the z-axis, and by ψ_n about the x-axis. The rotation matrices are provided in Eq. 3.28.

$$\boldsymbol{R}_x(\theta_x) = \begin{bmatrix} 1 & 0 & 0 \\ 0 & \cos\theta_x & -\sin\theta_x \\ 0 & \sin\theta_x & \cos\theta_x \end{bmatrix}, \quad \boldsymbol{R}_y(\theta_y) = \begin{bmatrix} \cos\theta_y & 0 & \sin\theta_y \\ 0 & 1 & 0 \\ -\sin\theta_y & 0 & \cos\theta_y \end{bmatrix}, \quad \boldsymbol{R}_z(\theta_z) = \begin{bmatrix} \cos\theta_z & -\sin\theta_z & 0 \\ \sin\theta_z & \cos\theta_z & 0 \\ 0 & 0 & 1 \end{bmatrix} \tag{3.28}$$

Thus, the unit outward normal of each cell with index n is calculated using Eq. 3.29:

$$\boldsymbol{n}_n = \boldsymbol{R}_x(\psi_n)\boldsymbol{R}_z(\alpha_\mathrm{n}) \begin{bmatrix} 0 \\ 1 \\ 0 \end{bmatrix} \tag{3.29}$$

From Fig. 3.5, the cell area is calculated using the nozzle radius, r_m, according to Eq. 3.30:

$$dS_m = r_m d\Psi dx \tag{3.30}$$

The force on each cell, indexed by (m, n) is calculated using Eq. 3.31:

$$d\boldsymbol{F}_{P,mn} = P_{mn}\boldsymbol{n}_n r_m d\Psi dx \tag{3.31}$$

The overall force vector due to the wall pressure distribution, $\boldsymbol{F}_P$, is calculated by summing over the nozzle length L for index m, and the full angular range of 360° for index n, as follows:

$$\boldsymbol{F}_P = \sum_m \sum_n P_{mn}\boldsymbol{n}_n r_m d\Psi dx \tag{3.32}$$

The pressure distribution on each (m, n)-indexed cell is elliptically interpolated between the undisturbed nozzle pressure and the pressure of each region (P_{plat} or P_f) as shown in Eq. 3.33.

$$P_{mn} = P_{m,\text{isen}} + \left(P_{m,\text{isen}} - P_{\text{region}}\right)\sqrt{1 - \left(\frac{\psi_n r_m}{\psi_{m,\max} r_m}\right)^2} \tag{3.33}$$

Here, $\psi_{m,\max}$ describes the angular position of each region boundary, as described in the following section.

3.3.2 Region Boundaries on the Nozzle Wall

The nozzle wall is separated into three distinct regions in order to define the pressure distribution as shown in Fig. 3.5. These regions are delineated by the bow shock curve, and the separation curve as illustrated in three-dimensions in Fig. 3.6a. The shock shape around a spherical obstruction was predicted by Billig (1967) to be hyperbolic (see Appendix A.7). Building on this theory, Maarouf (2008) proposed that the boundary layer separation profile is also hyperbolic. Using these theories, the shock and separation curves are assumed to have hyperbolic profiles that are asymptotic with the freestream Mach angle, θ. The Mach angle is evaluated using Eq. 3.34 at the boundary layer separation position, x_s.

$$\sin\theta = \frac{1}{M_s} \tag{3.34}$$

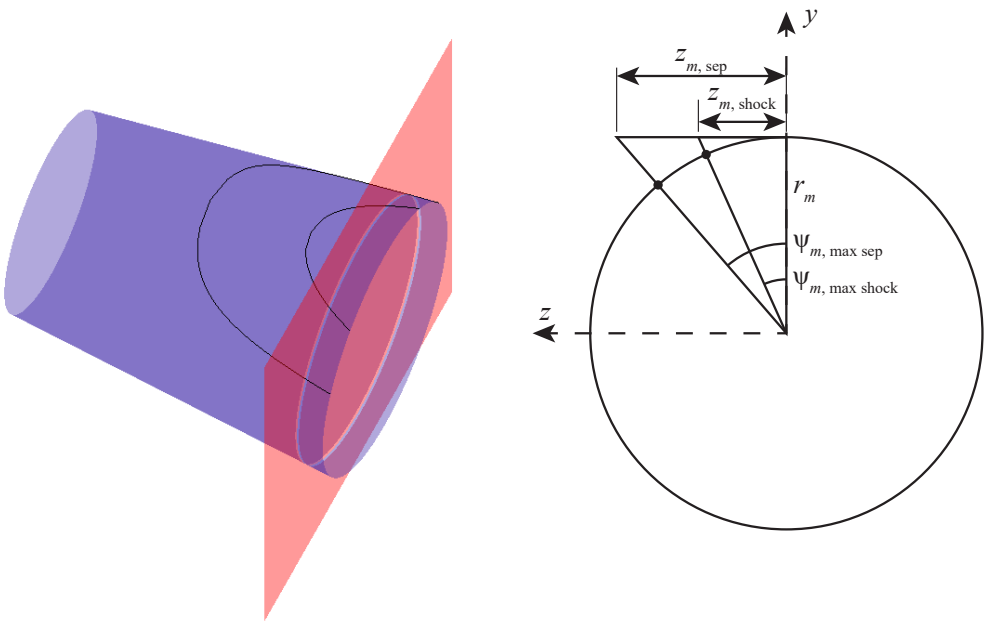

(a) Separation and shock hyperbolas on three-dimensional nozzle surface.

(b) Schematic of $\psi_{m,\,\mathrm{max}}$ for two-dimensional slice of the nozzle at index m.

Figure 3.6: Two- and three-dimensional schematics illustrating $\psi_{m,\mathrm{max}}$ for separation and bow shock hyperbolas at each index m.

A two-dimensional slice is shown in Fig. 3.6b to define ψ_{max} with respect to the z-coordinates of the shock and separation hyperbolas. At each x-position slice (indexed m), ψ_{max} is evaluated using Eq. 3.35.

$$\tan \psi_{m,\mathrm{max}} = \frac{z_m}{r_m} \tag{3.35}$$

Figure 3.7 illustrates the hyperbolic shock and separation profiles ahead of a spherical-nosed body with radius, R. The x-coordinates of the centre of the injection port and focus point of the hyperbolas are x_{inj} and x_F, respectively. The shock standoff distance, Δ, and vertex radius of curvature, R_C are also illustrated.

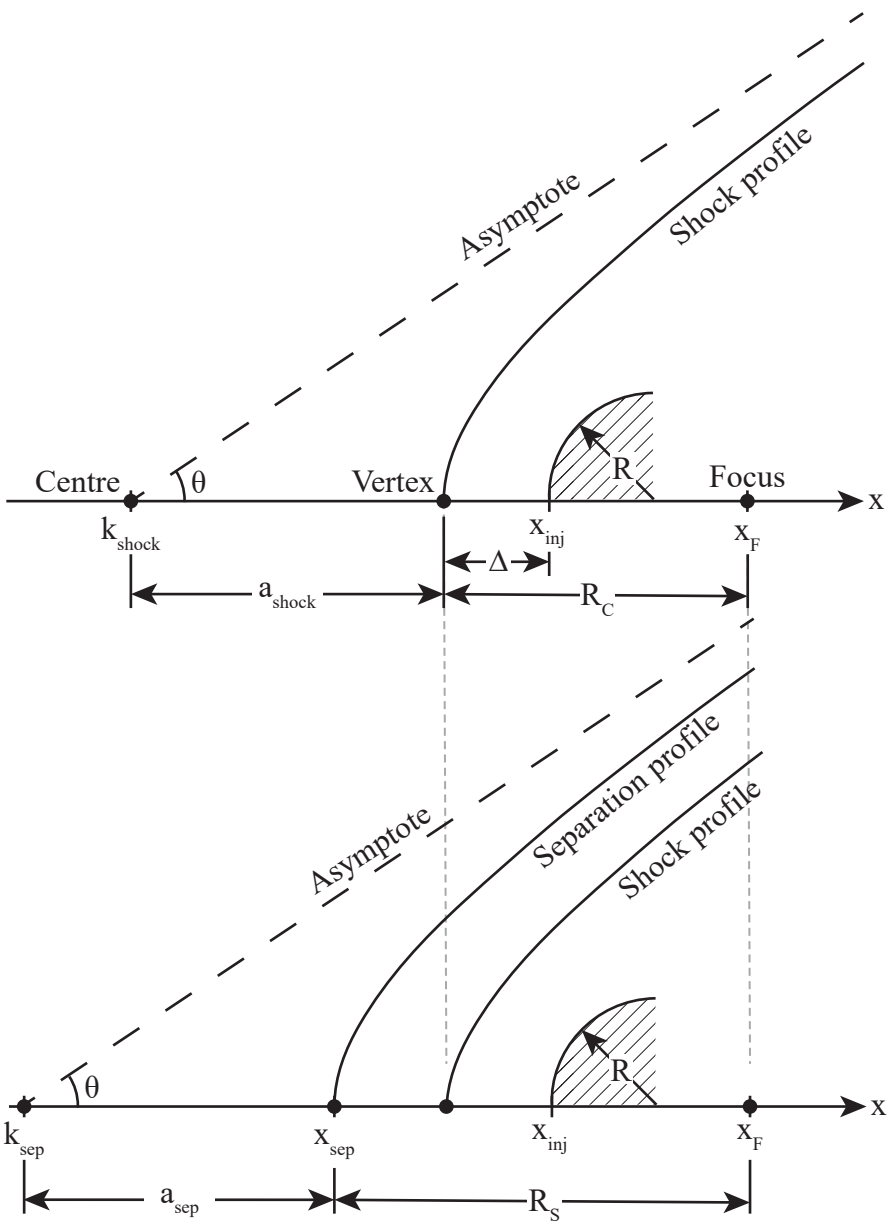

Figure 3.7: Schematics of hyperbolic shock and separation profiles generated by a spherical-nosed body. Adapted from Billig (1967) and Maarouf (2008).

The hyperbola coefficients a, b, and k are defined in Tab. 3.1 using the coordinate system provided in Fig. 3.7.

Table 3.1: Coefficients for hyperbolic shock and separation curves.

Coefficients	a	b	k
Shock profile	$R_C \cot^2\theta$	$R_C \cot^2\theta$	$x_{\text{inj}} - \Delta - R_C \cot^2\theta$
Separation profile	$R_s \cot^2\theta$	$R_s \cot\theta$	$x_F - R_s - \Delta - R_s \cot^2\theta$

Thus, the final shock and separation hyperbolas are presented in Eqs. 3.36 and 3.37, respectively:

$$\left[\frac{x - (x_{\text{inj}} - \Delta - R_C \cot^2\theta)}{R_C \cot^2\theta}\right]^2 - \left[\frac{z_{\text{shock}}}{R_C \cot\theta}\right]^2 = 1 \tag{3.36}$$

$$\left[\frac{x - (x_c - R_s - R_s \cot^2\theta)}{R_s \cot^2\theta}\right]^2 - \left[\frac{z_{\text{sep}}}{R_s \cot\theta}\right]^2 = 1 \tag{3.37}$$

Lastly, the radius of curvature for the separation curve, R_s, may be calculated from the focus point, X_F according to Eqs. 3.38 and 3.39.

$$x_F = x_{\text{inj}} - \Delta + R_C \tag{3.38}$$

$$R_s = x_F - x_s \tag{3.39}$$

The boundary layer separation position, x_s, was determined in subroutine 1.

3.3.3 Determination of the Thrust Vector

The procedure to solve for the thrust vector is schematically shown in Fig. 3.8.

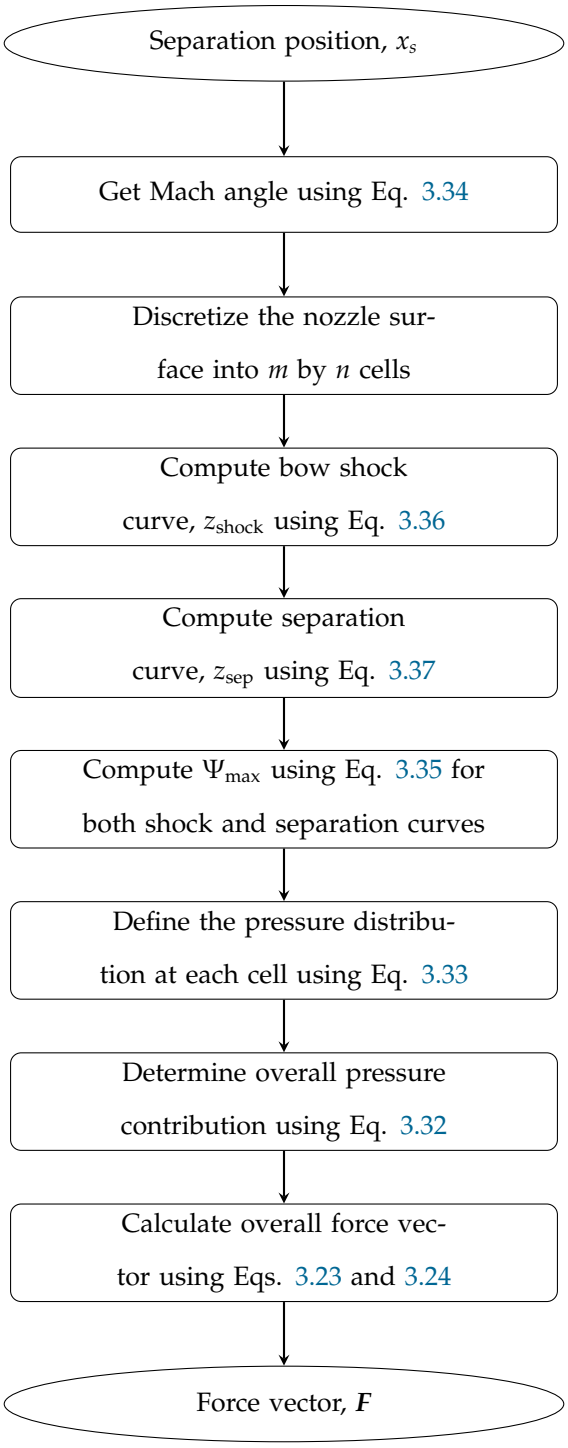

Figure 3.8: Schematic of subroutine 2 for modelling the thrust vector.

3.4 Problem Setup

The geometry and flow properties were selected based on availability of three-dimensional SITVC experimental data in the literature, enabling validation of the model and numerical results. The simulation parameters, including nozzle geometry and flow conditions, were selected based on the experiments performed at the CNRS Institute for Combustion, Aerothermics, Reactivity and Environment (ICARE) (Chpoun et al., 2017; Sellam et al., 2012, 2015; Zmijanovic, 2013; Zmijanovic et al., 2014), herein referred to as the University of Evry experiments. The experimental setup consisted of a blow-down supersonic wind tunnel supplying clean, oil-free, unheated air to both the primary and secondary jets through an SITVC conical nozzle, which exhausted into a vacuum chamber. Experimental setup details are reported by the authors with some discrepancies between the various papers as summarized in Tab. 3.2. Unavailable data is listed as not available (N/A).

Table 3.2: Select reported experimental setup parameters at ICARE.

Study	Half-angle	Area ratio	Nozzle length	T_t	Port diameter
Sellam et al. (2012)	5.42°	$A_e/A_{th} = 4.237$	N/A	N/A	6.15 mm
Zmijanovic et al. (2013)	5.42°	$A_{th}/A_e = 0.236$	N/A	245 K	6 mm
Zmijanovic et al. (2014)	5.42°	$A_e/A_{th} = 4.237$	100 mm	N/A	6 mm
Zmijanovic et al. (2016)	N/A	$A_e/A_{th} = 4.234$	100 mm	260/243 K	6 mm

Given a nozzle length of 100 mm and throat radius of 9.72 mm, an area ratio of 4.237 yields an exit radius of 20.0 mm. Given the same nozzle length and throat radius, a nozzle half-angle of 5.42° yields an exit radius of 19.2 mm. Similar inconsistencies in the stagnation temperature and injection port diameters are shown in Table 3.2. To mitigate these discrepancies, the nozzle geometry and stagnation temperature were matched to the latest paper (Zmijanovic et al., 2016). The experimental data used for comparison with the results in this work is from the earlier three papers, as the latest paper does not report the data required (Zmijanovic et al., 2016). The conical nozzle geometry used in the analytical and numerical assessments in this work are presented in Tab. 3.3. This geometry yields a half-angle and area ratio of approximately 5.87° and 4.234, respectively. Given the potential inconsistencies between the simulation inputs and the experimental setup, errors are expected to arise.

Table 3.3: Conical nozzle geometry.

Dimension	Value (mm)
Throat radius	9.72
Exit radius	20.0
Nozzle length	100.0
Injector port position	90.0

The centre of the injection port is located at 90% of the nozzle length ($x_{\text{inj}} = 90.0$ mm). Note that the origin of the x-coordinate is set at the nozzle throat. The injection is perpendicular to the primary rocket axis, not the conical nozzle wall. The experimental setup's nozzle geometry was initially unclear, leading to a 6 mm injector port diameter assumption in the numerical simulations. However, it was later confirmed that the experiments used a 6.15 mm port diameter, which has been updated in the model results. Consequently, this discrepancy in port diameter should be noted when interpreting quantitative comparisons between the numerical and experimental results, as the smaller port size in simulations results in a secondary injection mass flow rate that is 4.8% lower than expected for the experiment. Primary and secondary flow parameters are provided in Tab. 3.4.

Table 3.4: Primary and secondary flow parameters.

Parameter	Species	Molar mass	Stagnation pressure	Stagnation temperature	Inlet Mach
Primary flow	Air	28.96 kg/kmol	300 kPa	260 K	1
Secondary flow			Varies		

The secondary jet stagnation pressure is varied to evaluate its effect on TVC performance. The secondary pressure ratio (SPR) is defined in Eq. 3.40 as the stagnation pressure ratio of the secondary to the primary jets. Analytical and numerical simulations are performed at SPR values of 0.667, 0.833, 1, and 1.167.

$$\text{SPR} = \frac{P_{tj}}{P_t} \tag{3.40}$$

The SITVC nozzle exhausts into a vacuum chamber with air at an ambient temperature and pressure of

290 K and 8 kPa, respectively.

Table 3.5: Ambient conditions of the air surrounding the SITVC exhaust nozzle.

Parameter	Pressure	Temperature
Value	8 kPa	290 K

Chapter 4

Numerical Simulation of SITVC

Numerical investigation of the secondary injection of a gas into supersonic flow of the diverging nozzle is performed using OpenFOAM, an open source CFD software (Weller et al., 1998), coupled with the third-party solver pimpleCentralFOAM (Kraposhin et al., 2015, 2018). The CFD simulation parameters, including nozzle geometry and flow conditions, were selected based on the experiments performed at the ICARE research institute as discussed in Section 3.4. The experimental setup consisted of a blow-down supersonic wind tunnel supplying clean, oil-free, unheated air to both the primary and secondary jets through an SITVC conical nozzle, which exhausted into a vacuum chamber. This chapter outlines the complete methodology for the numerical simulations of this experiment. It begins with a discussion of the governing equations, thermophysical modelling, and turbulence modelling. Numerical discretization methods are then covered, followed by details on mesh generation and boundary conditions. Finally, an uncertainty assessment of the results is presented. A survey of numerical simulations of SITVC in the literature is summarized in Appendix D.

4.1 Governing Equations

SITVC involves (1) high-speed compressible flow with discontinuities, (2) turbulent mixing, and (3) jet expansion (Walker et al., 1962). The selected solver, pimpleCentralFOAM, captures these flow features by employing a hybrid scheme of the PISO (Pressure-Implicit with Splitting of Operators) and SIMPLE (Semi-Implicit Method for Pressure Linked Equations) algorithms (Kraposhin et al., 2018). In addition, it uses a non-oscillating central discretization scheme for the convective terms (similar to rhoCentralFOAM) at higher Mach numbers. The conservative mass, momentum and energy conservation equations (shown

in Eqs. 4.1 to 4.3) are solved implicitly:

$$\underbrace{\frac{\partial \rho}{\partial t}}_{\text{Transient term}} + \underbrace{\boldsymbol{\nabla} \cdot (\rho \boldsymbol{U})}_{\text{Convective term}} = 0 \tag{4.1}$$

$$\underbrace{\frac{\partial \rho \boldsymbol{U}}{\partial t}}_{\text{Transient term}} + \underbrace{\boldsymbol{\nabla} \cdot [\boldsymbol{U} (\rho \boldsymbol{U})]}_{\text{Convective term}} + \underbrace{\boldsymbol{\nabla} P}_{\text{Pressure gradient}} - \underbrace{\boldsymbol{\nabla} \cdot \boldsymbol{\tau}}_{\text{Viscous diffusion term}} = 0 \tag{4.2}$$

$$\underbrace{\frac{\partial \rho E}{\partial t}}_{\text{Transient term}} + \underbrace{\boldsymbol{\nabla} \cdot [\boldsymbol{U} (\rho E)]}_{\text{Convective term}} + \underbrace{\boldsymbol{\nabla} \cdot (P \boldsymbol{U})}_{\text{Pressure work term}} - \underbrace{\boldsymbol{\nabla} \cdot (\boldsymbol{\tau} \cdot \boldsymbol{U})}_{\text{Viscous dissipation term}} + \underbrace{\boldsymbol{\nabla} \cdot \boldsymbol{q}}_{\text{Thermal diffusion term}} = 0 \tag{4.3}$$

where ρ, t, $\boldsymbol{U}$, P, $\boldsymbol{\tau}$, E and $\boldsymbol{q}$ are the density, time, velocity vector, pressure, viscous stress tensor, total energy and diffusive heat flux, respectively. Detailed derivation and explanation of the governing equations (Eqs. 4.1 to 4.5) are available in Moukalled et al. (2015). The viscous stress tensor for a Newtonian fluid is given by Eq. 4.4:

$$\boldsymbol{\tau} = \mu \left[\boldsymbol{\nabla} \boldsymbol{U} + (\boldsymbol{\nabla} \boldsymbol{U})^T \right] - \frac{2}{3} \mu (\boldsymbol{\nabla} \cdot \boldsymbol{U}) \boldsymbol{I} \tag{4.4}$$

where μ and $\boldsymbol{I}$ are the dynamic viscosity and identity matrix, respectively. The diffusive heat flux is governed by Fourier's law of conduction shown in Eq. 4.5:

$$\boldsymbol{q} = -\kappa \boldsymbol{\nabla} T \tag{4.5}$$

where κ and T are the thermal conductivity and temperature, respectively.

Note that the rhoCentralFOAM (rCF) solver is often selected for high-speed compressible flow problems in OpenFOAM because of its ability to capture flow discontinuities like shock waves (Bondarev and Kuvshinnikov, 2018). However, rCF is an explicit solver, which requires small time steps. Conversely, the pimpleCentralFOAM solver is implicit, offering greater numerical stability and allowing for larger time steps (Moukalled et al., 2015). In addition to the capabilities of pimpleCentralFOAM, reactingPimpleCentralFOAM can handle multi-species problems. This will allow the investigation of multi-species secondary injection in future work with minor modification of the current simulation setup.

4.2 Thermophysical Modelling

The working fluid, air, was modelled using the perfect gas equation of state:

$$P = \rho R T \tag{4.6}$$

where R is the gas constant. Generally, this simplified relation is only valid for gases at high temperatures and low pressures. To quantify the deviation from real gas behaviour, the fluid densities at each temperature and pressure were determined using CoolProp (Bell et al., 2014). CoolProp is a C++ library that calculates thermophysical properties using the Helmholtz-energy-explicit formulations (Lemmon et al., 2000; Lemmon and Jacobsen, 2004). The maximum and average deviations of the compressibility factor from 1.0 were 0.3% and 0.02%, respectively. Thus, the working fluid behaves ideally within the simulation range of 40 K $< T <$ 290 K. This low temperature bound reflects the conditions arising from the unheated air supplied by the wind tunnel. Note that the lowest temperatures are only observed in a very small and localized region downstream of the injection.

In addition, the viscosity requires modelling, as it varies by over 700% in this temperature range. The dynamic viscosity (μ) was calculated using Sutherland's law presented in Eq. 4.7:

$$\mu = \frac{A_s \sqrt{T}}{1 + T_s/T} \tag{4.7}$$

where for air, $A_s = 1.46E - 6$ kg/ms $\sqrt{\text{K}}$ and $T_s = 111$ K. This relation is valid from 0 K to 3000 K (Rathakrishnan, 2013).

The modified Eucken method was implemented for modelling thermal conductivity (κ):

$$\kappa = \mu C_V \left(1.32 + \frac{1.77R}{C_V}\right) \tag{4.8}$$

where C_V is the heat capacity at constant volume.

No references were found for specific heat capacity models valid at the low temperature bound of 40 K. Instead, initial CFD simulations were conducted and their results were used to obtain average conditions inside the nozzle. A heat capacity at constant pressure (C_P) of 1014 J/kg K was set based on the average temperature inside the nozzle.

4.3 Turbulence Modelling

Turbulence modelling is required for resolving the Reynolds stress term in the governing equations. The selected turbulence model must accurately resolve the SITVC features of interest, which include the pressure profile along the nozzle wall, boundary layer separation and overall thrust vector. Accurate near wall treatment is required in the presence of an adverse pressure gradient. The k-ω shear stress transport (SST) turbulent model was selected for its accurate predictions in both near-wall and far-wall regions, as well as its ability to handle adverse pressure gradients and boundary layer separation in similar flows (Hou et al., 2011; Li and Wu, 2021; Sethuraman et al., 2021).

The k-ω SST turbulence model is a two-equation eddy viscosity model that combines the k-ϵ and k-ω models using a blending function (Menter et al., 2003). The k-ϵ model solves two transport equations for the turbulent kinetic energy (k) and the turbulent dissipation rate (ϵ). However, as the distance from the wall decreases, the dissipation rate grows exponentially, leading to inadequate modelling of near-wall phenomena such as boundary layer separation. To overcome this, the k-ω turbulence model was developed which implements a transport equation for the turbulent dissipation frequency (ω) and k. Note that the dissipation rate and frequency are related according to Eq. 4.9.

$$\omega = \frac{\epsilon}{k\beta^*} \tag{4.9}$$

Here, β^* is a standard coefficient of the model and is defined in Tab. 4.1. While the k-ω model showed great improvement near the wall, the freestream flow was found to be sensitive to the boundary conditions imposed on ω at the inputs . The k-ω SST model addresses these shortcomings by combining the near wall treatment of the k-ω model with freestream performance of the k-ϵ model using a blending function, F_1. To do this, $\omega = \epsilon/k\beta^*$ is substituted into the ϵ transport equation causing an additional cross-diffusion term to emerge when compared to the original transport equation for ω. The weight of this additional term is adjusted based on the distance from the wall using the blending function. Thus, the k-ω SST model combines accurate near-wall modelling with insensitivity to boundary conditions, making it an appropriate turbulence model for the prediction of flow separation in the presence of an adverse pressure gradient.

The conservative transport equations for the TKE and dissipation frequency are presented in Eqs. 4.10 and 4.11.

$$\underbrace{\frac{\partial(\rho k)}{\partial t}}_{\text{Transient term}} + \underbrace{\nabla\cdot(\rho k\boldsymbol{U})}_{\text{Convective term}} = \underbrace{\widetilde{P_k}}_{\text{Production term}} - \underbrace{\rho\epsilon}_{\text{Dissipation term}} + \underbrace{\nabla\cdot[(\mu+\sigma_k\mu_t)\nabla k]}_{\text{Diffusion term}} \tag{4.10}$$

$$\underbrace{\frac{\partial(\rho\omega)}{\partial t}}_{\text{Transient term}} + \underbrace{\nabla\cdot(\rho\omega\boldsymbol{U})}_{\text{Convective term}} = \underbrace{\frac{\gamma_t}{\nu_t}\widetilde{P_k}}_{\text{Production term}} - \underbrace{\beta\rho\omega^2}_{\text{Dissipation term}} + \underbrace{\nabla\cdot\left[\left(\mu+\sigma_\omega\mu_t\right)\nabla\omega\right]}_{\text{Diffusion term}} + \underbrace{2\left(1-F_1\right)\frac{\rho\sigma_{\omega 2}}{\omega}\nabla k:\nabla\omega}_{\text{Cross-Diffusion term}} \tag{4.11}$$

The final term in Eq. 4.11 is responsible for smoothly transitioning between the k-ω model near the wall and the k-ϵ model away from the wall according to Eqs. 4.12 and 4.13:

$$F_1 = \tanh\left(\left[\min\left(\max\left[\frac{\sqrt{k}}{\beta^*\omega d}, \frac{500\nu}{d^2\omega}\right], \frac{4\rho\sigma_{\omega 2}k}{CD_{k\omega}d^2}\right)\right]^4\right) \tag{4.12}$$

$$CD_{k\omega} = \max\left(2\rho\sigma_{\omega 2}\frac{1}{\omega}\nabla k:\nabla\omega, 10^{-10}\right) \tag{4.13}$$

where d is the distance to the nearest wall. The coefficients are combined using the blending function F_1 according to Eq. 4.14.

$$\phi = \phi_1 F_1 + \phi_2\left(1-F_1\right) \tag{4.14}$$

OpenFOAM's default k-ω SST model coefficients were used and are provided in Tab. 4.1.

Table 4.1: $k-\omega$ SST coefficients.

Parameter	σ_k	σ_ω	β	γ_t	a_1	β^*
ϕ_1 (k-ω)	0.85	0.5	0.075	0.555	0.31	0.09
ϕ_2 (k-ϵ)	1	0.856	0.0828	0.44		

The implemented k-ω SST model limits the production term to prevent the non-physical accumulation of turbulence in stagnation regions. The original and limited TKE production terms are shown in Eqs. 4.15 and 4.16, respectively.

$$P_k = \boldsymbol{\tau}:\nabla\boldsymbol{U} \tag{4.15}$$

$$\widetilde{P_k} = \min\left(P_k, 10\beta^*\rho\omega k\right) \tag{4.16}$$

The shear stress is evaluated according to Eq. 4.17.

$$\boldsymbol{\tau} = \mu_t\left(2\boldsymbol{S} - \frac{2}{3}\left(\nabla\cdot\boldsymbol{U}\right)\boldsymbol{I}\right) - \frac{2}{3}\rho k\boldsymbol{I} \tag{4.17}$$

The mean rate of strain tensor is defined according to Eq. 4.18.

$$\boldsymbol{S} = \frac{1}{2}\left[\nabla\boldsymbol{U} + \left(\nabla\boldsymbol{U}\right)^T\right] \tag{4.18}$$

Lastly, the k-ω SST model implements a viscosity limiter using the strain invariant (Eqs. 4.19 to 4.20). This limiter imposes an upper bound on the viscosity and results in better agreement with separated flow experimental data.

$$\mu_t = \frac{\rho a_1 k}{\max(a_1\omega, SF_2)} \tag{4.19}$$

$$S = \sqrt{2\boldsymbol{S} : \boldsymbol{S}} \tag{4.20}$$

The second blending function, F_2, is presented in Eq. 4.21.

$$F_2 = \tanh\left(\left[\max\left(2\frac{\sqrt{k}}{\beta^*\omega d}, \frac{500\nu}{d^2\omega}\right)\right]^2\right) \tag{4.21}$$

4.4 Numerical Discretization

Up to this point, the SITVC problem has been translated from the physical world into mathematical terms using partial differential equations (PDEs), constitutive equations, and fluid modelling to close out the problem. However, since an analytical solution to these PDEs does not exist, a numerical approach is necessary. Implementation of the numerical solution requires extraction of key cell geometry terminology from the finite volume mesh first. Figure 4.1 schematically illustrates the owner cell C sharing an interface with its neighbouring cell N. The two cell centres are connected using vector $\boldsymbol{d}$. The face area vector $\boldsymbol{S}_f$ is a product of the face area and the unit outward normal vector. Finally, the vector connecting the face centre $\boldsymbol{C}_f$ to the neighbouring cell centre is denoted by $\boldsymbol{d}_{fN}$.

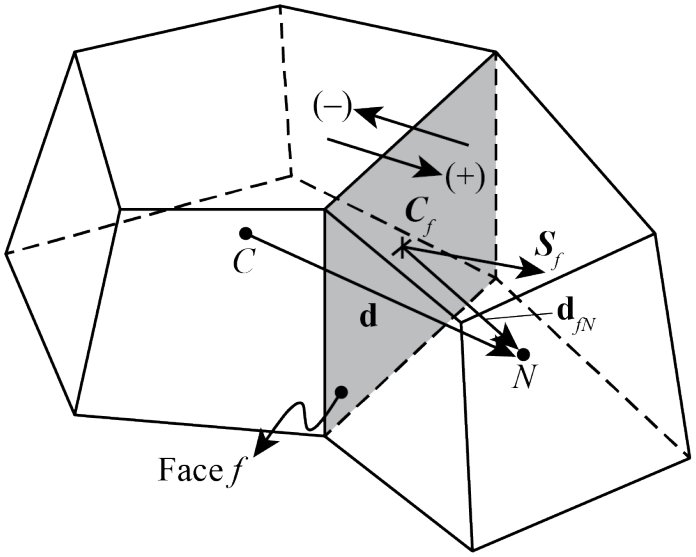

Figure 4.1: Schematic of finite volume cell for computation of fluxes. Adapted from Greenshields et al. (2009).

The following sections detail the numerical discretization schemes applied to each term in the governing equations. An arbitrary flow parameter, $\boldsymbol{\psi}$, is used to represent the flow variables for brevity.

4.4.1 Temporal Discretization

The transient term ($\partial\boldsymbol{\psi}/\partial t$) governs the time evolution of the simulation. In steady-state problems, the temporal derivative is set to zero, while in transient simulations, an appropriate discretization scheme must be selected. In this work, the transient term is discretized using the first-order backward Euler method shown in Eq. 4.22. While second-order schemes are generally preferred for their improved accuracy in capturing transient behaviour, first-order schemes were employed in this work. This choice is justified because the focus was solely on achieving the steady-state solution. The transient terms diminish as the solution approaches steady state, rendering the potential benefits of second-order schemes negligible.

$$\frac{\partial\boldsymbol{\psi}}{\partial t} = \frac{\boldsymbol{\psi}^{n} - \boldsymbol{\psi}^{n-1}}{\Delta t} \tag{4.22}$$

Here, $\boldsymbol{\psi}^{n}$ represents the solution at current time step and $\boldsymbol{\psi}^{n-1}$ represents the solution at the previous time step. While this implicit approach provides the advantage of larger increments in time, it has a high computational cost per time step when compared to explicit methods (Moukalled et al., 2015).

The Courant-Friedrichs-Lewy (CFL) condition imposes time step requirements for CFD simulations for the performance of numerical schemes. The Courant number (Co) is a non-dimensional parameter defined as follows for a one-dimensional problem.

$$Co = \frac{u\Delta t}{\Delta x} \tag{4.23}$$

When $Co = 1$, a fluid particle travelling at velocity u passes through a cell of length Δx in one time step Δt. For three-dimensional problems, the CFL number is calculated as follows:

$$Co = \frac{\Delta t}{2V}\sum_{f}|\phi_f| \tag{4.24}$$

where, $|\phi_f|$ represents the volumetric flux through a cell face, f. In this work, the local time step was selected to maintain a maximum Courant number of 0.3 according to Kraposhin et al. (2018).

4.4.2 Advective Discretization

Next, discretization of the convective terms is discussed. The convected flow parameters are ρ, $\rho\boldsymbol{U}$, and ρE in the mass, momentum, and energy conservation equations, respectively. In the following section, the

arbitrary flow parameter, $\boldsymbol{\psi}$, represents these convected flow variables. Eq. 4.25 relates the differential and integral forms of the convection term. Then, the integral form is discretized using a summation over the cell faces $\sum_f$:

$$\nabla \cdot (\boldsymbol{U}\boldsymbol{\psi}) = \lim_{\Delta V \to 0} \frac{1}{\Delta V} \int_S (d\boldsymbol{S} \cdot \boldsymbol{U}\boldsymbol{\psi}) \approx \frac{1}{V} \sum_f \boldsymbol{S}_f \cdot \boldsymbol{U}_f \boldsymbol{\psi}_f = \frac{1}{V} \sum_f \phi_f \boldsymbol{\psi}_f \tag{4.25}$$

where ΔV and $\boldsymbol{S}_f$ represent the cell volume and face area normal vector, respectively. Note that $\phi_f = \boldsymbol{S}_f \cdot \boldsymbol{U}_f$ is the volumetric flow rate through a cell face. The finite volume method solves flow parameters at the cell centres. As such, interpolation from cell centres to faces is required for the evaluation of the convective terms. The pimpleCentralFOAM solver uses a switching function (Eq. 4.26) based on the Mach number and CFL at the face to combine the PISO/SIMPLE and Kurganov and Tadmore (KT)/Kurganov, Noelle and Petrova (KNP) algorithms. As compressibility effects increase, κ_f approaches 1, and fluxes are calculated according to the KT/KNP schemes. On the other hand, at low Mach numbers, the incompressible approach is implemented and κ_f approaches zero.

$$\kappa_f = \min\left(\frac{M_f}{\mathrm{CFL}}, 1\right) \tag{4.26}$$

For incompressible flows, the PISO/SIMPLE algorithm linearly interpolates the velocity, $\boldsymbol{U}_f$, using a central differencing scheme. Interpolation of the convected variable $\boldsymbol{\psi}_f$ requires the consideration of upwinding effects.

As compressibility effects become more significant, the fluxes include both the velocity of the fluid, as well as the acoustic speed of the propagation of disturbances (Kraposhin et al., 2015). The KT/KNP schemes consider this by using weighted fluxes from the + and - directions to evaluate the discretized convection term as in Eq. 4.27.

$$\frac{1}{V} \sum_f \phi_f \boldsymbol{\psi}_f = \frac{1}{V} \sum_f \left[\alpha \phi_{(f+)} \psi_{(f+)} + (1-\alpha)\phi_{(f-)}\psi_{(f-)} + \omega_f \left(\psi_{(f+)} - \psi_{(f-)}\right)\right] \tag{4.27}$$

The two weighting functions, α and ξ_f, are evaluated according to Eq. 4.28 and 4.29, respectively:

$$\alpha = \frac{a_{(f+)}}{a_{(f+)} + a_{(f-)}} \tag{4.28}$$

$$\xi_f = \alpha\,(1-\alpha)\left(a_{(f+)} + a_{(f-)}\right) \tag{4.29}$$

The volumetric fluxes that account for both the flow speed and wave propagation speed are evaluated

according to Eq. 4.30:

$$\begin{aligned} a_{(f+)} &= \max\left(c_{(f+)}|\boldsymbol{S}_f| + \phi_{(f+)} \quad , \quad c_{(f-)}|\boldsymbol{S}_f| + \phi_{(f-)} \quad , \quad 0\right) \\ a_{(f-)} &= -\min\left(-c_{(f+)}|\boldsymbol{S}_f| + \phi_{(f+)} \quad , \quad -c_{(f-)}|\boldsymbol{S}_f| + \phi_{(f-)} \quad , \quad 0\right) \end{aligned} \tag{4.30}$$

where the wave propagation speed is calculated using Eq. 4.31.

$$c_{(f\pm)} = \sqrt{\gamma_{(f\pm)} R T_{(f\pm)}} \tag{4.31}$$

Finally, the mass fluxes are evaluated according to Eq. 4.32.

$$\begin{aligned} \Phi_{(f-)} &= \kappa_f \alpha \rho_{(f+)} \left(\phi_{(f+)} + a_{(f+)}\right) \\ \Phi_{(f+)} &= \left(1 - \kappa_f\right) \alpha \rho_{(f+)} \left(\phi_{(f+)} + a_{(f+)}\right) + \rho_{(f-)} \left((1-\alpha)\,\phi_{(f-)} - \alpha a_{(f-)}\right) \end{aligned} \tag{4.32}$$

Treatment of $\boldsymbol{\psi}_f$ is critical because convection is an inherently directional phenomenon. The convected property $\boldsymbol{\psi}$ is carried in the direction of the flow velocity $\boldsymbol{U}$. Interpolation of $\boldsymbol{\psi}_f$ from the cell centres to faces must account for this directional behaviour. However, the linear interpolation scheme discussed in Section 4.4.5 is a central differencing scheme. This means it does not place higher weighting on the upstream cell, which tends to produce unbounded solutions (Greenshields and Weller, 2022). To resolve this, the upwind scheme was developed, where the face value is directly taken from the upstream cell. While the solution is stable, the upwind scheme has a highly diffusive nature leading to poor solution accuracy (Moukalled et al., 2015). To overcome the issues with boundedness and accuracy, blending of the linear and upwind schemes is implemented using a limiter β_{lim} according to Eqs. 4.33 and 4.34. These schemes define the limiter β_{lim} as a function of the gradient ratio r_{grad}.

$$\boldsymbol{\psi}_{f+} = \left(1 - \beta_{\text{lim}}(r_{\text{grad}})\left(1 - \xi_f\right)\right)\boldsymbol{\psi}_C + \beta_{\text{lim}}(r_{\text{grad}})\left(1 - \xi_f\right)\boldsymbol{\psi}_N \tag{4.33}$$

$$r_{\text{grad}} = \max\left[2\frac{\boldsymbol{\Delta d} \cdot \boldsymbol{\nabla \psi}}{|\boldsymbol{\Delta d}| \nabla_n \boldsymbol{\psi}_f} - 1, 0\right] \tag{4.34}$$

In this work, the van Albada scheme is used to compute fluxes across cell faces according to Eq. 4.35. This scheme blends between linear ($\beta_{\text{lim}} = 1$) and upwind ($\beta_{\text{lim}} = 0$) schemes. This second-order method provides a balance between accuracy and stability, particularly in the presence of strong gradients or shocks.

$$\beta_{\text{lim}} = \frac{r_{\text{grad}}^2 + r_{\text{grad}}}{r_{\text{grad}}^2 + 1} \tag{4.35}$$

4.4.3 Gradient Discretization

Next, discretion of the gradient term is evaluated. The gradient of an arbitrary flow variable, ψ, is defined according to Eq. 4.36.

$$\nabla\psi = \frac{\partial\psi}{\partial x}e_1 + \frac{\partial\psi}{\partial y}e_2 + \frac{\partial\psi}{\partial z}e_3 \tag{4.36}$$

The pressure gradient is required for momentum conservation (Eq. 4.2), and the velocity gradient is needed for the production term in the TKE transport equation (Eq. 4.10). Following the approach implemented for convection discretization, the gradient term at the cell centres is evaluated using the flow parameters at the cell faces. This approach, which is known as the Green-Gauss gradient method, is presented in Eq. 4.37. Here, the face area vector S_f is known from the mesh geometry, and the flow parameter, ψ_f is interpolated from the cell centre to the face. The linear scheme, which is discussed in Section 4.4.5, is used for the latter.

$$\nabla\psi = \lim_{\Delta V\to 0}\frac{1}{\Delta V}\int_S (d\boldsymbol{S}\psi) \approx \frac{1}{V}\sum_f \boldsymbol{S}_f\psi_f \tag{4.37}$$

In addition, the point linear scheme, which uses interpolated values from the cell vertices, may be implemented for high-skewness meshes. Another approach for numerically evaluating the gradient at the cell centre is the least squares finite difference method. An optimization process minimizes the function G_C, in Eq. 4.38.

$$G_C = \sum_f \left(w_{id}^2\left[\psi_{Nf} - \psi_C + \nabla\psi\cdot\boldsymbol{d}\right]^2\right) \tag{4.38}$$

The gradient is then evaluated using Eq. 4.39:

$$\nabla\psi \approx \frac{1}{V}\sum_f w_{id}^2\boldsymbol{G}^{-1}\cdot\boldsymbol{d}\left(\psi_N - \psi_C\right) \tag{4.39}$$

where the tensor $\boldsymbol{G}$ is calculated in Eq. 4.40:

$$\boldsymbol{G} = \sum_f w_{id}^2\boldsymbol{d}\boldsymbol{d} \tag{4.40}$$

In this case, the weighting function is given by $w_{id} = 1/|\boldsymbol{d}|$. The least squares gradient method yields higher accuracy at the cost of higher computation requirements when compared to the Green-Gauss method (Greenshields and Weller, 2022).

Gradient limiters implements a limit on the gradient value such that extrapolated values of ϕ_f are within the bounds of all neighbouring cells. Simulations in this work used a cell-limited least-squares gradient discretization approach to achieve improved accuracy.

4.4.4 Laplacian Discretization

Finally, the discretization of the Laplacian terms is discussed. To determine the diffusive terms at the cell centres, the divergence theorem is applied then discretized using a summation over the cell faces in Eq. 4.41,

$$\nabla \cdot (\Gamma \nabla \psi) = \lim_{\Delta V \to 0} \frac{1}{\Delta V} \int_S \left(dS_f \Gamma \nabla_n \psi \right) \approx \frac{1}{V} \sum_f |S_f| \Gamma_f \nabla_n \psi_f \tag{4.41}$$

where $|S_f|$ is known from the mesh data. The diffusivity at the face, Γ_f, is determined using linear interpolation from cell centres. The surface normal gradient, $\nabla_n \psi_f$, which corresponds to the gradient of ψ in the direction of the surface normal, requires further investigation:

$$\nabla_n \psi_f = C_\Delta (\psi_N - \psi_C) \tag{4.42}$$

where $C_\Delta = 1/|d|$. However, Eq. 4.42 is only valid for orthogonal meshes. Meshes with non-orthogonality are characterized by misalignment between the face normal unit vector n and the vector connecting the two cell centres (d). These meshes require a non-orthogonal correction in addition to the orthogonal contribution according to Eq. 4.43:

$$\nabla_n \psi_f = \underbrace{C_\Delta^{corr} (\psi_N - \psi_C)}_{\text{orthogonal}} + \underbrace{\left(n - C_\Delta^{corr} d \right) \cdot (\nabla \psi)_f}_{\text{non-orthogonal}} \tag{4.43}$$

where $C_\Delta^{corr} = 1/(n \cdot d)$.

For poor quality meshes with non-orthogonality over 75 degrees, Eq. 4.43 produces numerical instability (Greenshields and Weller, 2022). To resolve this, limiters may be applied to impose bounds on the Laplacian terms. In this work, Laplacian limiters were not necessary, as mesh non-orthogonality always fell below 75 degrees.

4.4.5 Numerical Interpolation

Linear interpolation is used to obtain face values from neighbouring cell values according to Eq. 4.44:

$$\psi = w_f \psi_P + (1 - w_f) \psi_N \tag{4.44}$$

where the weighting factor, w_f is calculated according to Eq. 4.45:

$$w_f = \frac{|S_f \cdot d_{fN}|}{|S_f \cdot d|} \tag{4.45}$$

This central differencing scheme is second-order accurate.

4.5 Linear Solvers

So far, the partial differential equations have been reconstructed into massive systems of linear equations, but solving them efficiently remains nontrivial. Traditional methods such as Gaussian elimination are computationally expensive and time consuming (Greenshields and Weller, 2022). Instead, the introduction of iterative methods greatly speeds up computation time while generating accurate solutions. For the pressure equation, the generalized geometric-algebraic multigrid (GAMG) solver first approximates the solution using a coarse grid (Stuben, 2001). This initial solution is mapped to the actual (fine) grid and iterated until convergence is achieved. The preconditioned bi-conjugate gradient stabilized (PBiCGStab) method was used for solving the remaining variables. The diagonal incomplete lower-upper (DILU) preconditioner was used to estimate the matrix inverse using only its diagonal elements, reducing computational time and accelerating convergence. Barrett et al. (1994) details the implementation of the PBiCGStab solver with preconditioning. For both iterative solvers, tolerances of 10^{-10} or below were selected to minimize the residuals such that sufficient solution accuracy was achieved (Greenshields and Weller, 2022).

4.6 Mesh Generation and Boundary Conditions

The diverging nozzle geometry, originating from extensive studies performed at the Orléans ICARE research centre (Sellam et al., 2012; Zmijanovic et al., 2013; Zmijanovic, 2013), is a Mach 3 axisymmetric conical design as shown in Fig. 4.2. Note that secondary injection is perpendicular to the nozzle axis, rather than the nozzle wall.

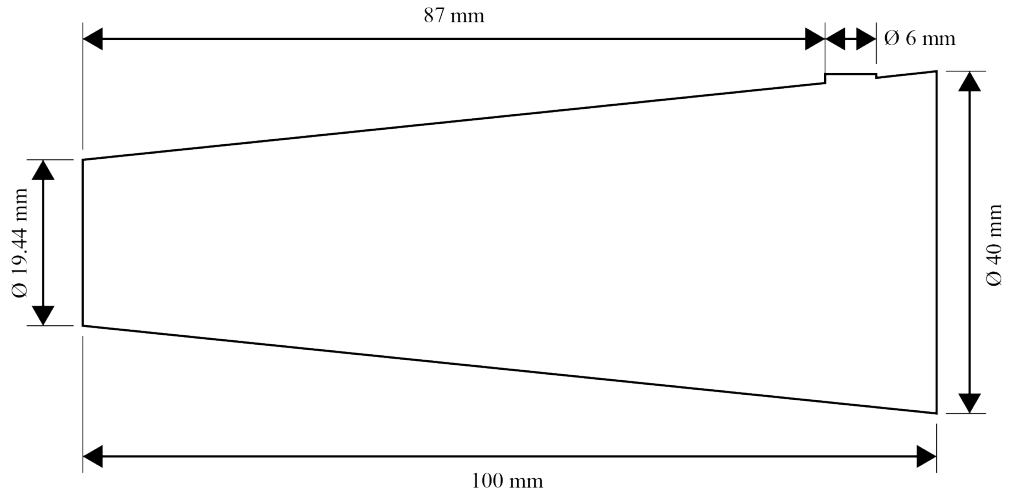

Figure 4.2: Conical nozzle geometry. Adapted from Sellam et al. (2012).

A schematic of the computational domain and associated boundary patches is shown in Fig. 4.3. Table 4.2 summarizes the boundary conditions for each patch. The primary and secondary sonic inlets were defined using stagnation properties for temperature and pressure, and a fixed value for velocity according to Moukalled et al. (2015) and Greenshields and Weller (2022). The no-slip, adiabatic wall condition was applied for the nozzle wall, while the slip, adiabatic condition was applied for the secondary injection pipe wall and the interface between the nozzle and farfield. The exterior domain, labelled as the farfield, was set to an inlet-outlet boundary condition to account for possible vortices exiting the domain. Since only half the conical nozzle was simulated, a symmetric boundary condition was implemented for the symmetry plane.

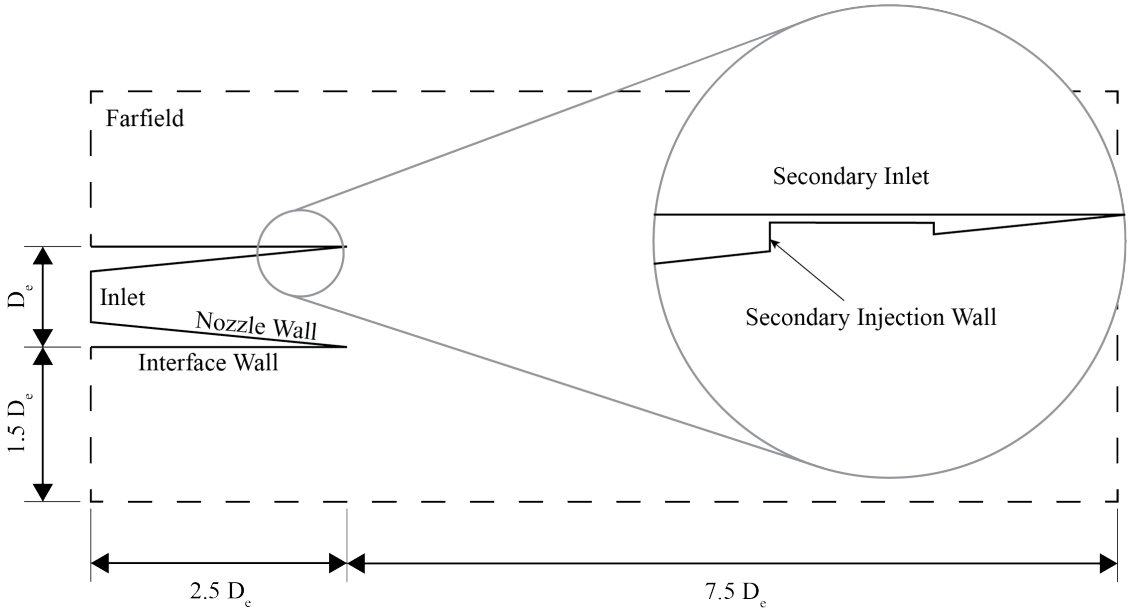

Figure 4.3: Schematic of boundary conditions and domain.

Table 4.2: SITVC nozzle simulation boundary conditions.

Patch	Temperature	Velocity	Pressure	k	ω	ν_t	α_t
Inlet	Total temperature 260K	Fixed value (296, 0, 0)	Total pressure 300kPa	Turbulent intensity kinetic energy inlet 0.1%	Turbulent mixing length frequency inlet 0.001361 m	Calculated	Calculated
Secondary inlet	Total temperature 260K	Fixed value (0, -296, 0)	Total pressure 300kPa	Turbulent intensity kinetic energy inlet 5%	Turbulent mixing length frequency inlet 0.00042 m	Calculated	Calculated
Nozzle wall	Zero gradient	No slip	Zero gradient	k Low Re wall function	ω wall function	Low Re wall function	Wall function
Interface wall	Zero gradient	Slip	Zero gradient	k Low Re wall function	ω wall function	Low Re wall function	Wall function
Secondary injection wall	Zero gradient	Slip	Zero gradient	k Low Re wall function	ω wall function	Low Re wall function	Wall function
Farfield	Inlet outlet 290K	Zero gradient	Fixed value 8 kPa	Zero gradient	Zero gradient	Calculated	Calculated
Symmetry	Symmetry	Symmetry	Symmetry	Symmetry	Symmetry	Symmetry	Symmetry

Farfield domain sizing was chosen to minimize boundary condition effects and to sufficiently capture flow development outside the nozzle (including an over- or under-expanded nozzle regime), while minimizing computational speed and resource requirements. The complete computational mesh is shown in Fig. 4.4.

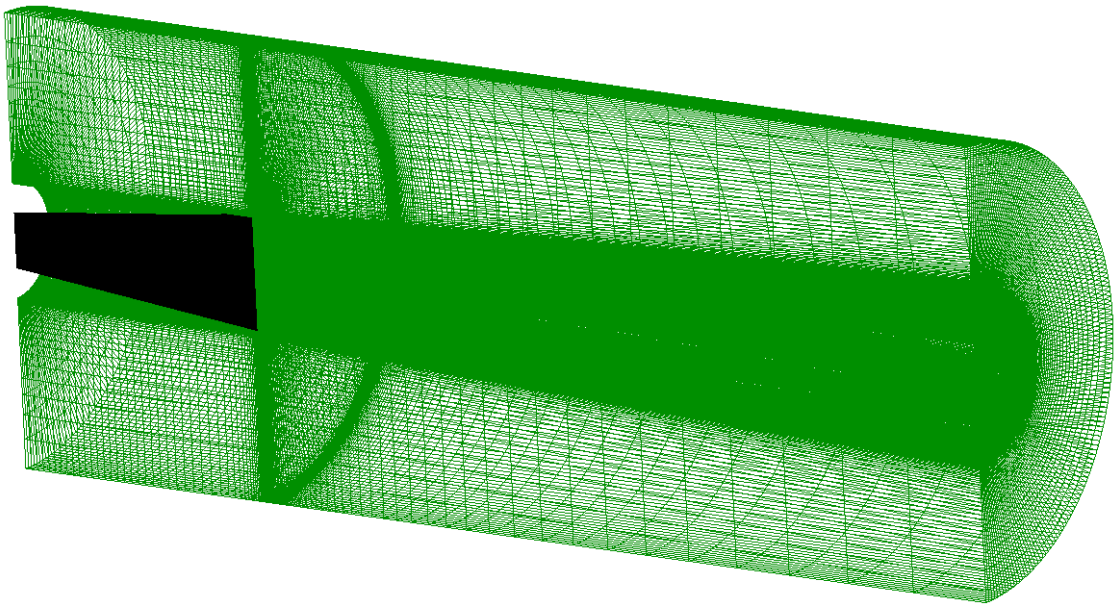

Figure 4.4: Overview of the medium refinement computational mesh (farfield in green).

A three-dimensional structured mesh was developed using intersecting C-grid topologies for the primary nozzle and the secondary injection port. Domain generation and discretization were carried out using the commercial meshing software PointWise. High quality meshes enhance convergence rates, solution accuracy, and numerical stability. Grid quality is determined by several factors, including aspect ratio, skewness, orthogonality, and volume ratio. Different meshing approaches balance implementation speed and simplicity against mesh quality. For example, Fig. 4.5 illustrates four methods for meshing of circular geometries. The simplest mesh to produce, a polar grid, results in a singularity at the centre. This collapses the quadrilateral elements to triangular elements at the core, leading to an unstructured mesh. To achieve a fully structured mesh, the circular patch is divided into four domains in a configuration known as H-grid topology. While the H-grid approach improves cell quality at the centre, it results in highly-skewed cells at the edges. The OH-grid, sometimes called butterfly topology, addresses the cell skewness problems of the previous two by splitting the circle into five domains.

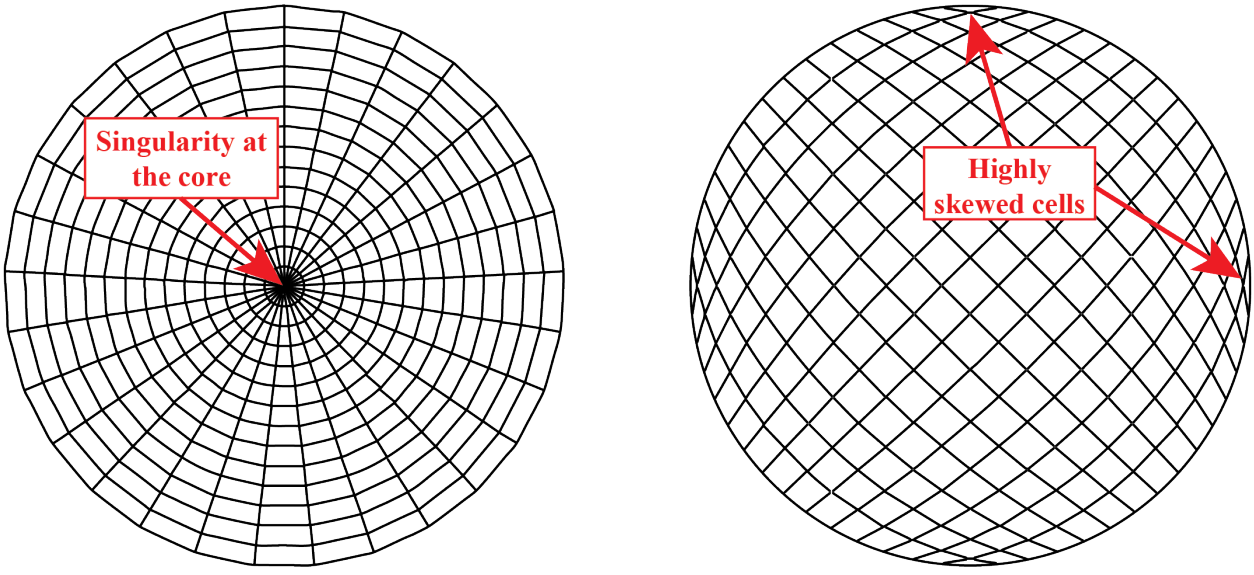

(a) Polar grid.

(b) H-grid.

(c) OH-grid.

(d) C-grid.

Figure 4.5: Overview of circular grid topologies.

The overall nozzle mesh is shown in Fig. 4.6. Note that only half the nozzle was simulated. As such, the C-grid topology (analogous to the OH-grid topology but for semi-circular geometries) was implemented for both the primary nozzle and the secondary injection port as shown in Fig. 4.7a and 4.7b, respectively. Laplacian smoothing was implemented to further improve grid quality by optimizing the area ratio and minimizing cell non-orthogonality.

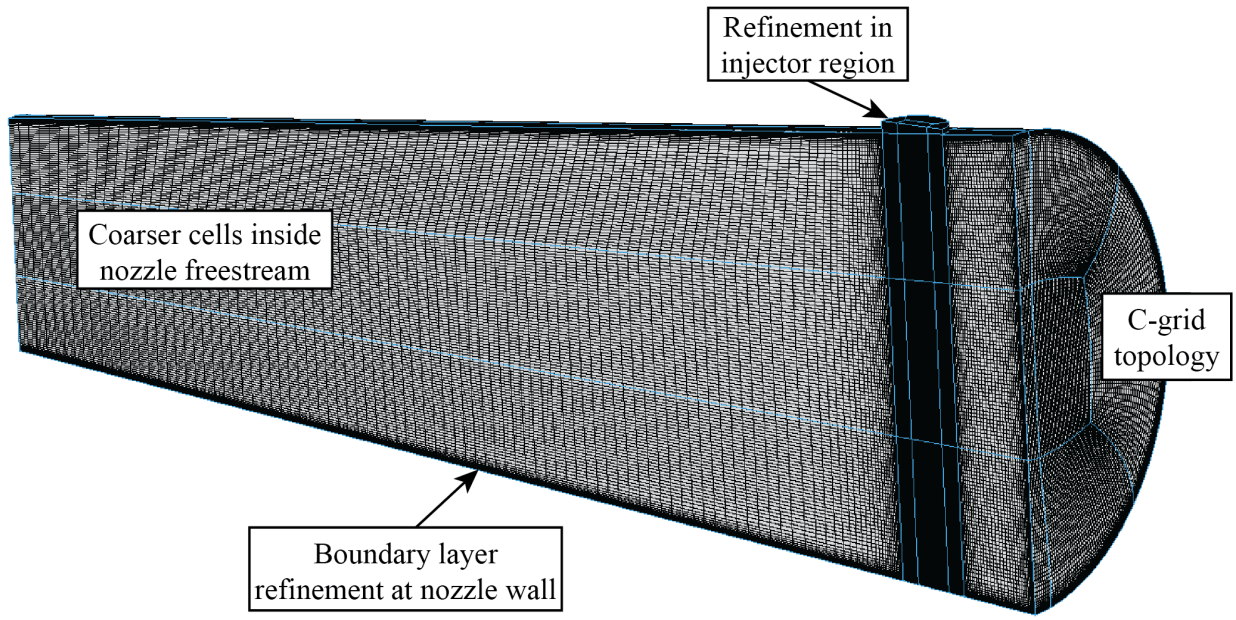

Figure 4.6: Fully structured mesh of axisymmetric nozzle with secondary injection (medium refinement).

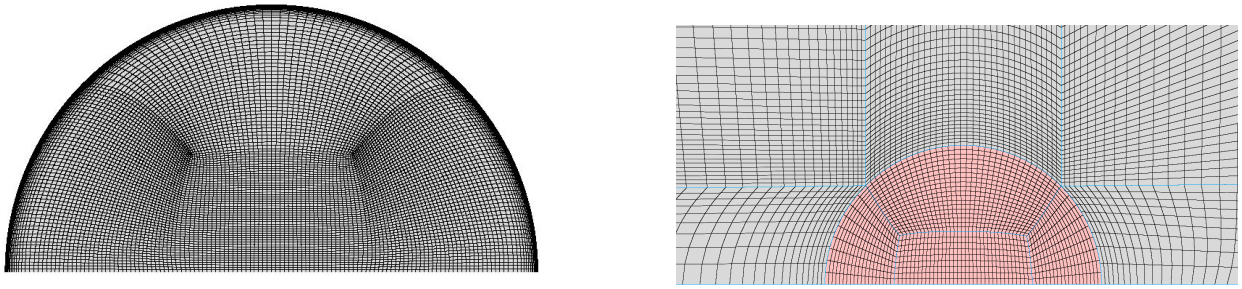

(a) Nozzle exit C-grid with smoothing.

(b) Secondary injection port C-grid with smoothing.

Figure 4.7: C-grids.

Special consideration was given for near-wall meshing to accurately resolve the boundary layer. As discussed in Section 3.1, the features of interest that significantly contribute to the thrust vector lie near the nozzle wall. The boundary layer, caused by friction between the nozzle wall and flow, results in high gradients. Properly resolving this steep profile is critical for accurately calculating the wall shear stress. As such, higher grid resolution was applied near the wall. This boundary layer refinement is characterized using a non-dimensional wall distance measurement, $y+$, that describes the relative importance of turbulent and viscous processes. It is evaluated using Eqs. 4.46 to 4.48:

$$y+ = \frac{yu_\tau}{\nu} \tag{4.46}$$

$$u_\tau = \sqrt{\frac{\tau_w}{\rho_w}} \tag{4.47}$$

$$\tau_w = \frac{1}{2} C_f \rho_\infty U_\infty^2 \tag{4.48}$$

where y, u_τ, and τ_w are the wall-normal distance, friction velocity and wall shear stress, respectively.

Three consecutively refined meshes were generated to evaluate grid independence. Table 4.3 summarizes key mesh statistics including the initial boundary layer spacing at the nozzle exit, the average $y+$ across the nozzle surface and the number of cells for each mesh. The $y+$ profiles at the nozzle surface are shown in Fig. 4.8 for the three meshes. $y+$ is a non-dimensional wall distance, and thus cannot be measured at the injector port. A grey box is used to indicate the location of the injection port in subsequent figures. Most notably, in the region upstream of the injection port, the maximum $y+$ values are 5.9, 2.1, and 0.9 for the coarse, medium and fine meshes, respectively. All three meshes show acceptable $y+$ values in the vicinity of the injector.

Table 4.3: Mesh refinement parameters.

Mesh	BL initial spacing (μm)	Average $y+$	Number of Cells
Coarse	12.0	2.8	3.2×10^6
Medium	5.0	1.7	5.2×10^6
Fine	1.0	0.3	9.8×10^6

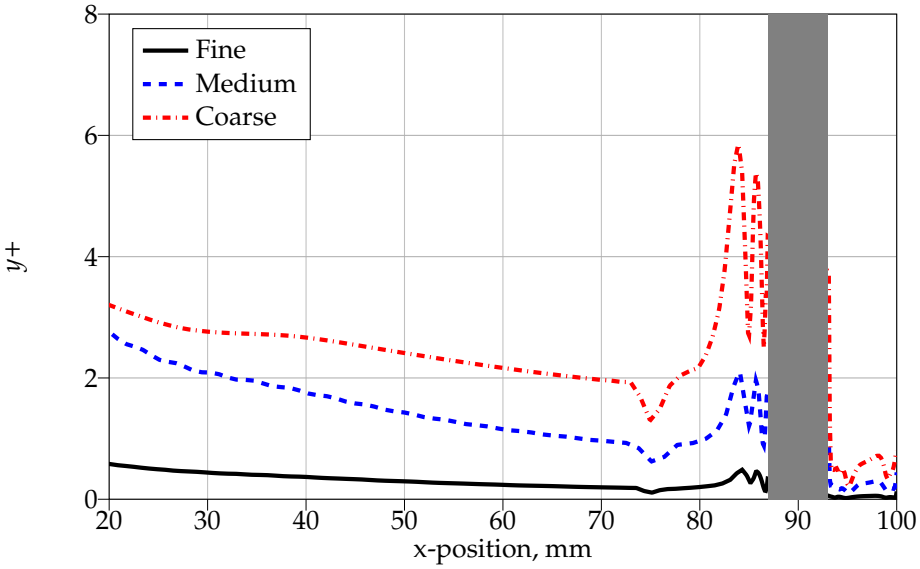

Figure 4.8: $y+$ profiles along nozzle surface for coarse, medium and fine meshes.

4.7 Verification and Validation

To assess the credibility of the results, acceptable levels of error and uncertainty must be demonstrated. Uncertainty is quantified using a mesh refinement study. A validation study could not be performed to quantify error due to incomplete experimental data. Instead, an overview of the validation of the pimpleCentralFOAM solver in the literature is presented for relevant flow features.

4.7.1 pimpleCentralFOAM in the Literature

The pimpleCentralFOAM solver has been extensively validated for single-component flows by the original authors (Kraposhin et al., 2018) and by unaffiliated researchers (Lastiwka et al., 2022). Table 4.4 presents select cases to demonstrate the solver's ability to capture bow shocks, separated flow, turbulent flow, shock wave boundary layer interaction (SWBLI), jet expansion, and flow reattachment.

Table 4.4: Flow features and associated verification cases.

	Supersonic compressible flow	**Bow shock**	**Separated flow**	**Turbulent flow**	**Shock wave BL interaction**	**Jet expansion**	**Flow reattachment**
NASA cold-jet benchmark (Lastiwka et al., 2022)	✓			✓		✓	
Compressible confined jet case (Lastiwka et al., 2022)	✓			✓		✓	
Shock Tube Problem (Kraposhin et al., 2018)	✓						
Backward facing step (Kraposhin et al., 2018)	✓						✓
Nozzle with normal shock (Kraposhin et al., 2018)	✓						
Forward-facing step (Kraposhin et al., 2018)	✓	✓	✓		✓		

4.7.2 Grid Convergence

A grid refinement study is performed to assess discretization errors. The spatial and temporal discretization errors asymptotically approach zero as the grid is refined. Three consecutively refined meshes were generated. As the cell size decreases, the time increments shrink to maintain a maximum CFL number of 0.3. After iterative convergence of the solution is demonstrated, the Richardson extrapolation method is used to approximate the discretization error (Richardson, 1911; Richardson and Gaunt, 1927). If iterative conver-

gence is not achieved, the factor of safety method is used for the uncertainty analysis. The implemented procedure, summarized below, adheres to the American Society of Mechanical Engineers (ASME) standard for verification and validation in CFD (ASME, 2009) with deviation for the factor of safety uncertainty calculations based on Xing and Stern (2010).

For a three-dimensional mesh of N cells, the representative cell size of each mesh, h_M, is calculated according to Eq. 4.49:

$$h_M = \left[\frac{1}{N}\sum_{i=1}^{N} V_i\right] \tag{4.49}$$

where V_i is the cell volume of cell i. The fine, medium and coarse grids are denoted by mesh 1, 2 and 3, respectively. The mesh refinement ratio, which describes the degree of refinement between consecutive grids, is defined in Eq. 4.50.

$$r_{\text{ab}} = \frac{h_{Ma}}{h_{Mb}} \tag{4.50}$$

In this work, second order numerical discretization schemes were used to enhance accuracy. The scheme order describes the power of the leading term in the truncation error. The theoretical order, p_{th} differs from the observed order due to the boundary conditions and the grid. The observed order, which considers these factors, may be obtained using Eq. 4.51 to 4.53 for an arbitrary variable of interest ψ.

$$p = \frac{1}{\ln(r_{21})}\left|\ln\left|\frac{\epsilon_{32}}{\epsilon_{21}}\right| + \ln\left(\frac{r_{21}^{p} - s}{r_{32}^{p} - s}\right)\right| \tag{4.51}$$

$$\epsilon_{\text{ab}} = \psi_a - \psi_b \tag{4.52}$$

$$s = \text{sgn}\left(\frac{\epsilon_{32}}{\epsilon_{21}}\right) \tag{4.53}$$

The ratio of the observed order to the theoretical order, p_r, is defined in Eq. 4.54.

$$p_r = \frac{p}{p_{\text{th}}} \tag{4.54}$$

Similarity between the apparent and theoretical order indicates asymptotic convergence of the solution. Once convergence is demonstrated, the Richardson extrapolation method may be used to obtain a solution of higher-order, $\psi^{21}_{\text{extrapolated}}$, according to Eqs. 4.55 to 4.57. Note that the extrapolated solution is invalid in the region of discontinuities (i.e. shock waves).

$$\psi^{21}_{\text{extrapolated}} = \frac{r_{21}^{p}\psi_1 - \psi_2}{r_{21}^{p} - 1} \tag{4.55}$$

$$e^{\text{ab}}_{\text{approx}} = \left| \frac{\psi_b - \psi_a}{\psi_b} \right| \tag{4.56}$$

$$\text{GCI}_{\text{ab}} = \frac{1.25 e^{\text{ab}}_{\text{approx}}}{r^p_{\text{ab}} - 1} \tag{4.57}$$

The grid convergence index (GCI) method has strict grid refinement requirements to achieve asymptotic convergence, which in practice, are difficult to adhere to for complex geometries. In this work, lack of grid similarity generated observed orders greater than two. The GCI method produces unreasonably small uncertainties when the observed order is greater than the theoretical order. One approach to address this deficiency is the least-squares (LSQ) method, which estimates the error using at least four power series expansions and least-squares data fitting (Eça and Hoekstra, 2014). Another approach is the factor of safety (FS) method, which estimates uncertainty by applying a factor of safety to the GCI error based on the deviation from the asymptotic range (Xing and Stern, 2010). Phillips and Roy (2014) independently analyzed these approaches and concluded that the LSQ and FS methods may be used to estimate uncertainty successfully and exhibit similar accuracy. However, the FS method, requiring only three solutions, is easier to implement and less computationally expensive. In this work, the uncertainty is calculated using the FS approach according to Eqs. 4.58 to 4.60:

$$u_{disc} = FS\,|\delta| \tag{4.58}$$

$$\delta = \frac{\epsilon_{21}}{r^p_{21} - 1} \tag{4.59}$$

$$FS = \begin{cases} 2.45 - 0.85 p_r & 0 < p_r \leq 1 \\ 16.4 p_r - 14.8 & p_r > 1 \end{cases} \tag{4.60}$$

Additionally, the observed order is limited according to $p_{\text{FS}} = max(0.5, min(2, p))$ as suggested by Phillips and Roy (2014).

Figure 4.9 shows the wall pressure distribution at 0 degrees for the three meshes.

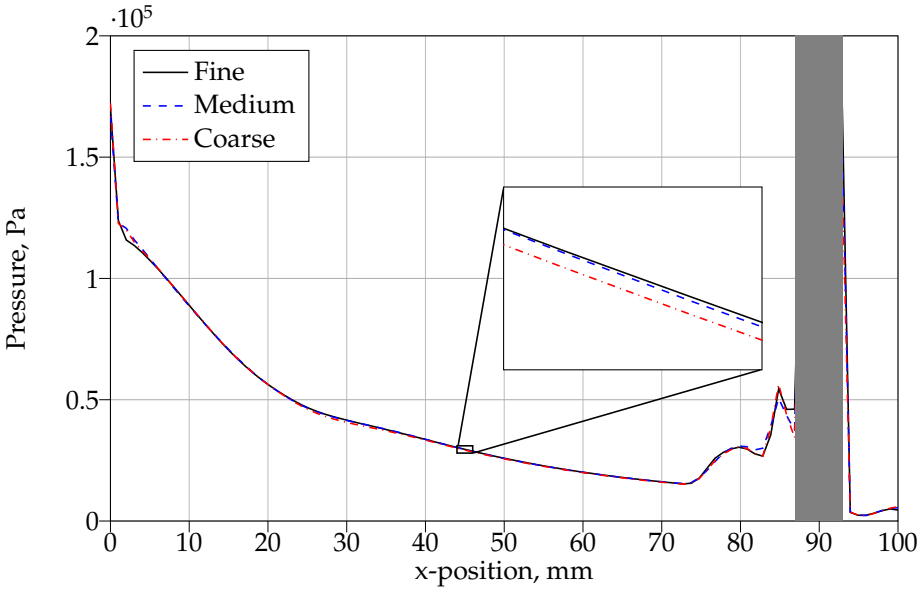

Figure 4.9: Pressure along nozzle wall at 0° compared to x-position for the three meshes.

Selection of the mesh for subsequent simulations requires balancing computational time and accuracy of results. The comparison in Fig. 4.10 shows only a minor reduction in the uncertainty band from the medium to the fine mesh. However, the fine mesh significantly increases computational cost and time. Therefore, the medium mesh was selected for remaining simulations in this work.

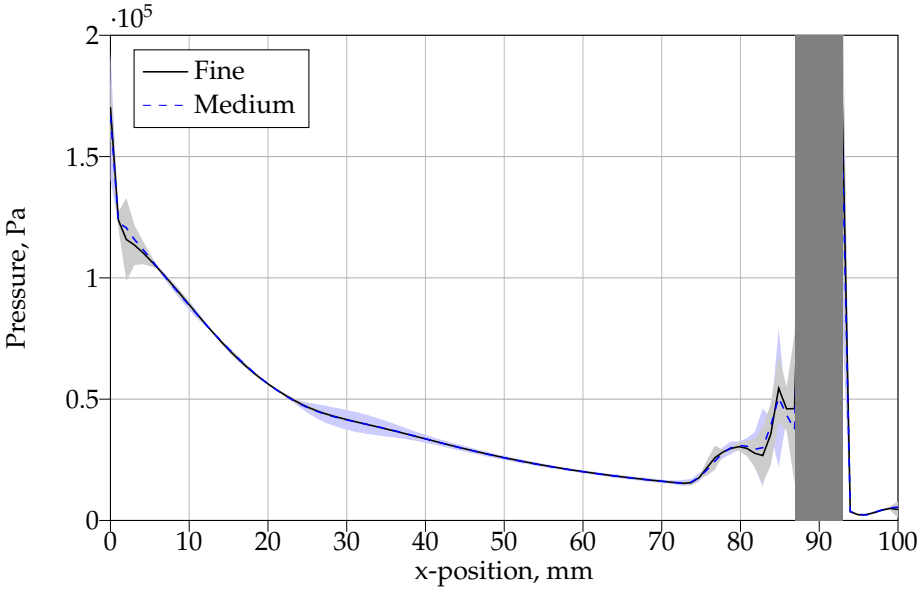

Figure 4.10: Comparison of the fine and medium mesh uncertainty bands for the nozzle pressure profile at 0°.

Chapter 5

Results

Results of the CFD simulations and analytical assessments are jointly presented and discussed. The cold-gas injection case discussed in Section 3.4 was used for validation of the MMC-SIM code. Sample values are provided for SPR=1 unless otherwise specified.

5.1 Overview of the Interaction Field

A qualitative analysis of the CFD simulations offers significant insights into the flow features within an SITVC nozzle. Figure 5.1 presents the streamlines of the flow near the secondary injection port, highlighting key flow structures.

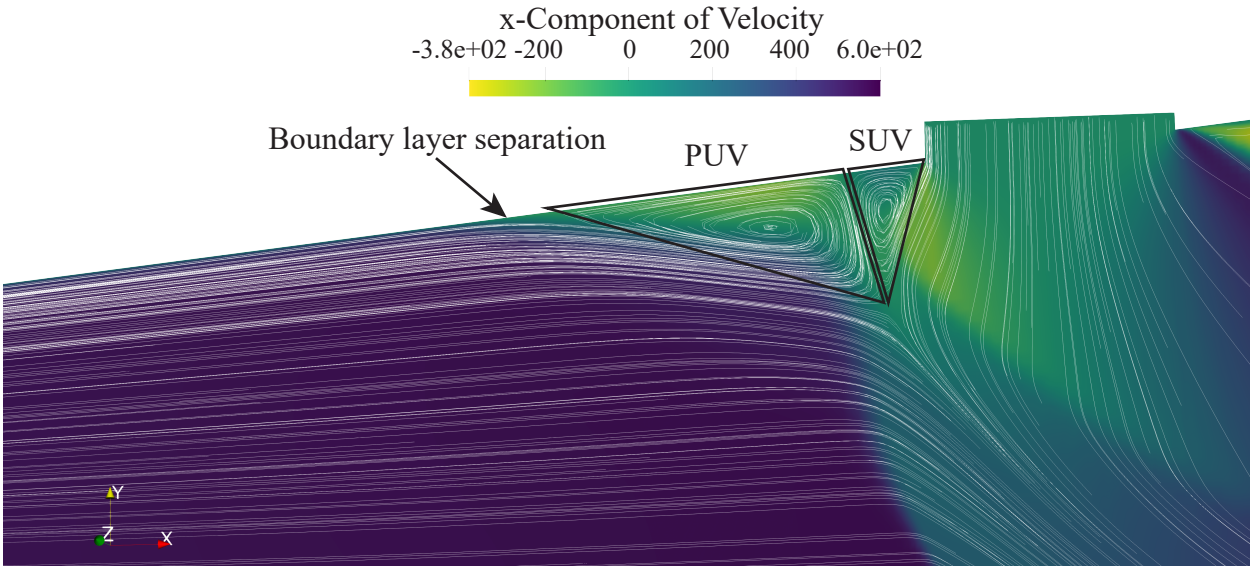

Figure 5.1: Streamlines of two opposing vortices upstream of injector.

Upstream of the secondary gas injection, boundary layer separation occurs, creating two distinct counter-rotating vortices in the plateau region. The primary upstream vortex (PUV), which rotates counter-clockwise, occupies the larger portion of the separation zone, while the secondary upstream vortex (SUV) rotates clockwise.

The primary nozzle flow accelerates in the undisturbed region as expected. At the secondary injection port, the jet is introduced sonically, rapidly expanding and accelerating into the primary flow. The Mach number distribution in Fig. 5.2 provides a detailed view of the regions directly around the injection port. Here, the plateau flow is subsonic upstream of the injection site, a result of the secondary jet obstructing and deflecting the primary nozzle flow. This deflection occurs via two main mechanisms: an oblique separation shock generated upstream of the injection point, and a bow shock surrounding the jet. Numerical Schlieren is used to visualize these discontinuities in Fig. 5.3.

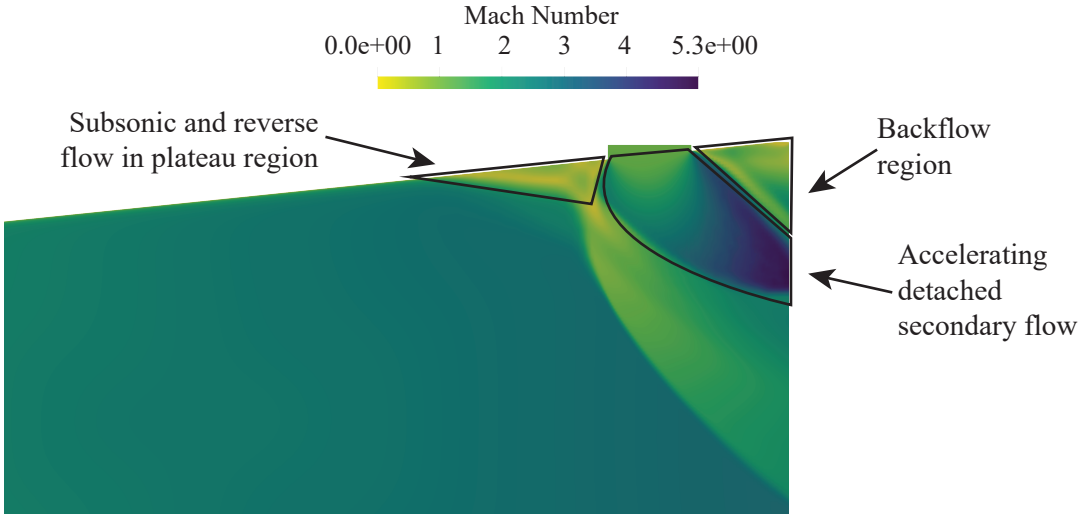

Figure 5.2: Distribution of the Mach number in an SITVC nozzle in the injector port region.

Downstream of the injection, a distinct subsonic region forms, marked by some degree of backflow. This region is associated with extremely low static pressures, lower than the ambient back pressure, creating conditions that allow external flow to re-enter the nozzle. This low-pressure zone, strongly influenced by the stagnation pressure of the external atmosphere, is detrimental to thrust vectoring performance. By driving backflow into the nozzle, it counteracts the desired redirection of thrust, and minimizing this low-pressure region is crucial for improving overall vectoring efficiency.

The secondary jet does not reattach to the nozzle wall following injection. Instead, the flow remains detached, suggesting that the jet expansion and interactions with the primary flow prevent reattachment under the current conditions. This detachment impacts the effective direction and magnitude of the thrust

vector, highlighting areas for potential improvement in future SITVC nozzle designs aimed at optimizing reattachment and minimizing backflow zones for enhanced control authority.

This observation also reveals a limitation in MMC-SIM and similar blunt-body models, which assume the secondary gas deflects parallel to the nozzle wall. However, CFD analysis shows that the jet remains detached under certain conditions. Future work could refine the control volume by incorporating a more accurate representation of the equivalent obstruction, based on this detached flow pattern.

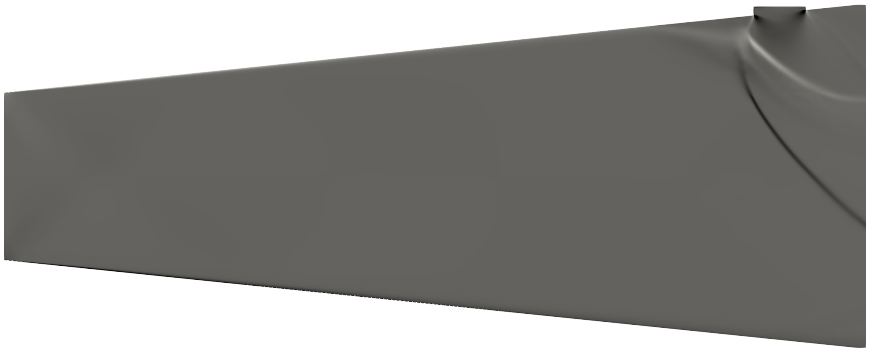

Figure 5.3: Numerical Schlieren of the SITVC nozzle.

The vortical structures generated by SITVC are illustrated in Fig. 5.4 using iso-contours of the Q-criterion, an approach developed by Hunt et al. (1988) to identify vortex-dominated regions in turbulent flows. Here, the Q-criterion is coloured according to the local Mach number, providing context to the intensity and velocity of the vortical flows. The threshold value for the Q-criterion was selected to achieve optimal clarity of the vortex structures. As expected, the SITVC features closely resemble those observed in studies of transverse jets in supersonic crossflows (Zhang et al., 2021). The similarities include the horseshoe vortex, and the counter-rotating vortex pair.

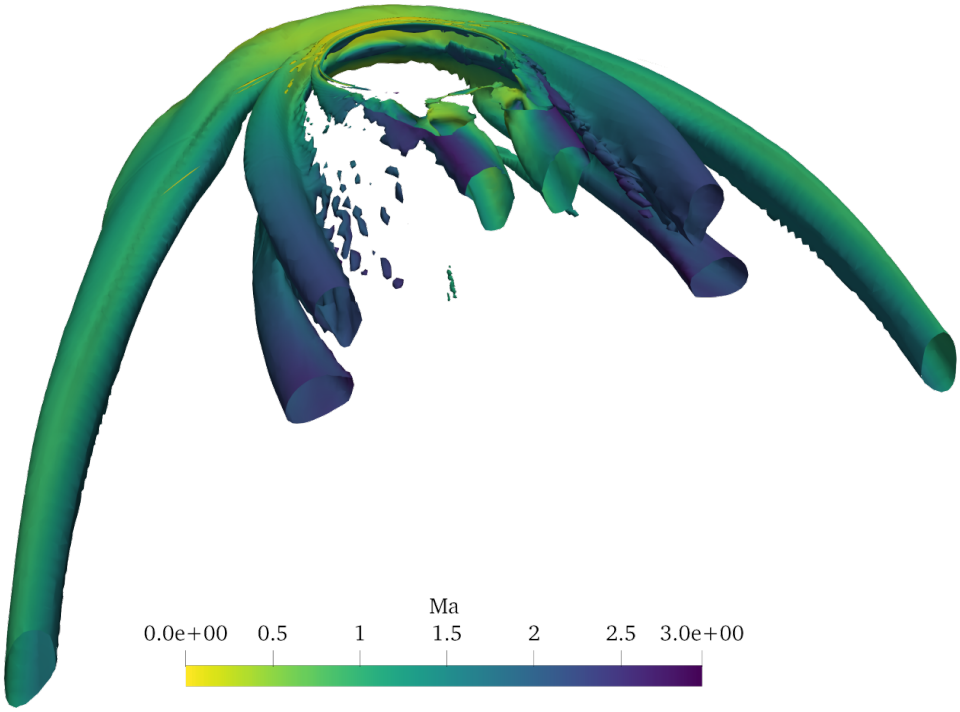

Figure 5.4: Visualization of turbulent structures in SITVC nozzle using Q-Criterion.

5.2 Secondary Jet Shape

Figure 5.5 presents cross-sections of traced secondary jet streamlines taken at various x-positions along the nozzle. Observations reveal that the jet continues to expand at least to the exit face of the nozzle. Additionally, each cross-section has non-uniform pressure and density distributions. The cross-sectional shape of the jet is difficult to pinpoint, but more closely approximates an elliptical area than a semi-circular one.

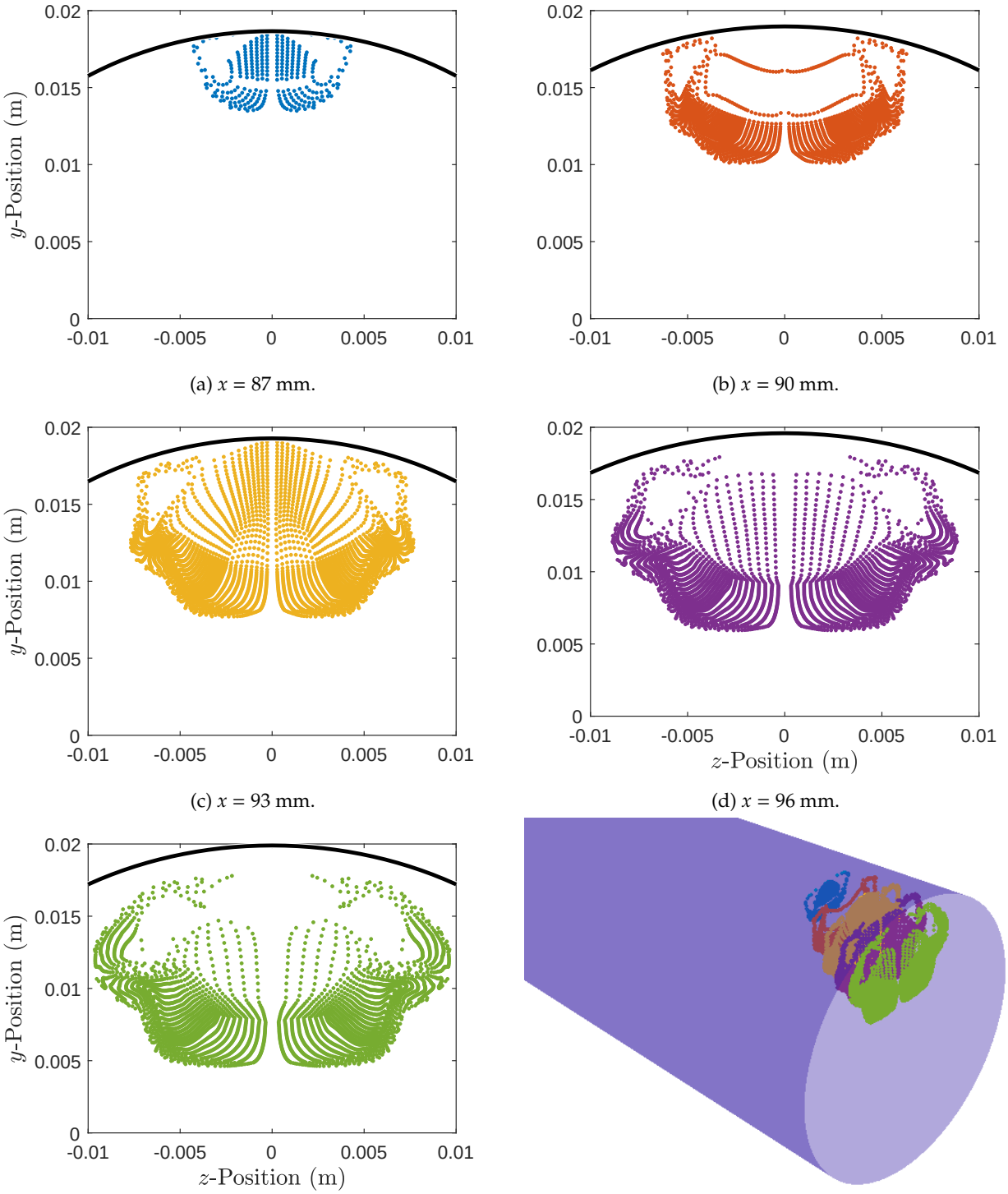

(a) x = 87 mm.

(b) x = 90 mm.

(c) x = 93 mm.

(d) x = 96 mm.

(e) x = 99 mm.

(f) Slices in 3D nozzle.

Figure 5.5: (a) - (e) Cross-sections of secondary jet streamlines with corresponding nozzle wall at various x-positions. (f) Cross-sections within the three-dimensional nozzle.

5.3 Boundary Layer Separation

To compare the boundary layer separation positions from MMC-SIM predictions and CFD simulations, the boundary layer separation position is defined as the location of zero wall shear stress ($\tau_w = 0$). For the case of SPR = 1.000, the CFD simulation results indicate that separation occurs at an x-position of 75.5 mm. Using Eq. 3.1 results in a separation standoff distance of X_s = 14.5 mm. Compared to the MMC-SIM prediction of 16.46 mm, this yields a 13.5% error. Table 5.1 summarizes separation standoff distances across various SPR values, with an average error of 14.8% when compared to CFD results. Additionally, Fig. 5.6 compares the separation standoff distances between MMC-SIM analyses and CFD results.

Table 5.1: Comparison of separation standoff distance results.

SPR	X_s (mm)		
	MMC-SIM	CFD	% Error
0.667	15.29	12.9	18.5%
0.833	15.89	13.6	16.9%
1.000	16.46	14.5	13.5%
1.167	16.98	15.4	10.2%

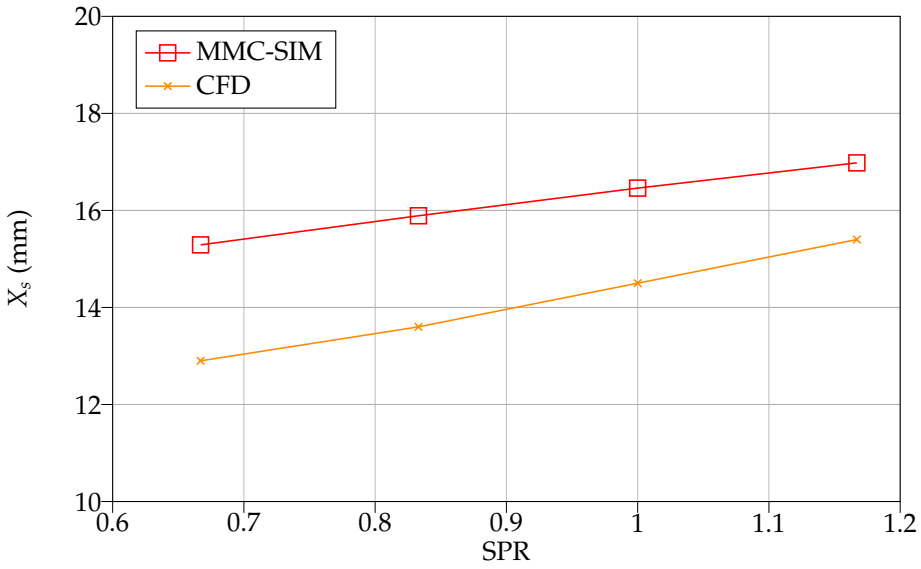

Figure 5.6: Comparison of separation distance as a function of SPR between MMC-SIM analyses and CFD results.

Furthermore, the separation position predicted by the Evry model for the SPR=1 case was provided by Dr. Sellam (personal communication, October 20, 2023) as 84 mm. This yields a separation distance of 6 mm - considerably shorter than that predicted by CFD.

Qualitative comparisons between the analytically- and numerically-determined separation curves are illustrated in Fig. 5.7. The CFD separation curves show some fluctuations that are likely due to mesh-related errors, but still capture the general trend and shape of the BL separation from the nozzle wall. Overall, the MMC-SIM code over-predicts the separation distance, with the predicted separation point occurring further upstream than observed in CFD simulations. Additionally, the shape of the separation curve generated by the MMC-SIM code follows a narrower, hyperbolic profile, compared to the broader curve produced by the CFD results. Such differences highlight a potential area for refinement of the MMC-SIM code, particularly in better representing the separation curve's profile to improve accuracy of thrust vector predictions.

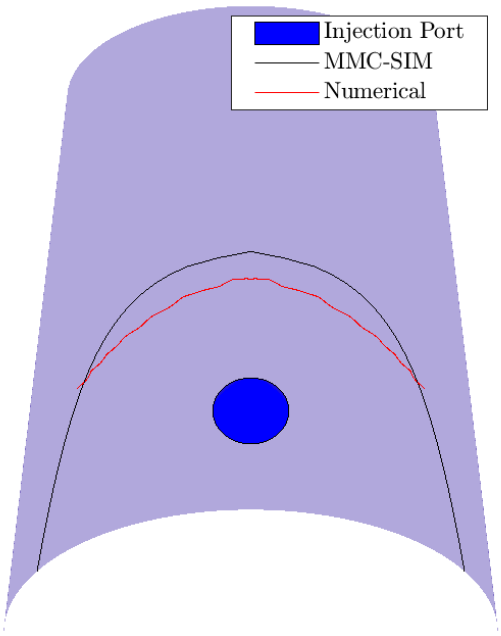

(a) SPR = 0.667.

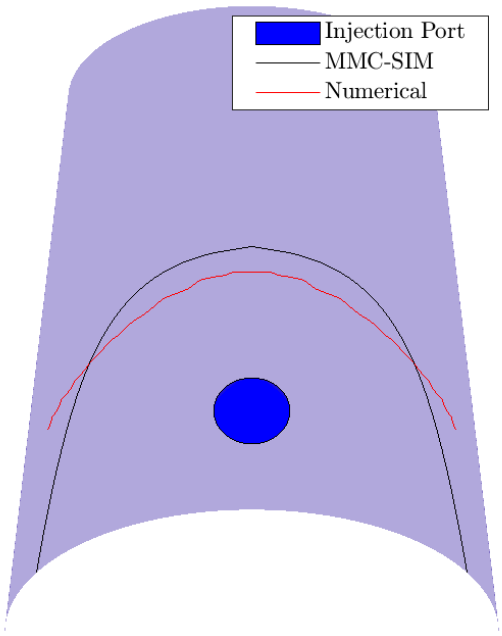

(b) SPR = 0.833.

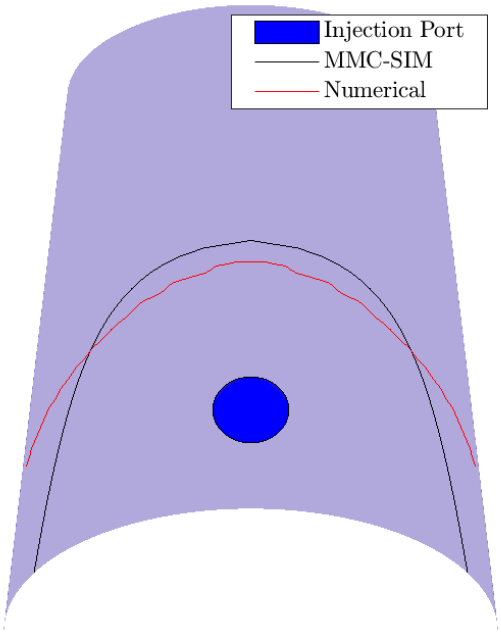

(c) SPR = 1.000.

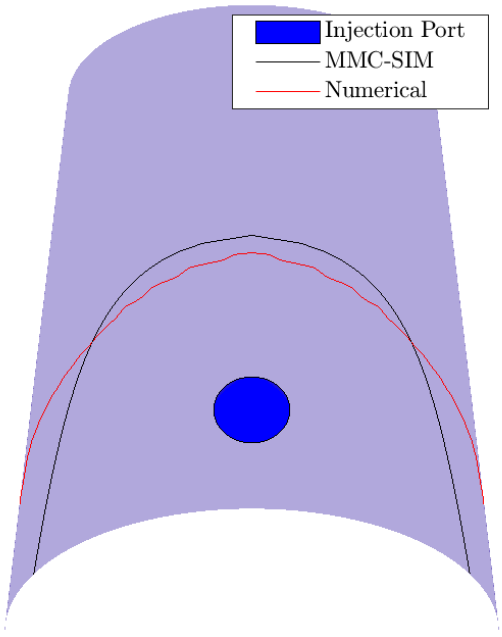

(d) SPR = 1.167.

Figure 5.7: Comparison between boundary layer separation curves determined by MMC-SIM and CFD simulations on nozzle wall.

5.4 Pressure Profile

The pressure profile along the wall at 0°, illustrated in Fig. 5.8, provides insight into the flow behaviour in the SITVC nozzle. As is typical of expanding nozzle flows, the pressure decreases as the flow progresses. Around 72 mm, the adverse pressure gradient begins to develop, as indicated by a reversal in the pressure trend. At some point, the adverse pressure triggers boundary layer separation. The pressure reaches its first peak in the plateau region with a maximum value of 30.9 kPa. Ahead of the secondary injection port, there is a noticeable second pressure spike, reaching 51.5 kPa, as the flow encounters the bow shock. Beyond this, the pressure sharply increases reaching the secondary jet inlet pressure, before sharply decreasing. The pressure drop downstream of the obstruction indicates the presence of localized backflow created by ambient air entering the nozzle.

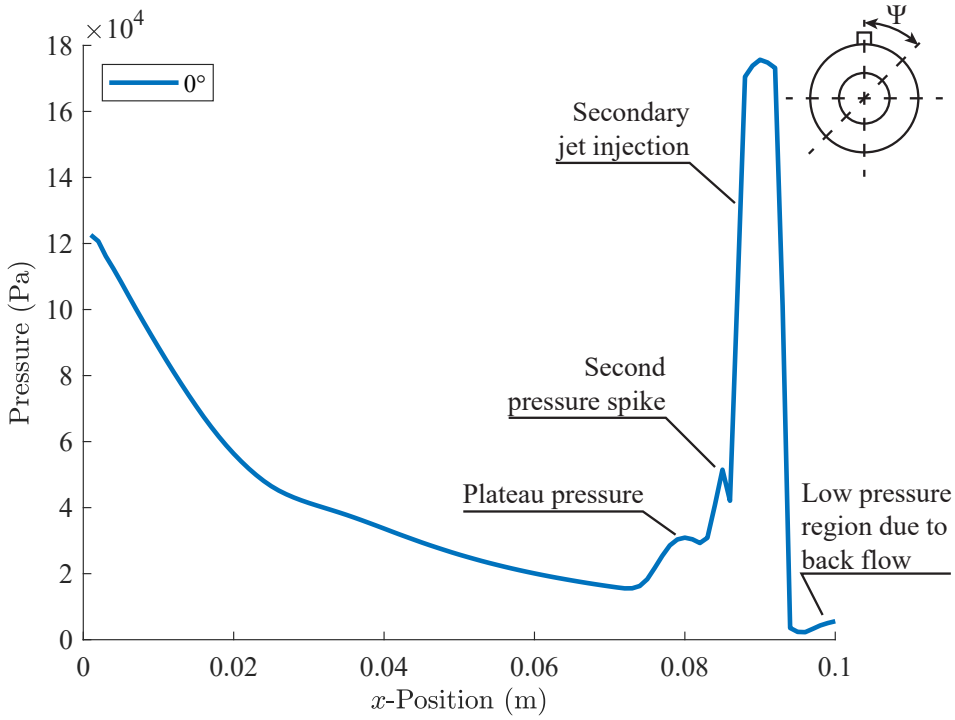

Figure 5.8: Numerically-generated wall pressure distribution for SITVC nozzle operating with SPR = 1 for $\Psi = 0°$.

Figure 5.9 further illustrates how the pressure along the nozzle wall evolves with increasing angular position, Ψ. The plot reveals an attenuated effect, where the influence of the secondary jet diminishes with increasing distance from the injection point.

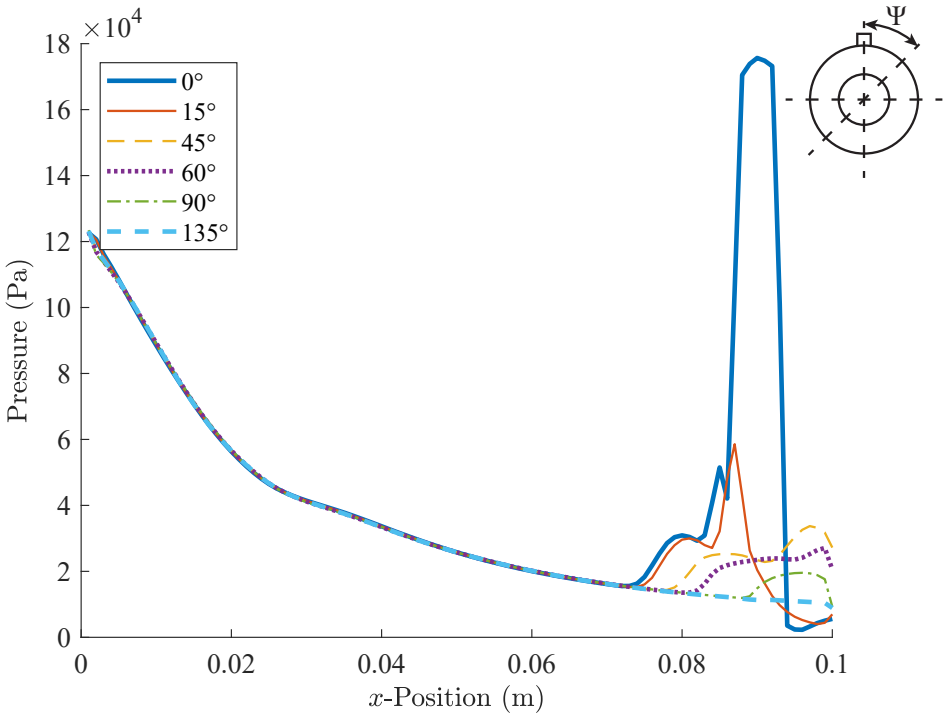

Figure 5.9: Numerically-generated wall pressure distribution for SITVC nozzle operating with SPR = 1 for various angles, Ψ.

Next, the pressure profiles generated using CFD simulations are compared with those used in the analytical model for various angles, as illustrated in Fig. 5.10. Both profiles exhibit a similar trend, showing an initial pressure decrease, followed by an increase ahead of the obstruction. This is consistent with flow behaviour in a supersonic nozzle with a lateral jet injection. While the magnitudes are similar, the numerically-obtained pressure profile is systematically higher than that of the analytical model in the undisturbed region.

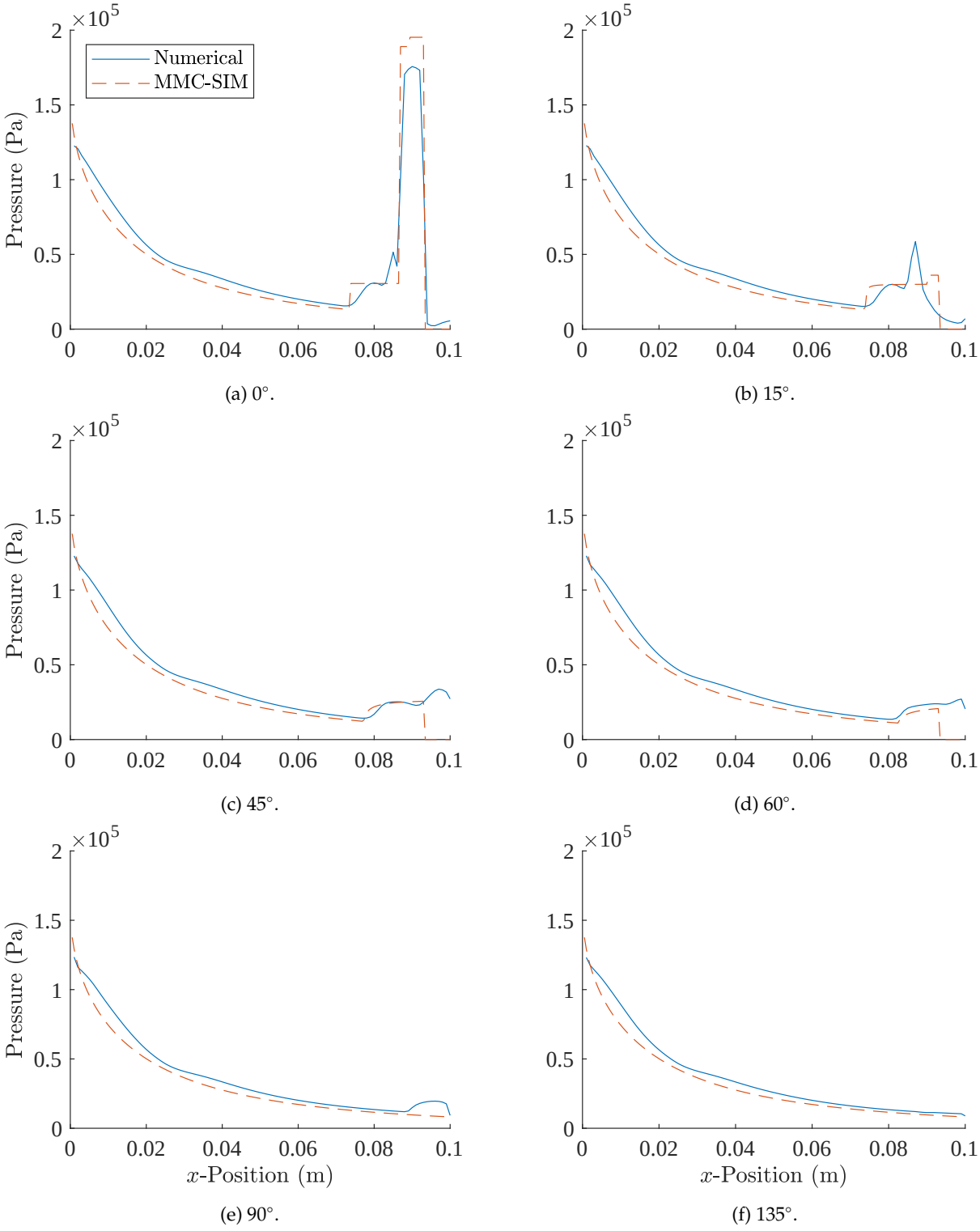

(a) 0°.

(b) 15°.

(c) 45°.

(d) 60°.

(e) 90°.

(f) 135°.

Figure 5.10: Comparison of CFD and analytical wall pressure distributions at various angles for SPR = 1.

5.5 Thrust Vectoring

The thrust vector predictions produced by MMC-SIM are analyzed as a function of SPR, with specific attention to comparing MMC-SIM's accuracy against experimental data. Table 5.2 compares the thrust vector generated by MMC-SIM with experimental measurements, accompanied by calculated percent errors. For easy comparison, these results are also plotted in Fig. 5.11. MMC-SIM yields average errors of 3.3% in predicting total lateral thrust, and 3.2% in estimating the thrust vector deflection angle.

Table 5.2: Validation of MMC-SIM thrust vector results with experimental data from Sellam et al. (2012).

SPR	F_y (N)			F_x (N)			Thrust Vector Angle (°)		
	Exp	MMC-SIM	% Error	Exp	MMC-SIM	% Error	Exp	MMC-SIM	% Error
0.667	12.4	12.85	3.7%	126.8	129.78	2.4%	5.59	5.66	1.3%
0.833	15.0	15.21	1.4%	128.3	129.84	1.2%	6.67	6.68	0.2%
1.000	18.4	17.52	4.8%	127.8	129.89	1.6%	8.19	7.68	6.2%
1.167	20.5	19.82	3.3%	127.3	129.93	2.1%	9.15	8.67	5.2%

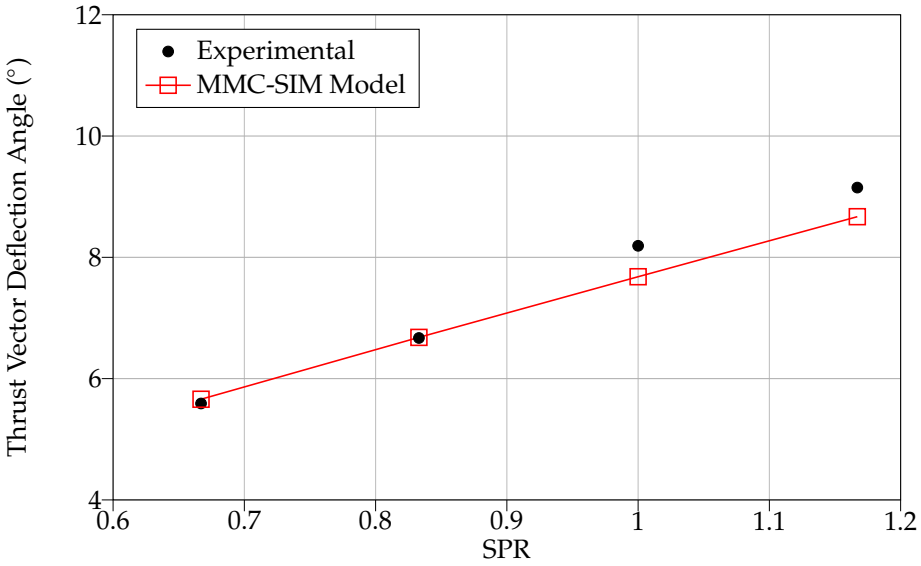

Figure 5.11: Thrust vector deflection angle compared to SPR.

In the University of Evry's experiments, the axial and lateral thrust were directly measured using force

transducers (Sellam et al., 2012). By subtracting the secondary jet momentum, F_{jy}, from the measured lateral thrust, the remaining component approximates the pressure-driven force. Note that the viscous forces are considered negligible, as CFD simulations show that they are approximately one order-of-magnitude smaller than pressure forces.

Table 5.3 compares the results of the MMC-SIM code and the Evry model (the current state-of-the-art from the University of Evry) with experimental data reported by the same research group (Sellam et al., 2012). MMC-SIM achieves an average error of 8.3% and a maximum error of 11.8% in predicting the pressure-driven lateral thrust. Furthermore, it offers a 2.5-fold improvement in accuracy over the Evry model's maximum error of 30.7%.

Table 5.3: Comparison of the pressure-driven lateral force between the MMC-SIM code and Evry model results with experimental data (Sellam et al., 2012).

SPR	Experimental	Evry Model		MMC-SIM	
		Value	% Error	Value	% Error
0.667	5.154	5.091	1.2%	5.609	8.8%
0.833	5.871	6.467	10.2%	6.076	3.5%
1.000	7.388	7.123	3.6%	6.513	11.8%
1.167	7.605	9.940	30.7%	6.925	8.9%

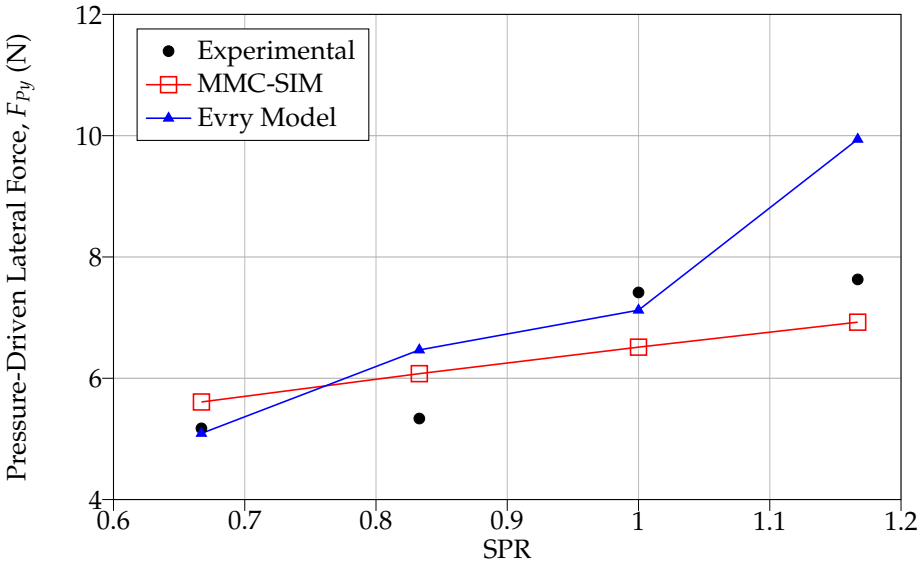

Figure 5.12: Pressure contribution to lateral force compared to SPR.

Chapter 6

Conclusion and Recommendations

6.1 Conclusions

The existing models for secondary injection thrust vector control (SITVC) were reviewed and a critical limitation was identified: mass conservation is not enforced. Instead, the models rely on additional assumptions regarding the secondary jet exit conditions, compromising physical accuracy and introducing significant deviations in continuity in the control volume analysis. Furthermore, prominent models were found to be challenging to reproduce, leading to the introduction of even more assumptions for problem closure.

To address this gap, the mass- and momentum-conserved secondary injection model (MMC-SIM) was developed for the prediction of the thrust vector. Designed for secondary gas injection in three-dimensional axisymmetric nozzles, MMC-SIM provides accurate results fast. Validation against cold-gas experiments demonstrates strong agreement, yielding average and maximum lateral force errors of just 3.3% and 4.8%, respectively. Notably, MMC-SIM reduces the error in the pressure-driven lateral force by up to 2.5 times compared to current prominent models in the field.

As a semi-empirical model based on the blunt-body analogy, the secondary jet is replaced with an equivalent solid obstruction, modelled using a quarter-sphere nose with radius h. Conservation of mass and momentum, as well as semi-empirical relations are used to determine the characteristic height of the injection and the boundary layer separation point along the nozzle. The pressure distribution on the nozzle wall is used to obtain the overall thrust vector direction and magnitude.

Moreover, MMC-SIM is CFD-informed, capturing key flow features that significantly impact force generation, such as the boundary layer separation, oblique and bow shocks, and the pressure distribution

along the wall. Alignment with CFD simulations demonstrates that MMC-SIM is physically representative and able to capture flow characteristics of SITVC.

The findings presented show that MMC-SIM accurately predicts the thrust vector from secondary gas injection into a three-dimensional nozzle with high accuracy, filling a critical gap in the current SITVC modelling landscape and offering a tool for dynamic rocket flight control.

6.2 Recommendations

This section details recommendations that would significantly broaden the scope and utility of MMC-SIM, making it a useful resource in both research and applied aerospace contexts. Each suggested improvement brings the model closer to real-world utility, aligning it more closely with the demands of modern propulsion systems.

Integrating Energy Conservation into MMC-SIM

Future work on refining MMC-SIM could benefit from incorporating energy conservation to further reduce model assumptions and increase alignment with physical reality. The current model relies on mass and momentum conservation, which has provided significant accuracy and reduced reliance on assumptions regarding the secondary jet exit condition. However, introducing energy conservation could capture thermodynamic effects and minimize dependence on empirical relations or simplifying assumptions. Introducing energy conservation could also improve predictions for the interaction of multi-species or reacting flows, where temperature effects play a more significant role.

Expanding Generality of MMC-SIM: Validation and Adaptation of Empirical Relations for Different Gas Properties

For MMC-SIM to be a more versatile tool across a wider variety of engineering setups, future developments should focus on expanding its applicability beyond the current limitations. One of MMC-SIM's primary limitations is its reliance on empirical relations for the bow shock shape, which are currently validated only for gases with a specific heat ratio of $\gamma = 1.4$, typically associated with air, which was selected because of the availability of experimental data in the literature. However, in many high-performance applications, including those involving advanced propellants, the working fluid may have different thermodynamic properties, with γ values often closer to 1.2. Therefore, a key area of improvement involves experimentally validating or modifying these empirical relations for alternative gases, specifically those with $\gamma \approx 1.2$. By broadening the model's accuracy across a range of gas properties, MMC-SIM could better support the

design and simulation of propulsion systems using diverse propellants, enabling its application in a broader spectrum of aerospace setups.

Adapting MMC-SIM for Multi-Port Injection Configurations

Current MMC-SIM functionality is limited to single-port injection configurations, which restricts its applicability in complex propulsion scenarios where multiple injection ports are used to enhance control authority. Expanding the model to accommodate multi-port injection setups would make it much more practical for rocket propulsion applications. This enhancement would require detailed study of the interactions between multiple separation zones and the overlapping shock structures. CFD simulations, which have previously explored similar configurations, could serve as valuable references to inform the model's development in this area. Integrating multi-port capability would make MMC-SIM a powerful tool for simulating thrust vector control in rockets requiring high control authority.

Integration of MMC-SIM into Six Degree-of-Freedom Rocket Flight Simulations

The development of MMC-SIM was driven by the goal of incorporating SITVC into hybrid rocket technology. Embedding MMC-SIM within a six degree-of-freedom (6-DOF) rocket flight simulation framework is the next step to reach this goal. Many parameters needed by MMC-SIM, such as nozzle geometry and flow conditions, overlap significantly with inputs typically required in 6-DOF simulation environments. Incorporating MMC-SIM would allow for real-time thrust vector control calculations that adjust dynamically with flight conditions, making it an invaluable tool for trajectory and control optimization in aerospace applications. By enabling MMC-SIM to interact directly with comprehensive flight simulations, this enhancement could lead to more accurate and efficient control strategies, bridging the gap between model predictions and operational application.

References

Adams, R. A. and Essex, C. (2018). *Calculus: a complete course*. Pearson, 9th edition.

Anderson, Jr., J. D. (2006). *Hypersonic and high temperature gas dynamics*. American Institute of Aeronautics and Astronautics, 2nd edition.

Anderson, Jr., J. D. (2011). *Fundamentals of aerodynamics*. McGraw-Hill, 5th edition.

Andreosky, E. (1965). Functional design of the minuteman flight control system. Technical Report SAE 650598.

ASME (2009). Standard for verification and validation in computational fluid dynamics and heat transfer.

Atta, R. H. V., Reed, S. G., and Deitchman, S. J. (1991). DARPA technical accomplishments: An historical review of selected DARPA projects. Technical report.

Balu, R., Marathe, A. G., Paul, P. J., and Mukunda, H. S. (1991). Analysis of performance of a hot gas injection thrust vector control system. *Journal of Propulsion and Power*, 7(4):580–585.

Barrett, R., Berry, M., Chan, T. F., Demmel, J., Donato, J. M., Dongarra, J., Eijkhout, V., Pozo, R., and Romine, C. (1994). *Templates for the solution of linear systems: Building blocks for iterative methods*. Society for Industrial and Applied Mathematics.

Bell, I. H., Wronski, J., Quoilin, S., and Lemort, V. (2014). Pure and pseudo-pure fluid thermophysical property evaluation and the open-source thermophysical property library CoolProp. *Industrial & Engineering Chemistry Research*, 53(6):2498–2508.

Bell Laboratories (1975). *ABM research and development at Bell laboratories chapter 9: Sprint missile subsystem*.

Billig, F. S. (1967). Shock-wave shapes around spherical-and cylindrical-nosed bodies. *Journal of Spacecraft and Rockets*, 4(6):822–823.

Bondarev, A. E. and Kuvshinnikov, A. E. (2018). Analysis of the accuracy of OpenFOAM solvers for the problem of supersonic flow around a cone. In *Computational Science – ICCS 2018*, pages 221–230. Springer International Publishing.

Broadwell, J. E. (1963). Analysis of the fluid mechanics of secondary injection for thrust vector control. *AIAA Journal*, 1(5):1067–1075.

Burnell, B. (2006). Polaris A3T missile.

Cape Canaveral Space Force Museum (1978). Space launch complex 4 east.

Carrière, P., Sirieix, M., and Solignac, J.-L. (1969). Similarity properties of the laminar or turbulent separation phenomena in a non-uniform supersonic flow. In Hetényi, M. and Vincenti, W. G., editors, *Applied Mechanics*, pages 145–157. Springer Berlin Heidelberg, Berlin, Heidelberg.

Carroll, K. A., Cherrington, W., Greatrix, D., Harry, C., Lapp, P., Porcher, J., Arny Sokoloff, Spencer, H., Trumpour, A., and Viechweg, M. (2009). Microsatellite launch system technical feasibility study project final report. Technical report, Continuum Aerospace.

Case, E. G. (2008). Preliminary design of a hybrid rocket liquid injection thrust vector control system. In *46th AIAA Aerospace Sciences Meeting and Exhibit*, Reno, Nevada. American Institute of Aeronautics and Astronautics.

Chapman, D. R., Kuehn, D. M., and Larson, H. K. (1958). Investigation of separated flows in supersonic and subsonic streams with emphasis on the effect of transition. Technical Report 1356.

Chen, J.-L. and Liao, Y.-H. (2020). Parametric study on thrust vectoring with a secondary injection in a convergent–divergent nozzle. *Journal of Aerospace Engineering*, 33(4).

Chpoun, A., Sellam, M., Zmijanovic, V., and Leger, L. (2017). Secondary injectant gas thermodynamic properties effects on fluidic thrust vectoring performances of a supersonic nozzle. In Ben-Dor, G., Sadot, O., and Igra, O., editors, *30th International Symposium on Shock Waves 1*, pages 539–543. Springer International Publishing, Cham.

Deere, A. (2000). Computational investigation of the aerodynamics effects on fluidic thrust vectoring. In *AIAA/ASME/SAE/ASEE Joint Propulsion Conference & Exhibit*, Huntsville, AL. AIAA.

Deere, K., Berrier, B., Flamm, J., and Johnson, S. (2003). Computational study of fluidic thrust vectoring using separation control in a nozzle. In *21st AIAA Applied Aerodynamics Conference*, Orlando, Florida. American Institute of Aeronautics and Astronautics.

Deere, K., Flamm, J., Berrier, B., and Johnson, S. (2007). Computational study of an axisymmetric dual throat fluidic thrust vectoring nozzle for a supersonic aircraft application. In *43rd AIAA/ASME/SAE/ASEE Joint Propulsion Conference & Exhibit*, Cincinnati, OH. American Institute of Aeronautics and Astronautics.

Deng, R., Kong, F., and Kim, H. D. (2014). Numerical simulation of fluidic thrust vectoring in an axisymmetric supersonic nozzle. *Journal of Mechanical Science and Technology*, 28(12):4979–4987.

Dhinagaran, R. and Bose, T. (1996). Comparison of Euler and Navier-Stokes solutions for nozzle flows with secondary injection. In *34th Aerospace Sciences Meeting and Exhibit*, Reno,NV,U.S.A. American Institute of Aeronautics and Astronautics.

Eça, L. and Hoekstra, M. (2014). A procedure for the estimation of the numerical uncertainty of CFD calculations based on grid refinement studies. *Journal of Computational Physics*, 262:104–130.

Forghany, F., Taeibe-Rahni, M., and Asadollahi-Ghohieh, A. (2018a). Numerical investigation of freestream flow effects on thrust vector control performance. *Ain Shams Engineering Journal*, 9(4):3293–3303.

Forghany, F., Taeibi-Rahni, M., and Asadollahi Ghohieh, A. (2018b). Optimization of freestream flow effects on thrust shock vector control nozzle. *Journal of Applied Fluid Mechanics*, 11(2):361–374.

Green, C. J. and McCullough, F. (1961). Liquid injection thrust vector control. Technical report.

Greenshields, C. J. and Weller, H. G. (2022). *Notes on computational fluid dynamics: General principles*. CFD Direct Ltd, Reading, UK.

Greenshields, C. J., Weller, H. G., Gasparini, L., and Reese, J. M. (2009). Implementation of semi-discrete, non-staggered central schemes in a colocated, polyhedral, finite volume framework, for high-speed viscous flows. *International Journal for Numerical Methods in Fluids*, 63(1):1–21.

Hawkes, T. (1996). Computational analysis of an axisymmetric fluidic injection nozzle. In *34th Aerospace Sciences Meeting and Exhibit*, Reno,NV,U.S.A. American Institute of Aeronautics and Astronautics.

Hou, L., Weigand, B., and Banica, M. (2011). Effects of Staged Injection on Supersonic Mixing and Combustion. *Chinese Journal of Aeronautics*, 24(5):584–589.

Hozaki, S., Gagnon, R., Mayer, E., Tromblay, J., and Wu, J. (1963). Investigation of boundary layer parameters in APG nozzle and the flow interference caused by secondary injection. Technical report.

Hunt, J. C. R., Wray, A. A., and Moin, P. (1988). Eddies, streams, and convergence zones in turbulent flows. Center for Turbulence Research, California, USA.

IAS, E. (2024). Minuteman III: A United States intercontinental ballistic missile.

Indian Space Research Organisation (2019). Polar Satellite Launch Vehicle.

Inouye, T. and Nottage, H. B. (1966). Experiments on rocket thrust vector control by hot gas injection. *Journal of Spacecraft and Rockets*, 3(5):737–739.

JAXA Institute of Space and astronautical science (1997). Launch vehicles M-V.

John, J. E. and Keith, T. G. (2006). *Gas dynamics*. Pearson, Toledo, Ohio, 3rd edition.

Karamcheti, K. and Tao-Sze Hsia, H. (1963). Integral approach to an approximate analysis of thrust vector control by secondary injection. *AIAA Journal*, 1(11):2538–2544.

Karp, A. C., Nakazono, B., Benito Manrique, J., Shotwell, R., Vaughan, D., and Story, G. T. (2016). A hybrid Mars ascent vehicle concept for low temperature storage and operation. In *52nd AIAA/SAE/ASEE Joint Propulsion Conference*, Salt Lake City, UT. American Institute of Aeronautics and Astronautics.

Karp, A. C., Nakazono, B., Vaughan, D. A., Story, G. T., Oglesby, B., and Prince, A. (2018). Update on technology development plan for a low temperature hybrid Mars ascent vehicle concept. In *2018 Joint Propulsion Conference*, Cincinnati, Ohio. American Institute of Aeronautics and Astronautics.

Kirby, D. and Van Vooren, R. (1964). Solid rocket motor thrust vector control system selection. In *1st Annual Meeting*, Washington,DC,U.S.A. American Institute of Aeronautics and Astronautics.

Ko, H. and Yoon, W.-S. (2002). Performance analysis of secondary gas injection into a conical rocket nozzle. *Journal of Propulsion and Power*, 18(3):585–591.

Kobald, M., Fischer, U., Tomilin, K., Petrarolo, A., Kysela, P., Schmierer, C., Pahler, A., Gauger, J., Breitinger, J., Hertel, F., and Hochheimer, B. (2017). Sounding rocket "HEROS" - a low-cost hybrid rocket technology demonstrator. In *53rd AIAA/SAE/ASEE Joint Propulsion Conference*, Atlanta, GA. American Institute of Aeronautics and Astronautics.

Kraposhin, M., Bovtrikova, A., and Strijhak, S. (2015). Adaptation of Kurganov-Tadmor numerical scheme for applying in combination with the PISO method in numerical simulation of flows in a wide range of Mach numbers. *Procedia Computer Science*, 66:43–52.

Kraposhin, M. V., Banholzer, M., Pfitzner, M., and Marchevsky, I. K. (2018). A hybrid pressure-based solver for nonideal single-phase fluid flows at all speeds. *International Journal for Numerical Methods in Fluids*, 88(2):79–99.

Lastiwka, D., Korobenko, A., and Johansen, C. T. (2022). Validation and verification of pimpleCentralFOAM and a 1D-ERAM solver for analysis of an ejector-ramjet. In *AIAA AVIATION 2022 Forum*, Chicago, IL & Virtual. American Institute of Aeronautics and Astronautics.

Lee, E., Kang, H., and Kwon, S. (2019). Demonstration of thrust vector control by hydrogen peroxide injection in hybrid rockets. *Journal of Propulsion and Power*, 35(1):109–114.

Lees, L. (2003). Hypersonic flow. *Journal of Spacecraft and Rockets*, 40(5):700–735.

Lees, L. and Kubota, T. (1957). Inviscid Hypersonic Flow Over Blunt-Nosed Slender Bodies. *Journal of the Aeronautical Sciences*, 24(3):195–202.

Lemmon, E. W. and Jacobsen, R. T. (2004). Viscosity and thermal conductivity equations for nitrogen, oxygen, argon, and air. *International Journal of Thermophysics*, 25(1):21–69.

Lemmon, E. W., Jacobsen, R. T., Penoncello, S. G., and Friend, D. G. (2000). Thermodynamic properties of air and mixtures of nitrogen, argon, and oxygen from 60 to 2000 K at pressures to 2000 MPa. *Journal of Physical and Chemical Reference Data*, 29(3):331–385.

Li, D. and Wu, K. (2021). Numerical Study on Rod Thrust Vector Control for Physical Applications. *International Journal of Aerospace Engineering*, 2021:1–15.

Maarouf, N. (2008). *Modélisation des phénomènes dissymétriques dans le divergent des tuyères supersoniques propulsives: Application a la vectorisation de la poussée*. PhD thesis, L'Université D'Évry-Val D'Essonne.

Mangin, B. (2006). *Vectorisation fluidique de la poussée d'une tuyère plane supersonique*. PhD thesis, Université d'Orléans.

Menter, F. R., Kuntz, M., and Langtry, R. (2003). Ten years of industrial experience with the SST turbulence model. *Heat and Mass Transfer*.

Messinger, T., Hill, C., Quinn, D., Stannard, D., Doerksen, G., and Johansen, C. T. (2019). Development and test flight of the Atlantis I nitrous oxide/paraffin-based hybrid rocket. In *AIAA Propulsion and Energy 2019 Forum*, Indianapolis, IN. American Institute of Aeronautics and Astronautics.

Missilery Info (1971). UGM-27C Polaris A-3 submarine ballistic missile.

Morita, Y. and Kawaguchi, J. (2001). Attitude control design of the M–V rocket. *Philosophical Transactions: Mathematical, Physical and Engineering Sciences*, 359(1788):2287–2303.

Moukalled, F., Mangani, L., and Darwish, M. (2015). *The finite volume method in computational fluid dynamics an advanced introduction with OpenFOAM and MATLAB*. Springer Cham.

Nazeer, A. (2018). Research on PSLV-C37 launcher by ISRO. 7(11).

Newton, J. (1961). Secondary injection for thrust vector control. Technical Report 36-9.

Nickens, T. L., Sutton, J. L., Erickson, L. H., and Sottosanti, P. C. (1970). Thrust vector control study for large (260 in) rocket motor applications. In *JANNAF Interagency Propulsion Committee*, Washington, D.C.

Pelouch, J. (1970). Final report thrust vector control system study program. Technical report, NASA.

Phillips, T. S. and Roy, C. J. (2014). Richardson extrapolation-based discretization uncertainty estimation for computational fluid dynamics. *Journal of Fluids Engineering*, 136(12).

Rathakrishnan, E. (2013). *Theoretical aerodynamics*. John Wiley & Sons, Incorporated, 1st edition.

Reaction Dynamics (2023). Reaction Dynamics: Our Solution.

Resta, E., Marsilio, R., and Ferlauto, M. (2021). Thrust vectoring of a fixed axisymmetric supersonic nozzle using the shock-vector control method. *Fluids*, 6(12):441.

Richardson, L. F. (1911). The approximate arithmetical solution by finite differences of physical problems involving differential equations, with an application to the stresses in a masonry dam. *Philosophical Transactions of the Royal Society of London. Series A, Containing Papers of a Mathematical or Physical Character*, 210(459-470):307–357.

Richardson, L. F. and Gaunt, A. (1927). The deferred approach to the limit. *Philosophical Transactions of the Royal Society of London. Series A, Containing Papers of a Mathematical or Physical Character*, 226(636-646):299–361.

Rowlands, A. (2017). *Physics of Digital Photography*. IOP Publishing.

Sakurai, A. (1953). On the propagation and structure of the blast wave I. *Journal of the Physical Society of Japan*, 8(5).

Schmierer, C., Kobald, M., Tomilin, K., Fischer, U., and Schlechtriem, S. (2019). Low cost small-satellite access to space using hybrid rocket propulsion. *Acta Astronautica*, 159:578–583.

Schmucker, R. H. (1984). Flow processes in overexpanded chemical rocket nozzles. Technical report.

Sellam, M., Chpoun, A., Zmijanovic, V., and Lago, V. (2012). Fluidic thrust vectoring of an axisymmetrical nozzle: An analytical model. *International Journal of Aerodynamics*, 2(2/3/4):193.

Sellam, M., Zmijanovic, V., Leger, L., and Chpoun, A. (2015). Assessment of gas thermodynamic characteristics on fluidic thrust vectoring performance: Analytical, experimental and numerical study. *International Journal of Heat and Fluid Flow*, 53:156–166.

Sethuraman, V. R. P., Kim, T. H., and Kim, H. D. (2021). Control of the oscillations of shock train using boundary layer suction. *Aerospace Science and Technology*, 118:107012.

Simurda, L., Stober, K., Boiron, A., Hornstein, K., Jens, E., and Fletcher, A. (2012). Design and development of a thrust vector controlled paraffin/nytrox hybrid rocket. In *48th AIAA/ASME/SAE/ASEE Joint Propulsion Conference & Exhibit*, Atlanta, Georgia. American Institute of Aeronautics and Astronautics.

SpaceX (2021). Falcon user's guide. Technical report.

SpaceX (2024). SpaceX Mission.

Spaid, F. W. (1964). *A study of secondary injection of gases into a supersonic flow*. PhD thesis, California Institute of Technology, Pasadena, California.

Spaid, F. W. and Zukoski, E. E. (1968). A study of the interaction of gaseous jets from transverse slots with supersonic external flows. *AIAA Journal*, 6(2):205–212.

Starin, S. R. and Eterno, J. (2011). Attitude determination and control systems.

Stofan, A. (1973). Titan/Centaur - NASA's newest launch vehicle. In *Joint Space Mission Planning and Execution Meeting*, Denver,CO,U.S.A. American Institute of Aeronautics and Astronautics.

Story, G. T., Karp, A. C., Nakazono, B., Zilliac, G., Evans, B. J., and Whittinghill, G. (2020). Mars ascent vehicle hybrid propulsion effort. In *AIAA Propulsion and Energy 2020 Forum*, VIRTUAL EVENT. American Institute of Aeronautics and Astronautics.

Story, G. T., Prince, A., Chaffin, J., Oglesby, B., Karp, A., and Kibbey, T. (2018). Low temperature hybrid Mars ascent vehicle concept development at MSFC.

Stuben, K. (2001). An introduction to algebraic multigrid.

Summerfield, M., Foster, C. R., and Swan, W. C. (1954). Flow separation in overexpanded supersonic exhaust nozzles. *Jet Propulsion*, 24(9):319–321.

Sutton, G. P. (2003). History of liquid propellant rocket engines in the United States. *Journal of Propulsion and Power*, 19(6):978–1007.

Sutton, G. P. and Biblarz, O. (2017). *Rocket propulsion elements*. Wiley, 9th edition.

Tsohas, J., Droppers, L. J., and Heister, S. D. (2006). Sounding rocket technology demonstration for small satellite launch vehicle project. Los Angeles, CA.

Tsohas, J., Droppers, L. J., and Heister, S. D. (2007). Progress in technology demonstration for a small hybrid launch vehicle. volume 5.

US Department of Defense (2024). Titan IIIC.

Waithe, K. and Deere, K. (2003). An Experimental and Computational Investigation of Multiple Injection Ports in a Convergent-Divergent Nozzle for Fluidic Thrust Vectoring. In *21st AIAA Applied Aerodynamics Conference*, Orlando, Florida. American Institute of Aeronautics and Astronautics.

Walker, R. E. and Shandor, M. (1964). Influence of injectant properties for fluid injection thrust vector control. *Journal of Spacecraft and Rockets*, 1(4):409–413.

Walker, R. E., Stone, A. R., and Shandor, M. (1962). Secondary gas injection in a conical rocket nozzle i. effect of orifice diameter and molecular weight of injectant. Technical report, The Johns Hopkins University Applied Physics Laboratory.

Weller, H. G., Tabor, G., Jasak, H., and Fureby, C. (1998). A tensorial approach to computational continuum mechanics using object-oriented techniques. *Computers in Physics*, 12(6):620–631.

White, F. M. (2016). *Fluid mechanics*. McGraw-Hill Education, 8th edition.

Whittinghill, G., Whittinghill, I., Aumann, C., and Mosser, N. (2019). Mars ascent vehicle hybrid motor development testing. In *2019 IEEE Aerospace Conference*, pages 1–8, Big Sky, MT, USA. IEEE.

Wilson, W. G. and Comparin, R. A. (1969). Analytical investigation of side jet supersonic stream interaction including vortex flow in rocket nozzles for thrust vector control. Technical Report NASA CR 66754, Virginia Polytechnic Institute, Blacksburg, Virginia.

Woodberry, R. F. H. and Zeamer, R. J. (1974). Solid rocket thrust vector control. Technical Report NASA SP-8114, National Aeronautics and Space Administration.

Wu, J.-M., Chapkis, R. L., and Mager, A. (1961). Approximate analysis of thrust vector control by fluid injection. *ARS Journal*, 31(12):1677–1685.

Xing, T. and Stern, F. (2010). Factors of safety for Richardson extrapolation.

Yan, D., Xiao, Y., Ye, L., Zhao, G., and Wang, L. (2023). Study on the effect of oxidative jet and vortex structure in fluidic throat combined with thrust vector control. *International Journal of Aerospace Engineering*, 2023:1–17.

Younes, K., Grenke, A., Hickey, J.-P., Gagnon, M., and Elzein, B. (2020). Enhanced delayed detached eddy simulations of shock-vector control. In *23rd AIAA International Space Planes and Hypersonic Systems and Technologies Conference*, Montreal, Quebec, Canada. American Institute of Aeronautics and Astronautics.

Younes, K. and Hickey, J.-P. (2020). Fluidic thrust shock-vectoring control: A sensitivity analysis. *AIAA Journal*, 58(4):1887–1890.

Zhang, Z., McCreton, S. F., Awasthi, M., Wills, A. O., Moreau, D. J., and Doolan, C. J. (2021). The flow features of transverse jets in supersonic crossflow. *Aerospace Science and Technology*, 118.

Zmijanovic, V. (2013). *Secondary injection fluidic thrust vectoring of an axisymmetric supersonic nozzle*. PhD thesis.

Zmijanovic, V., Lago, V., Leger, L., Depussay, E., Sellam, M., and Chpoun, A. (2013). Thrust vectoring effects of a transverse gas injection into a supersonic cross flow of an axisymmetric convergent-divergent nozzle. In *Progress in Propulsion Physics*, pages 227–256, St. Petersburg, Russian. EDP Sciences.

Zmijanovic, V., Lago, V., Sellam, M., and Chpoun, A. (2014). Thrust shock vector control of an axisymmetric conical supersonic nozzle via secondary transverse gas injection. *Shock Waves*, 24(1):97–111.

Zmijanovic, V., Leger, L., Depussay, E., Sellam, M., and Chpoun, A. (2016). Experimental–numerical parametric investigation of a rocket nozzle secondary injection thrust vectoring. *Journal of Propulsion and Power*, 32(1):196–213.

Zukoski, E. E. (1967). Turbulent boundary-layer separation in front of a forward-facing step. *AIAA Journal*, 5(10):1746–1753.

Zukoski, E. E. and Spaid, F. W. (1964). Secondary injection of gases into a supersonic flow. *AIAA Journal*, page 8.

Appendix A

Background Theory

Key concepts used for developing the models are summarized, including control volume analysis, compressible flows, and boundary layer theory. The background provided here is not a comprehensive review of fluid mechanics, but is intended to contextualize the models in the literature and the new model proposed in Chapter 3. Detailed derivations of the concepts and equations presented in this section are available in John and Keith (2006); Anderson (2011); White (2016).

A.1 Control Volume Analysis

Control volume (CV) analysis is a simple yet powerful technique for analyzing the large-scale behaviour of fluid in a fixed region (White, 2016). In this integral approach, conservation laws are applied to estimate gross effects on a finite volume of space, in contrast to the differential approach, which analyzes point-by-point data of the flow field. Control volume analysis is practical for low-order modelling of SITVC (Spaid, 1964; Spaid and Zukoski, 1968; Mangin, 2006). The complex fluid behaviours are simplified by selecting an appropriate boundary and applying the conservation laws for mass, momentum and energy provided in Eqs. A.1 to A.3:

$$\frac{d}{dt}\iiint_{CV}\rho dV = \underbrace{\iiint_{CV}\frac{\partial\rho}{\partial t}dV}_{\text{Mass variation rate within CV}} + \underbrace{\oiint_{CS}\rho\boldsymbol{U}\cdot\boldsymbol{n}dS}_{\text{Net mass flux across boundaries}} = 0 \tag{A.1}$$

$$\frac{d}{dt}\iiint_{CV}\rho\boldsymbol{U}dV = \underbrace{\iiint_{CV}\frac{\partial(\rho\boldsymbol{U})}{\partial t}dV}_{\text{Momentum variation rate within CV}} + \underbrace{\oiint_{CS}\rho\boldsymbol{U}(\boldsymbol{U}\cdot\boldsymbol{n})dS}_{\text{Net momentum flux across boundaries}} = \underbrace{\boldsymbol{F}_{net}}_{\text{Net external forces}} \tag{A.2}$$

$$\frac{d}{dt}\iiint_{CV}\rho E dV = \underbrace{\iiint_{CV}\frac{\partial(\rho E)}{\partial t}dV}_{\text{Energy variation rate within CV}} + \underbrace{\oiint_{CS}\rho E(\boldsymbol{U}\cdot\boldsymbol{n})dS}_{\text{Net energy flux across boundaries}} \tag{A.3}$$

where V, t, $\boldsymbol{U}$, $\boldsymbol{n}$, S, and $\boldsymbol{F}_{net}$ are the volume, time, velocity vector, outward normal unit vector, surface, and net external force vector, respectively. The specific total energy, E, is composed of the internal energy, e, and kinetic energy as per Eq. A.4:

$$E = e + \frac{|\boldsymbol{U}|^2}{2} \tag{A.4}$$

A.2 Fluid Modelling

The SITVC problem combines two classical flows: (1) supersonic flow through varying area channel, and (2) jet in supersonic crossflow. There are several factors to consider in the analysis of SITVC, including area change, friction and heat transfer. Modelling assumptions and techniques for simplifying the analysis are introduced in this section, including calorically perfect gas, inviscid flow, and isentropic flow.

Calorically Perfect Gas

The medium, often air, N_2 or propellant exhaust gases, is characterized as a calorically perfect gas in the analysis of SITVC. This assumption neglects the intermolecular forces and the volume occupied by molecules. The perfect gas law relates the pressure, density and temperature according to Eq. A.5:

$$P = \rho RT \tag{A.5}$$

where P, ρ, R, and T are the pressure, density, the specific gas constant and temperature, respectively. Additionally, the gas is assumed to have constant specific heats in the operating range of SITVC. The ratio of specific heats, denoted by γ, is defined as the ratio between the heat capacities at constant pressure (C_P) and volume (C_V), as expressed in Eq. A.6:

$$\gamma = \frac{C_P}{C_V} \tag{A.6}$$

The validity of these approximations for SITVC is discussed in Chapter 4.

Inviscid Flow

Nozzles are designed for high-speed flow and as a result, viscous effects are typically confined to a thin region near the wall, known as the boundary layer (Sutton and Biblarz, 2017). High Reynolds number flows have very thin boundary layers, further limiting the area where viscous losses occur. Consequently, the core flow, where frictional effects are negligible, is modelled as inviscid. Furthermore, even in the presence of shock waves, flow upstream and downstream of the discontinuity may be approximated as inviscid. Internal walls of nozzles are designed to be smooth to minimize friction.

Isentropic Flow

Shock-free nozzle flow is treated as isentropic because it is both adiabatic and reversible. Usually, heat losses to the walls of the rocket account for less than 1% of the total energy and may be neglected (Sutton and Biblarz, 2017). In the absence of dissipative effects from viscosity and discontinuities, the flow is smooth and continuous, making it reversible. Under these ideal conditions, flow through a nozzle is modelled as adiabatic and reversible, resulting in constant entropy. Prediction of changes in flow properties is greatly simplified for isentropic processes.

Stagnation states, which are denoted with the subscript t in this work, may be defined according to Eqs A.7 to A.9:

$$\frac{T_t}{T} = 1 + \frac{\gamma - 1}{2} M^2 \tag{A.7}$$

$$\frac{P_t}{P} = \left(1 + \frac{\gamma - 1}{2} M^2\right)^{\frac{\gamma}{\gamma - 1}} \tag{A.8}$$

$$\frac{\rho_t}{\rho} = \left(1 + \frac{\gamma - 1}{2} M^2\right)^{\frac{1}{\gamma - 1}} \tag{A.9}$$

Note that Eqs. A.8 and A.9 are only valid for calorically perfect gases. The mass flow rate, $\dot{m}$, through a cross-sectional area, A, is calculated using stagnation states according to Eq. A.10:

$$\dot{m} = \frac{P_t}{\sqrt{T_t}} A M \sqrt{\frac{\gamma}{R}} \left(1 + \frac{\gamma - 1}{2} M^2\right)^{-\frac{\gamma + 1}{2(\gamma - 1)}} \tag{A.10}$$

Nozzle flow upstream and downstream of shock waves is approximated as isentropic.

A.3 Nozzle Flow

Control volume analysis for compressible, isentropic flow through a nozzle yields helpful relations for SITVC analysis. Making use of the sonic throat condition, indicated with an asterisk ($*$) in this work, Eq. A.11 relates the Mach number and cross-sectional flow area.

$$\frac{A}{A^*} = \frac{1}{M}\left[\frac{1+\frac{\gamma-1}{2}M^2}{\frac{\gamma+1}{2}}\right]^{\frac{\gamma+1}{2(\gamma-1)}} \tag{A.11}$$

Rockets generate thrust by expelling high-speed exhaust gases from the nozzle. Rockets primarily produce forward thrust by ejecting mass backward, according to Newton's third law. Rocket thrust is composed of the momentum and pressure contributions according to Eq. A.12:

$$\text{Thrust} = \dot{m}U + (P_\text{e} - P_\text{amb})\,A_\text{e} \tag{A.12}$$

where subscripts "e" and "amb" indicate nozzle exit conditions and ambient conditions, respectively.

A.4 Shocks

The injection of a secondary fluid into the supersonic stream generates a series of shocks in the nozzle. Shocks, which are characterized by a sharp and abrupt discontinuity of fluid flow properties, are irreversible and cause a rise in entropy. Shocks are formed due to sudden release of energy (such as an explosion) or due to obstruction of a supersonic flow.

Normal Shock Waves

Normal shock waves, which are perpendicular to the flow direction, drop the flow velocity from supersonic to subsonic speeds. Relations for properties upstream and downstream of the shock are exclusively a function of the upstream Mach number, M_1 and the specific heat ratio, γ. There are many forms of the stagnation pressure ratio across a normal shock wave. One helpful form, shown in Eq. A.13, is presented in John and Keith (2006):

$$\frac{P_{t2}}{P_{t1}} = \frac{\left(\frac{\gamma+1}{2}M_1^2\right)^{\frac{\gamma}{\gamma-1}}}{\underbrace{\left(1+\frac{\gamma-1}{2}M_1^2\right)^{\frac{\gamma}{\gamma-1}}}_{P_{t1}/P_1}\left(\frac{2\gamma}{\gamma+1}M_1^2-\frac{\gamma-1}{\gamma+1}\right)^{\frac{1}{\gamma-1}}} \tag{A.13}$$

Note that the under-braced text in Eq. A.13 is simply the stagnation pressure ratio (P_{t1}/P_1). Minor rearranging yields an equation for the stagnation pressure after the shock, P_{t2}, with respect to the pressure before the shock, P_1, as shown in Eq. A.14:

$$\frac{P_{t2}}{P_1} = \frac{\left(\frac{\gamma+1}{2}M_1^2\right)^{\frac{\gamma}{\gamma-1}}}{\left(\frac{2\gamma}{\gamma+1}M_1^2 - \frac{\gamma-1}{\gamma+1}\right)^{\frac{1}{\gamma-1}}} \tag{A.14}$$

Oblique Shock Waves

When a supersonic flow is turned by an obstruction, a shock wave at an oblique angle forms. In this case, the supersonic flow is deflected by an angle, δ. Unlike normal shocks, the flow may remain supersonic after the shock wave depending on the shock strength. The static pressure ratio across an oblique shock is given by Eq. A.15:

$$\frac{P_2}{P_1} = \frac{2\gamma M_1^2 \sin^2\delta}{\gamma+1} - \frac{\gamma-1}{\gamma+1} \tag{A.15}$$

Equation A.16 relates the oblique shock angle, ζ, to the flow deflection angle, δ.

$$\tan\zeta = \cot\delta \frac{M_1^2\sin^2\delta - 1}{\frac{\gamma+1}{2}M_1^2 - (M_1^2\sin^2\delta - 1)} \tag{A.16}$$

Finally, the Mach number after the oblique shock may be computed using Eq. A.17.

$$M_2^2 \sin^2(\delta-\zeta) = \frac{(\gamma-1)M_1^2\sin^2\delta + 2}{2\gamma M_1^2\sin^2\delta - (\gamma-1)} \tag{A.17}$$

Bow Shocks

A blunt body obstructing a supersonic flow generates a normal shock wave at the nose that curves around the front of the body. This detached shock upstream of an obstruction is referred to as a bow shock. The heightened pressure on the blunt body, and the shape of the bow shock are of interest and are discussed in Sections A.6 and A.7, respectively.

A.5 Boundary Layers

A boundary layer (BL) develops in the vicinity of a solid surface where viscous effects dominate relative to inertial forces. Friction between fluid molecules and a solid surface generates zero relative velocity (no-slip condition). The thin region of fluid flow near the wall is characterized by a steep velocity gradient from

zero to 99% of the freestream velocity at the edge of the boundary layer. For Newtonian fluids, the shear stress at the wall, τ_w, is directly proportional to the velocity gradient according to Eq. A.18:

$$\tau_w = \mu \left.\frac{\partial U}{\partial y}\right|_w \tag{A.18}$$

Furthermore, the pressure gradient in the flow direction is related to the second derivative of the velocity as shown in Eq. A.19:

$$\left.\frac{\partial^2 U}{\partial y^2}\right|_w = \frac{1}{\mu}\frac{\partial P}{\partial x} \tag{A.19}$$

Decreasing pressure along the flow direction ($\partial P/\partial x < 0$) is called a favourable pressure gradient because it prevents the separation of the boundary layer from the wall. On the other hand, increasing pressure ($\partial P/\partial x > 0$) is known as an adverse pressure gradient because the BL is susceptible to separation.

Boundary Layer Separation

Separation of the boundary layer from the wall may occur in the presence of a sufficiently strong adverse pressure gradient. Figure A.1 illustrates the evolution of the boundary layer as the pressure gradient increases. Figure A.1a shows a boundary layer velocity profile that is very rounded, characteristic of a favourable pressure gradient. In Fig. A.1b, the pressure gradient has increased until an inflection point is at the wall, indicating a zero pressure gradient. Further increase of the pressure gradient leads to an adverse pressure gradient and thickening of the boundary layer as shown in A.1c. A critical pressure gradient is reached in Fig. A.1d where a zero velocity gradient (or zero shear stress) at the wall triggers the detachment of the boundary layer from the wall. Once the boundary layer has separated from the wall, further pressure increase results in backflow and recirculation as shown in Fig A.1e.

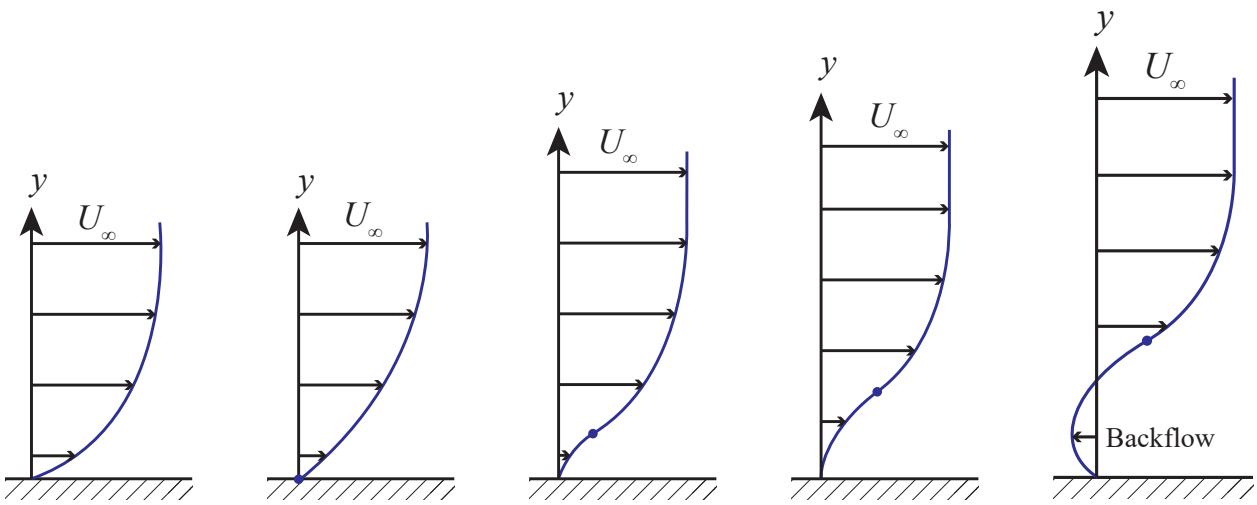

(a) Favourable PG $\frac{\delta U}{\delta y} > 0$, $\frac{\partial P}{\partial x} < 0$.
(b) Zero PG $\frac{\delta U}{\delta y} > 0$, $\frac{\partial P}{\partial x} = 0$.
(c) Adverse PG $\frac{\delta U}{\delta y} > 0$, $\frac{\partial P}{\partial x} > 0$.
(d) Critical APG $\frac{\delta U}{\delta y} = 0$, $\frac{\partial P}{\partial x} > 0$.
(e) Excessive APG $\frac{\delta U}{\delta y} < 0$, $\frac{\partial P}{\partial x} > 0$.

Figure A.1: Effects of increasing pressure gradient on boundary layer profiles. PG = pressure gradient, and APG = adverse PG. Adapted from White (2016).

Supersonic diffusers (diverging nozzles) always have an adverse pressure gradient, but they are generally designed to prevent boundary layer separation. However, in SITVC nozzles, shock waves impinging on the wall generate a sudden pressure increase ahead of the secondary injection port. This phenomena, referred to as shock wave-boundary layer interaction (SWBLI), is a key driver in the asymmetry of the wall pressure distribution, and the overall contribution to the lateral thrust. Understanding the onset of separation is critical for SITVC analysis because it is used to define the pressure distribution along the nozzle wall. Empirical approaches for prediction of the separation point are used in some SITVC models.

A.6 Hypersonic Flow: Modified Newtonian Theory

The surface pressure distribution on a body immersed in a supersonic flow is of interest and often requires powerful computational tools for analysis. However, a very simple technique for pressure estimation was derived based on inelastic collisions between fluid particles and a solid surface. The so-called Newtonian sine-squared law for the pressure coefficient, C_P, is given in Eq. A.20 (Anderson, 2006). This law predicts the pressure distribution on blunt-nosed bodies as illustrated in Fig. A.2.

$$C_P = \frac{P - P_\infty}{\frac{1}{2}\rho_\infty U_\infty^2} = 2\sin^2\Theta \tag{A.20}$$

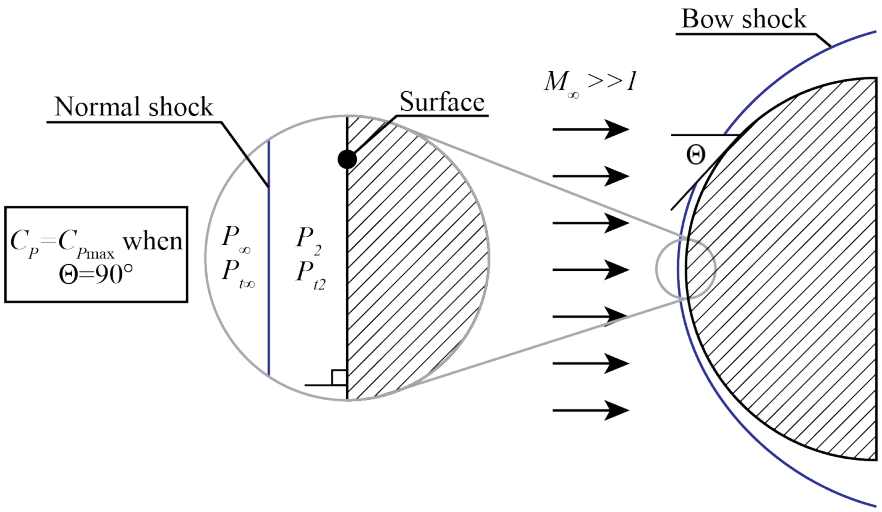

Figure A.2: Schematic of hypersonic flow impinging on blunt-body with local surface inclination of Θ.

Lees (2003) expanded on Newton's work with the modified relation in Eq. A.21 that demonstrates higher accuracy when compared with the original law (Anderson, 2006). Eq. A.21 predicts the surface pressure, P, using freestream flow properties (indicated with subscript ∞) for a hypersonic flow impinging on a surface with a local inclination angle, Θ. It is valid for freestream flows above Mach 2 (Lees, 2003).

$$C_P = \frac{P - P_\infty}{\frac{1}{2}\rho_\infty U_\infty^2} = C_{P\max} \sin^2 \Theta \tag{A.21}$$

The maximum coefficient of pressure, $C_{P\max}$, defined in Eq. A.22, occurs when the obstruction is perpendicular to the freestream flow (Θ = 90°). The pressure at a stagnation point behind a normal shock wave is denoted as P_{t2}.

$$C_{P\max} = \frac{P_{t2} - P_\infty}{q_\infty} = \frac{P_{t2} - P_\infty}{\frac{1}{2}\rho_\infty U_\infty^2} \tag{A.22}$$

Recalling that $\frac{1}{2}\rho U^2 = \frac{\gamma}{2} P M^2$ and rearranging yields an intermediate form shown in Eq. A.23:

$$C_{P\max} = \frac{2}{\gamma M_\infty^2}\left[\frac{P_{t2}}{P_{t\infty}}\frac{P_{t\infty}}{P_\infty} - 1\right] \tag{A.23}$$

Substituting the pressure ratio P_{t2}/P_∞ from Eq. A.14 yields the maximum coefficient of pressure as a function of the freestream Mach number as shown in Eq. A.24.

$$C_{P\max} = \frac{2}{\gamma M_\infty^2}\left[\frac{\left(\frac{\gamma+1}{2} M_\infty^2\right)^{\frac{\gamma}{\gamma-1}}}{\left(\frac{2\gamma}{\gamma+1} M_\infty^2 - \frac{\gamma-1}{\gamma+1}\right)^{\frac{1}{\gamma-1}}} - 1\right] \tag{A.24}$$

A.7 Shock-Wave Shape Around Spherical-Nosed Bodies

High deflection angles imposed by a blunt body in supersonic flow generate a detached shock wave. The shock profile and standoff distance are of interest in the analysis of SITVC. One method to obtain the location and shape of the shock ahead of a spherical-nosed body has been developed by Billig (1967). The shock is assumed to have a hyperbolic profile that is asymptotic with the freestream Mach angle, θ. The general equation for a hyperbola centred at (x_0, y_0) with semi-axes a and b is given in Eq. A.25.

$$\left[\frac{x - x_0}{a}\right]^2 - \left[\frac{y - y_0}{b}\right]^2 = 1 \tag{A.25}$$

Figure A.3 schematically illustrates the hyperbolic detached shock with the corresponding shock standoff distance, Δ, and vertex radius of curvature, R_C.

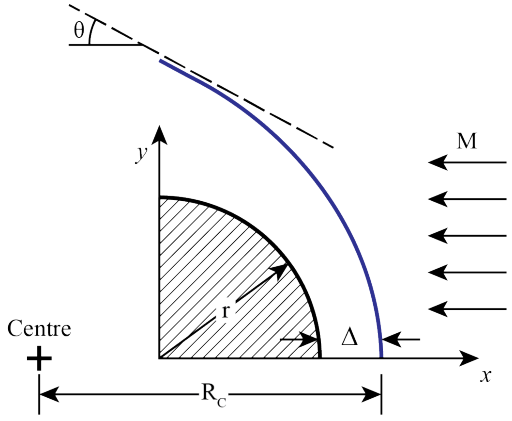

Figure A.3: Schematics of hyperbolic shock generated by spherical-nosed body of radius r. Adapted from Billig (1967).

Billig (1967) proposed the hyperbolic shock profile given in Eq. A.26. Note that this equation describes a pseudo-hyperbola, rather than a true hyperbola. See Appendix B for a detailed explanation and derivation.

$$\left[\frac{x - (r + \Delta + R_C \cot^2\theta)}{R_C \cot^2\theta}\right]^2 - \left[\frac{y}{R_C \cot\theta}\right]^2 = 1 \tag{A.26}$$

Empirically-derived relations for the standoff distance, Δ, and radius of curvature, R_C, are shown in Eqs. A.27 and A.28, respectively (Billig, 1967).

$$\Delta = 0.143 r \exp\left(\frac{3.24}{M^2}\right) \tag{A.27}$$

$$R_C = 1.143 r \exp\left[\frac{0.54}{(M-1)^{1.2}}\right] \tag{A.28}$$

These relations are valid for a perfect gas with $\gamma = 1.4$.

Appendix B

Derivation of Shock Hyperbolas

The general hyperbola centred at (x_0, y_0) with semi-axes a and b shown in Fig. B.1 is defined according to Eq. B.1.

$$\left[\frac{x - x_0}{a}\right]^2 - \left[\frac{y - y_0}{b}\right]^2 = 1 \tag{B.1}$$

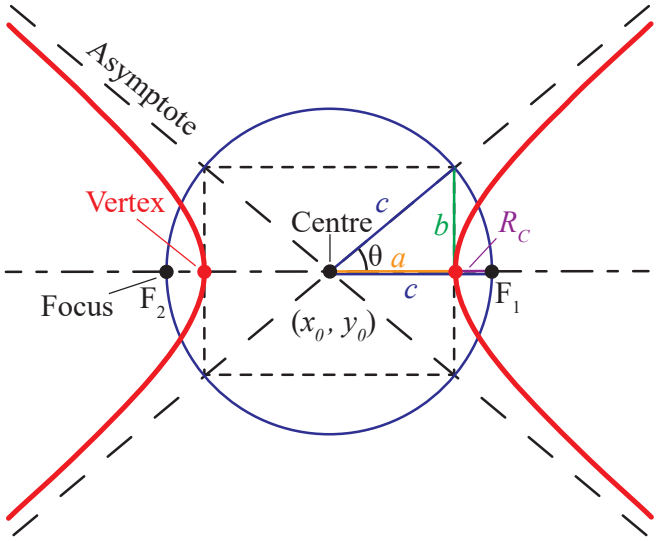

Figure B.1: Schematic of a hyperbola centred at (x_0, y_0) with major semi-axis a and minor semi-axis b. Adapted from Adams and Essex (2018).

Billig (1967) describes a bow shock upstream of spherical and cylindrical-nosed bodies using Eq. B.2.

$$x = R + \Delta - R_C \cot^2\theta \left[\sqrt{1 + \frac{y^2 \tan^2\theta}{R_C^2}} - 1\right] \tag{B.2}$$

Rearranging yields a form of Billig's equation that resembles the general hyperbola equation presented in Eq. B.1.

$$\left[\frac{x-\left(R+\Delta+R_C\cot^2\theta\right)}{R_C\cot^2\theta}\right]^2-\left[\frac{y}{R_C\cot\theta}\right]^2=1 \tag{B.3}$$

By observation, the coefficients can be extracted as follows:

$$\begin{cases} a = R_C\cot^2\theta \\ b = R_C\cot\theta \\ x_0 = R+\Delta+R_C\cot^2\theta \\ y_0 = 0 \end{cases} \tag{B.4}$$

The linear eccentricity, c, is extracted from Fig. B.1 by observation:

$$c = a + R_C = R_C\left(1+\cot^2\theta\right) \tag{B.5}$$

However, the hyperbola coefficients a, b, and c must satisfy the Pythagorean theorem in Eq. B.6:

$$a^2+b^2=c^2 \tag{B.6}$$

Plugging the coefficients determined earlier into the Pythagorean theorem yields an inequality as shown in Eq. B.7.

$$(R_C\cot^2\theta)^2+(R_C\cot\theta)^2 \neq R_C^2\left(1+\cot^2\theta\right)^2 \tag{B.7}$$

The discrepancy demonstrates that Billig's equations describe a pseudo-hyperbola rather than a true hyperbola. Nevertheless, the shock standoff distance, Δ, and vertex radius of curvature, R_C, are scaled using experimental data, ensuring validity of Billig's equation.

If of interest, the true hyperbola coefficients may be determined given that there are three equations and three unknowns (a, b, and c). However, scaling of the new equation using experimental data is required.

$$\begin{cases} a^2+b^2=c^2 \\ \tan\theta = \frac{b}{a} \\ c = a + R_C \end{cases} \tag{B.8}$$

Solving the system of equations yields new coefficients a, b, and c:

$$\begin{cases} a = R_C \cot\theta \left(\cot\theta + \csc\theta\right) \\ b = R_C \left(\cot\theta + \csc\theta\right) \\ c = R_C \cot\theta \left(\cot\theta + \csc\theta\right) + R_C \end{cases} \tag{B.9}$$

Ensure that these coefficients satisfy Eq. B.8 by substituting them back in. It is clear that they fulfill the latter two equations by inspection. Satisfying the Pythagorean theorem requires some rearranging as shown below:

$$a^2 + b^2 = c^2 \tag{B.10}$$

$$R_C^2 \cot^2\theta \left(\cot\theta + \csc\theta\right)^2 + R_C^2 \left(\cot\theta + \csc\theta\right)^2 = \left[R_C \cot\theta \left(\cot\theta + \csc\theta\right) + R_C\right]^2 \tag{B.11}$$

Expand the binomial on the right-hand side:

$$R_C^2 \cot^2\theta \left(\cot\theta + \csc\theta\right)^2 + R_C^2 \left(\cot\theta + \csc\theta\right)^2 = R_C^2 \cot^2\theta \left(\cot\theta + \csc\theta\right)^2 + 2R_C^2 \cot\theta \left(\cot\theta + \csc\theta\right) + R_C^2 \tag{B.12}$$

Cancel the repeated terms:

$$\cancel{R_C^2 \cot^2\theta \left(\cot\theta + \csc\theta\right)^2} + R_C^2 \left(\cot\theta + \csc\theta\right)^2 = \cancel{R_C^2 \cot^2\theta \left(\cot\theta + \csc\theta\right)^2} + 2R_C^2 \cot\theta \left(\cot\theta + \csc\theta\right) + R_C^2 \tag{B.13}$$

Divide both sides by R_C^2:

$$R_C^2 \left(\cot\theta + \csc\theta\right)^2 = 2R_C^2 \cot\theta \left(\cot\theta + \csc\theta\right) + R_C^2 \tag{B.14}$$

$$\left(\cot\theta + \csc\theta\right)^2 = 2\cot\theta \left(\cot\theta + \csc\theta\right) + 1 \tag{B.15}$$

Expand and cancel repeated terms:

$$\cot^2\theta + 2\cot\theta\csc\theta + \csc^2\theta = 2\cot^2\theta + 2\cot\theta\csc\theta + 1 \tag{B.16}$$

$$\cancel{\cot^2\theta} + \cancel{2\cot\theta\csc\theta} + \csc^2\theta = 2\cot^2\theta + \cancel{2\cot\theta\csc\theta} + 1 \tag{B.17}$$

$$\csc^2\theta = \cot^2\theta + 1 \tag{B.18}$$

This is simply a trigonometric identity!

Appendix C

SITVC Modelling Code

MMC-SIM Main File

```
% MMC-SIM
% Mass- and Momentum-Conserved Secondary Injection Model
% N. Abdelwahab
% 20241028

clear; clc; close all;
addpath("functions\", "inputs\");

% Get Inputs
run("input1Evry.m")

summary = zeros(length(SPR),11);

for m = 1:length(SPR)
    % Compute derived properties
    run("derivedProperties.m")

    % Compute injection height (characteristic dimension)
    run('computeInjectionHeight.m')

    % Compute forces
    run("computeForces3D")

```

```
    summary(m,1) = NPR(m);
    summary(m,2) = SPR(m);
    summary(m,3) = Fyj;
    summary(m,4) = Fyw;
    summary(m,5) = Fy;
    summary(m,6) = Fx;
    summary(m,7) = deflection;
    summary(m,8) = a_exp(m);
    summary(m,9) = percentError;
    summary(m,10) = bool;
    summary(m,11) = x_s*1000;
end

summary = array2table(summary, 'VariableNames', {'NPR', 'SPR', 'Fyj', 'Fyw', 'Fty', 'Ftx', ...
    'a_model', 'a_exp', '%% error', 'no shock reflection', 'x_s'});
disp(summary);
avgError = mean(table2array(summary(:,9)),'omitnan');
disp(avgError);

%% Output Results
quiet = true;
if quiet == false
    fprintf('The nozzle is in the %s regime. \n', regime);
    fprintf('======================================== \n \n');
    fprintf('Ms: %f \n', Ms);
    % fprintf('P_sep: %f \n', Ps);
    fprintf('P_plat: %f \n', P2);
    fprintf('x_s/L: %f \n', x_s/nozzle_length);
    % fprintf('beta: %f \n', beta);
    % fprintf('epsilon: %f \n', epsilon);
    fprintf('h: %f \n \n', h);

    fprintf('Sum of forces in x, Fx: %f N \n', Fx);
    fprintf('Sum of forces in y, Fy: %f N \n', Fy);
    fprintf('Net deflection angle: %f degrees \n', deflection);
    fprintf('Mass flow ratio: %f %% \n \n', 100*m_ratio);
    fprintf('<strong>Fy/Fx: %f %% \n \n</strong>', 100*Fy/Fx);

    fprintf('SUMMARY OF FORCES IN X \n');
    fprintf('---------------------------------- \n');
    fprintf('Fc: %f N \n', Fc);
```

```
64      fprintf('Fxtuy: %f N \n', Fxtuy);
65      fprintf('Fxj: %f N \n', Fxj);
66
67      fprintf('SUMMARY OF FORCES IN Y \n');
68      fprintf('------------------------------------ \n');
69      fprintf('Fytuy: %f N \n', Fytuy);
70      fprintf('Fyj: %f N \n', Fyj);
71  end
```

Derived Properties

```
1   %% Properties Derived from Inputs
2   P_th = getPress(gamma_p, M_th, Pt(m));
3   densityt = Pt(m)/gasConstant_p/Tt; % kg/m^2
4   mdot_p = getmdot(gamma_p, gasConstant_p, Pt(m), Tt, area_throat, M_th);
5
6   Pj = getPress(gamma_s, Mj, Ptj(m));
7   mdot_s = getmdot(gamma_s, gasConstant_s, Ptj(m), Ttj, area_port, Mj);
8
9   % Injection plane properties
10  height_inf = 2*x_inj*tand(half_angle) + height_throat; %m
11  if dim == 2
12      area_inf = w*height_inf;
13  elseif dim ==3
14      area_inf = pi/4*height_inf^2;
15  end
16
17  AR_inf = (area_inf/area_throat);
18
19  M_inf = getSuperMach(gamma_p, AR_inf);
20  P_inf = getPress(gamma_p, M_inf, Pt(m));
21  T_inf = getTemp(gamma_p, M_inf, Tt);
22  density_inf = getDensity(gamma_p, M_inf, densityt);
23
24  speedSound_inf = sqrt(gamma_p*gasConstant_p*T_inf);
25  velocity_inf = M_inf*speedSound_inf;
26  dynamicPress_inf = 1/2*density_inf*velocity_inf^2;
27
28  % Exit plane properties
```

```
AR_exit = area_exit/area_throat;

M_exit = getSuperMach(gamma_p, AR_exit);
P_exit = getPress(gamma_p, M_exit, Pt(m));
T_exit = getTemp(gamma_p, M_exit, Tt);
density_exit = getDensity(gamma_p, M_exit, densityt);

if P_exit < P_amb
    regime = 'overexpanded';
    P_av = P_amb;
else
    regime = 'underexpanded';
    P_av = P_exit;
end
% disp(regime);
```

Compute Injection Height

```
% Guess value of h
h = 0.005;

error = 1;
counter = 0;
r = 1; % relaxation factor
∆=13.3; % initialize
while error > 0.0001
    counter = counter + 1;

    % Compute separation distance
    Xs = h*(1/sind(∆) - 1);
    x_s = x_inj - Xs;

    % Compute primary flow properties at x_s
    height_s = 2*x_s*tand(half_angle) + height_throat;
    ARs = getAreaRatio(dim, height_s, height_throat);
    Ms = getSuperMach(gamma_p, ARs);
    Ps = getPress(gamma_p, Ms, Pt(m));
    Ts = getTemp(gamma_p, Ms, Tt);
    density_s = getDensity(gamma_p, Ms, densityt);
```

```
22
23      % Compute plateau pressure using empirical relation
24      Pplat = Ps*(1 + 0.5*Ms);
25
26      % Oblique shock angle and flow deflection angle from oblique shock relations
27      zeta = asind(sqrt((Pplat/Ps*(gamma_p + 1) + (gamma_p - 1))/(2*gamma_p*Ms^2)));
28      ∆ = atand(2*cotd(zeta)*((Ms^2*sind(zeta)^2-1)/(Ms^2*(gamma_p + cosd(2*zeta)) + 2)));
29
30      Mplat = sqrt((Ms^2*sind(zeta)^2 + ...
            2/(gamma_p-1))/(2*gamma_p/(gamma_p-1)*Ms^2*sind(zeta)^2-1))/sind(zeta-∆);
31
32      Pf = (1+0.062*gamma_p*Mplat^2/(1+(gamma_p-1)/2*Mplat^2))*Pplat;
33
34      % Properties in plateau region (after oblique shock)
35      Ttplat = Tt;
36      Tplat = getTemp(gamma_p, Mplat, Ttplat);
37      density_plat = ...
            density_s*(gamma_p+1)*Ms^2*(sind(zeta))^2/((gamma_p-1)*Ms^2*(sind(zeta))^2+2);
38      speedSoundplat = sqrt(gamma_p*gasConstant_p*Tplat);
39      velocityplat = Mplat*speedSoundplat;
40      dynamicPressplat = 1/2*density_plat*velocityplat^2;
41      CPmaxplat = 2/gamma_p/Mplat^2*(((gamma_p+1)/2*Mplat^2)^(gamma_p/(gamma_p-1)) / ...
            (2*gamma_p/(gamma_p+1)*Mplat^2 - (gamma_p-1)/(gamma_p+1))^(1/(gamma_p-1)) - 1);
42
43      % Conservation of Momentum
44      Tjj = @(Mjj) Ttj/(1+(gamma_s-1)/2*Mjj^2);
45      Vjj = @(Mjj) Mjj*sqrt(gamma_s*gasConstant_s*Tjj(Mjj));
46      mV = @(Mjj) mdot_s*Vjj(Mjj);
47      h_momentum = @(Mjj) sqrt(2/pi*(mV(Mjj)/(Pplat + 1/2*dynamicPressplat*CPmaxplat - ...
            P_exit)));
48
49      % Conservation of Mass
50      h_mass = @(Mjj) sqrt(2/pi*mdot_s*sqrt(Ttj)/Ptj(m)./Mjj*sqrt(gasConstant_s/gamma_s).*(1 ...
            + (gamma_s-1)/2*Mjj.^2).^((gamma_s+1)/2/(gamma_s-1)));
51
52      % Find new value of h
53      xroot = fzero(@(Mjj) h_momentum(Mjj)-h_mass(Mjj), 1);
54      h_new = h_mass(xroot);
55
56      error = abs(h - h_new)/h;
57
```

```
    h = h+r*(h_new - h);
end
Xs = h*(1/sind(∧) - 1);
x_s = x_inj - Xs;
xi_s = x_s/cosd(half_angle);

%% Compute the maximum allowable oblique shock angle
y_s = height_s/2;

beta_lim = atand((y_s + height_exit/2)/(nozzle_length - x_s));

% fprintf('max allowable shock angle: %.1f \n', beta_lim);

if zeta≥beta_lim
    fprintf('Shock reflection occurs off inside of nozzle!!! \n')
    fprintf('%.f > %.f \n', zeta, beta_lim)
    bool = 0;
else
    bool = 1;
end
```

Compute Forces 3D

```
%% Compute forces 3D
% Create a vector of n uniformly spaced intervals
x = linspace(0, nozzle_length, n)';
xi = x/cosd(half_angle);

dx = x(2) - x(1);
dxi = dx/cosd(half_angle);

psi = linspace(0, pi, n);
dpsi = psi(2) - psi(1);

run("computePsiMax.m");

% run('visualization_v1.m');

% Compute the supersonic Mach number and isentropic pressure at each x location using AR
```

```
% Initialize
M_k = zeros(length(x), 1);

for j = 2:length(x)
    M_k(j) = getSuperMach(gamma_p, AR_k(j));
end
Pisen = getPress(gamma_p, M_k, Pt(m));

P = zeros(n);
delFx = zeros(n);
delFy = zeros(n);

for i = 2:length(x)
    if x(i) ≤ x_s
        for j = 1:length(psi)
            P(i,j) = Pisen(i);
        end
    elseif x(i) ≤ x_bow
        for j = 1:length(psi)
            if psi(j) > psi_max(i)
                P(i,j) = Pisen(i);
            elseif psi(j) ≤ psi_max(i)
                P(i,j) = Pisen(i) + ...
                    (Pplat-Pisen(i))*sqrt(1-(psi(j)*r(i))^2/(psi_max(i)*r(i))^2);
            end
        end
    elseif x(i) ≤ x_inj - dia_port/2
        for j = 1:length(psi)
            if psi(j) > psi_max(i)
                P(i,j) = Pisen(i);
            elseif psi(j) ≤ psi_max(i) && psi(j) > psi1_max(i)
                P(i,j) = Pisen(i) + ...
                    (Pplat-Pisen(i))*sqrt(1-(psi(j)*r(i))^2/(psi_max(i)*r(i))^2);
            elseif psi(j) ≤ psi1_max(i)
                P(i,j) = Pisen(i) + ...
                    (Pf-Pisen(i))*sqrt(1-(psi(j)*r(i))^2/(psi_max(i)*r(i))^2); %!
            end
        end
    elseif x(i) ≤ x_inj + dia_port/2
        for j = 1:length(psi)
            if psi(j) > psi_max(i)
```

```
                P(i,j) = Pisen(i);
            elseif psi(j) ≤ psi_max(i) && psi(j) > psi1_max(i)
                P(i,j) = Pisen(i) + ...
                    (Pplat-Pisen(i))*sqrt(1-(psi(j)*r(i))^2/(psi_max(i)*r(i))^2);
            elseif psi(j) ≤ psi1_max(i)
                P(i,j) = Pisen(i) + ...
                    (Pf-Pisen(i))*sqrt(1-(psi(j)*r(i))^2/(psi_max(i)*r(i))^2); %!
            end
        end
    elseif x(i) ≤ nozzle_length
        for j = 1:length(psi)
            if psi(j) > psi_max(i)
                P(i,j) = Pisen(i);
            elseif psi(j) ≤ psi_max(i) && psi(j) > psi1_max(i)
                P(i,j) = 0;
            elseif psi(j) ≤ psi1_max(i)
                P(i,j) = 0;
            end
        end
    end
end

radius = zeros(length(x),1);
F_p=zeros(3,1);

for i = 1:length(x)-1
    radius(i) = dia_throat/2 + mean(x(i:i+1))*tand(half_angle);
    points_x(i) = mean(x(i:i+1));
    for j = 1:length(psi)-1
        n1 = [0; 1; 0];
        n2 = rotz(half_angle)*n1;
        nUnit = rotx(-mean(psi(j:j+1))*180/pi)*n2;
        points_y(i,j) = radius(i)*cos(mean(psi(j:j+1)));
        points_z(i,j) = -radius(i)*sin(mean(psi(j:j+1)));
        Area(i) = radius(i)*dpsi*dx;
        F_p = F_p + mean(P(i:i+1,j:j+1),'ALL')*nUnit*Area(i);
    end
end

mdotVj = getmdotV(gamma_s, area_port, Ptj(m), Mj);

```

```
mdotV = getmdotV(gamma_p, area_throat, Pt(m), 1); % m_dot of primary flow * velocity of ...
    primary flow at primary nozzle throat
Fc = mdotV + (P_th)*area_throat;

Fxtuy = -2*F_p(1);
Fytuy = 2*F_p(2);

Fxj = 2*sum(0, 'all') + mdotVj*sind(inj_angle);
Fyj = 2*sum(0, 'all') + mdotVj*cosd(inj_angle) + (Pj-P_inf)*area_port;

F_amb = area_exit*P_amb;

Fx = Fc + Fxtuy + Fxj - F_amb;
Fy =      Fytuy + Fyj;

deflection = atand(Fy/Fx);
m_ratio = Cd*mdot_s/mdot_p;
if bool == 1
    percentError = abs(deflection-a_exp(m))/a_exp(m)*100;
else
    percentError = NaN;
end

Fyw = Fytuy;
```

Compute Shock and Separation Curves

```
%% Compute psi_kmax
dia_throat = height_throat;

% Compute the Mach angle (rads)
mu = asin(1/Ms);

% Radius and area ratio at each x (geometry)
r = dia_throat/2 + x*tand(half_angle);
AR_k = (r/(dia_throat/2)).^2;

% Compute the shock radius and distance between shock and obstruction based on Billig
Rc = 1.143*h*exp(0.54/(Ms-1)^1.2);
```

```
inc = 0.143*h*exp(3.24/Ms^2);

% Compute the center of the shock hyperbola
xi_c = xi_inj - inc + Rc;

% Parameters for bow shock hyperbola
a1 = Rc/(tan(mu))^2;
b1 = Rc/tan(mu);
k1 = xi_inj - inc - a1; %xi_c - Rc - a1;

% Compute z-coordinate of bow shock
z1 = zeros(n,1);
x_bow = k1+a1;
for i = 1:n
    if x(i) ≥ x_bow
        z1(i) = b1*sqrt((xi(i)-k1).^2/a1^2 - 1);
    end
end

% Compute psi_max for the bow shock at each x location
psi1_max = atan(z1./r); % !

% Compute the radius of the separation hyperbola
Rs = xi_c - xi_s;

% Parameters for separation hyperbola
a2 = Rs/(tan(mu))^2;
b2 = Rs/tan(mu);
k2 = xi_c - Rs - a2;

% Compute z-coordinate of separation hyperbola
z = zeros(n,1);
for i = 1:n
    if x(i) ≥ x_s
        z(i) = b2*sqrt((xi(i)-k2).^2/a2^2 - 1);
    end
end

% Compute psi_max at each x location
psi_max = atan(z./r); % !

```

```
% Compute arc length at each x location
L_rk = psi_max.*r;
```

Sample Input File

```
%% Input 1 Universite d'Evry
n = 200;
dim = 3; % two-dimensional or three-dimensional problem

% Ambient Conditions
P_amb = 8000; %Pa

% Nozzle Inputs
height_throat = 0.01944; %m
height_exit = 0.040; %m  0.040921

area_throat = pi/4*height_throat^2;%m^2
area_exit = pi/4*height_exit^2; %m^2

nozzle_length = 0.1; %m
half_angle = atand((height_exit - height_throat)/2/nozzle_length); %deg

% Primary flow inputs
gamma_p = 1.4;
NPR = 37.5*ones(4,1);
Pt = NPR*P_amb;
Tt = 260; %K
molarMass_inf = 28.96; %kg/kmol
M_th = 1; % unitless

gasConstant_p = 8314/molarMass_inf; %J/kgK

% Secondary flow inputs
gamma_s = 1.4;
molarMass_s = 28.96; %kg/kmol
gasConstant_s = 8314/molarMass_s; %J/kgK

dia_port = 0.00615; %m
Ptj = [200000, 250000, 300000, 350000]';
```

```
SPR = Ptj./Pt;
Ttj = 260; % K !
Mj = 1;
x_L = 0.9;
Cd = [1 1 1 1]';
% Cd = [0.824, 0.815, 0.809, 0.839]';
ʌ_exp = [5.59, 6.67, 8.19, 9.15]';

inj_angle = 0; % radians

area_port = pi/4*dia_port^2; %m^2
x_inj = x_L*nozzle_length;
xi_inj = x_inj/cosd(half_angle);
y_inj = x_inj*tand(half_angle) + height_throat/2;
```

Supporting Functions

Area Ratio

```
function AR = getAreaRatio(dim, height1, height_throat)
% Get area ratio
if dim == 2
    AR = (height1/height_throat);
elseif dim == 3
    AR = (height1/height_throat)^2;
end
end
```

Fluid Density

```
function density = getDensity(gamma, M, rhot)
% Get static density from stagnation density
density = rhot./(1+(gamma-1)/2*M.^2).^(1/(gamma-1));
end
```

Oblique Shock Flow Deflection

```
function δ = getFlowDeflection(M, gamma, angle)
% Get flow deflection angle, δ, for an oblique shock
δ = atan(1/tan(angle)*((M*sin(angle))^2-1)/((gamma+1)/2*M^2-((M*sin(angle))^2-1)));
end
```

Mass Flow Rate

```
function mdot = getmdot(gamma, R, Pt, Tt, area, M)
% Get mdot
mdot = sqrt(gamma/R)*Pt/sqrt(Tt)*area*M*(1 + (gamma-1)/2*M^2)^(-(gamma+1)/2/(gamma-1));
end
```

Momentum of Sonic Jet

```
function mdotV = getmdotV(gamma, area, Pt, M)
% Get mdotV for sonic flow
mdotV = gamma*area*Pt*M^2*(1 + (gamma-1)/2*M^2)^(-gamma/(gamma-1));
end
```

Fluid Pressure

```
function P = getPress(gamma, M, Pt)
% Get static pressure from stagnation pressure
P = Pt./(1+(gamma-1)/2*M.^2).^(gamma/(gamma-1));
end
```

Oblique Shock Wave Angle

```
function angle = getShockWaveAngle(M, gamma, P_plat, P_u)
% Get oblique shock wave angle
angle = asin(sqrt((P_plat/P_u*(gamma+1)+(gamma-1))/(2*gamma*M^2)));
end
```

Supersonic Mach

```
function Mach = getSuperMach(gamma, AR)
% Get Mach number from area ratio
for i=1:length(AR)
    syms M
    eqn = AR(i) == 1./M.*((1+(gamma-1)/2*M.^2)/((gamma+1)/2)).^((gamma+1)/2/(gamma-1));

    Mach(i) = double(vpasolve(eqn, M, [1 6]));
end
end
```

Fluid Temperature

```
function T = getTemp(gamma, M, Tt)
% Get static temperature from stagnation temperature
T = Tt./(1+(gamma-1)/2*M.^2);
end
```

Appendix D

Survey of Numerical Simulations of SITVC in the Literature

Table D.1 presents a survey of numerical simulations conducted for SITVC. This literature review highlights selected studies with notable findings and does not encompass all published simulations on SITVC. The table, which is organized chronologically by publication date, includes details on the simulation type:

- **uRANS**: Unsteady Reynolds-averaged Navier-Stokes
- **uEuler**: Unsteady Euler
- **LES**: Large eddy simulation
- **EDDES**: Enhanced delayed detached eddy simulation

It also provides the turbulence model including the Spalart-Allmaras (SA) model.

Table D.1: Summary of key numerical studies of SITVC.

Study	Simulation type	Turbulence model	Nozzle	Case and findings
Balu et al. (1991)	uEuler	-	3D	Numerically investigated hot gas injection experiments performed by Inouye and Nottage (1966) for unsymmetrical dimethylhydrazine/ red fuming nitric acid (UDMH/RFNA) bipropellant rockets. Sonic secondary jet was injected laterally into the nozzle at 46% of the diverging nozzle length. CFD results captured lateral forces with higher accuracy compared to modelling by Broadwell (1963); Walker and Shandor (1964).
Hawkes (1996)	uRANS	$k-\epsilon$	3D	Parametrically investigated SITVC performance for air injection through a slotted port at the throat (throat skewing). CFD simulations consistently over predicted the axial thrust when compared to experiment, especially in the presence of secondary injection.
Dhinagaran and Bose (1996)	uEuler	-	2D	Navier-Stokes model predicts both the experimentally observed flow structure and the pressure distribution near the slot whereas the Euler model fails to predict both of them. The gross system performance parameter, namely, the secondary specific impulse, has been predicted well by both the Euler and the Navier-Stokes model.
	uRANS	Baldwin-Lomax	2D	

Continued on next page

Table D.1: Summary of key numerical studies of SITVC. (Continued)

Study	Simulation type	Turbulence model	Nozzle	Case and findings
Deere (2000)	uRANS	$k-\epsilon$	2D	Investigated the effects of freestream conditions on SITVC performance. Found that the presence of freestream flow decreases performance and efficiency when compared to static conditions, with thrust vector angle penalties ranging from 1.5° to 2.9°.
Ko and Yoon (2002)	uRANS	Baldwin-Lomax	3D	Demonstrated SITVC performance deterioration due to shock impingement and reflection on the opposite wall using numerical simulations of an air-air axisymmetric nozzle. Also, showed that positioning injector port closer toward nozzle exit and decreasing diverging nozzle angle enhances SITVC efficiency over a wide range of pressure ratios. The differences in the results predicted by the Baldwin-Lomax and $k-\epsilon$ turbulence models were negligible.
	uRANS	$k-\epsilon$	3D	
Deere et al. (2003, 2007)	uRANS	$k-\epsilon$	2D/3D	Examined dual throat fluidic thrust vectoring numerically. Demonstrated enhanced thrust vectoring performance using a secondary slotted injection in a recessed cavity. Examined various the effects of various parameters including cavity divergence angle, slot angle, NPRs, and cavity lengths.

Continued on next page

Table D.1: Summary of key numerical studies of SITVC. (Continued)

Study	Simulation type	Turbulence model	Nozzle	Case and findings
Waithe and Deere (2003)	uRANS	$k-\epsilon$	2D	Increasing the injection ports from one to two while maintaining the secondary mass flow rate increases thrust vectoring capabilities without thrust for nozzle pressure ratios below 4 and at high SPRs. Generally, numerical simulation results fell within experimental uncertainty.
Zmijanovic et al. (2016)	uRANS	$k-\epsilon$	3D	Parametric investigation of cold flow SITVC for 3D converging-diverging and truncated ideal contour nozzles. Achieved thrust vector angles of 5-9° with mass flow rate ratio of 5-8%.
Chpoun et al. (2017)	uRANS	$k-\epsilon$	3D	Thermodynamics properties of air, He, CO_2, and Ar were investigated to assess performance as secondary injectants. Gases with lower molar mass were found to have higher thrust vectoring efficiency of around 2°/% as compared to 1°/% for air-air cases. Significant thrust vector angles up to 15° may be achieved with mass flow rate ratios of 7.5%.
Forghany et al. (2018b,a)	uRANS	SA	2D	Investigated time response of an SITVC nozzle with external flow. Concluded that increasing the freestream flow negatively affects the TVC response time. Suggested improvements by varying NPR and SPR values.

Continued on next page

Table D.1: Summary of key numerical studies of SITVC. (Continued)

Study	Simulation type	Turbulence model	Nozzle	Case and findings
Chen and Liao (2020)	uRANS	$k-\epsilon$	2D	Performed a parametric study on SITVC comparing air and hydrogen peroxide injectants. While similar thrust vector angles are produced, the hydrogen peroxide injectant has a higher specific impulse. Hydrogen peroxide concentration had little effect on the results. The $k-\omega$ turbulence model much higher accuracy than $k-\epsilon$ when the wall pressures were compared to experimental data.
	uRANS	$k-\omega$	2D	
Younes et al. (2020)	EDDES	$k-\omega$ SST	3D	Investigated SITVC in NASA's verification test case with a modified expansion ratio of 3.5 using hybrid RANS/LES numerical simulations. Observed expected flow structures including horseshoe vortex and ring vortex.
Resta et al. (2021)	uRANS	SA	3D	Compared the effects of static and freestream flow ($M = 0.6, 0.9$ and 1.2) conditions for a 3D SITVC nozzle with a slotted injection port.
Yan et al. (2023)	uRANS	$k-\omega$ SST	2D	Examined the effects of oxidative jets on SITVC performance. Compared the injection of nitrogen and pure oxygen into the throat and the diverging section of the nozzle.
	LES	-	3D	